FUNDAMENTAL STUDY OF CU-BASED CATALYSTS FOR METHANOL OXIDATION

by

Hao Chi

Bachelor of Science, The Ohio State University, 2013

Submitted to the Graduate Faculty of

Swanson School of Engineering in partial fulfillment

of the requirements for the degree of

Doctor of Philosophy

University of Pittsburgh

2018

UNIVERSITY OF PITTSBURGH

SWANSON SCHOOL OF ENGINEERING

This dissertation was presented

by

Hao Chi

It was defended on

July 16, 2018

and approved by

Robert M. Enick, Ph.D., Professor
Department of Chemical and Petroleum Engineering

Wissam A. Saidi, Ph.D., Associate Professor
Department of Mechanical Engineering & Materials Science

Guangwen Zhou, Ph.D., Professor
Department of Mechanical Engineering, State University of New York Binghamton

Dissertation Co-Directors:

Götz Veser, Ph.D., Professor
Department of Chemical and Petroleum Engineering

Judith C. Yang, Ph.D., Professor
Department of Chemical and Petroleum Engineering

FUNDAMENTAL STUDY OF CU-BASED CATALYSTS FOR METHANOL OXIDATION

Hao Chi, PhD

University of Pittsburgh, 2018

Heterogeneous catalysis plays a crucial role in addressing clean energy and chemical production needs. Currently, controlling the nanoscale structures, metal-support interfaces, and chemical states of heterogeneous catalysts via rational catalyst design are still major challenges. The aim of this dissertation is to experimentally identify active phases and active sites of Cu-based catalysts, which is the most widely used class of heterogeneous catalyst in the methanol industry. Firstly, Cu oxidation states that present in Cu/ZnO catalysts was evaluated in partial oxidation of methanol (POM) under different reaction conditions, a strong dependency between metallic Cu state and POM H_2 selectivity was found. No such dependency was observed between POM CO_2 selectivity and Cu oxidation state, CO_2 selectivity only depended on O_2 partial pressure. In the second part of the thesis, the active sites of Cu_2O nano-islands was identified during MeOH induced reduction using Environmental Transmission Electron Microscopy (ETEM). A two-stage reductive shrinking mechanism for Cu_2O nano-islands on Cu(100) facets was observed which featuring a transition from anisotropic to isotropic shrinking which is caused by preferential adsorption of methanol molecules on Cu(100) step edges rather than flat Cu(100) terrace. Finally, the third part of the thesis examines the atomic scale dynamics of Cu_2O nano-island and its interface with Cu during MeOH induced reduction. Interfacial transformations from Cu_2O to Cu facilitated by preferential reactions at the perimeters of Cu_2O islands was observed, which could alter interfacial reactivity under MeOH and lead to island tilting resulting from the accumulation of Cu at Cu/Cu_2O interface. Overall, this project yielded key insights on identifying the active phases and sites of Cu-based catalysts during MeOH oxidation which will enrich the fundamental understanding towards selective designing heterogeneous catalysts in the future.

TABLE OF CONTENTS

LIST OF TABLES

LIST OF FIGURES

PREFACE

Foremost, I would like to express my sincerest acknowledgement to my research advisors, Professor Götz Veser and Professor Judith Yang, for their guidance and support over the past five years. They taught me how to do research and communicate effectively which benefit me in my future career. Without their contribution of time, ideas and financial support, none of this work would have been possible.

I would like to thank Professor Guangwen Zhou and his group for their contribution to this collaborative project. I am also grateful to Professor Wissam Saidi and Professor Robert Enick for serving as my committee members. I would like to thank them for their insightful comments and suggestions.

I would like to thank Dr. Susheng Tan, Matt France, Mike McDonald, Dr. Cole Van Ormer and Dr. Joel Gillespie for training and technical support.

I would like to thank Dr. Christopher Andolina, Dr. Matthew Curnan, and Dr. Meng Li for helping me so much on my project, and also Dr. Yungchieh Lai, Dr. Stephen House, Dr. Qing Zhu, Dr. Lianfeng Zou, Dr. Amey More for their help on my experiments and discussion of results.

I would like to thank to my colleagues and friends, Dr. Sharlee Mahoney, Yahui Yang, Henry Ayoola, Dr. Jiaqi Zhao, Jierui Liang, Dr. Ke Xu, Zhongmou Chao, Dr. Xiaoxiao Yu, for their help on countless occasions.

My final and most heartfelt acknowledgment must go to my parents and my beloved fiancée Qing. Their support, encouragement, and companionship have kept me motivated, and turned my journey through graduate school into a pleasure. They have my everlasting love.

1.0 INTRODUCTION

1.1 BACKGROUND AND SIGNIFICANCE

The diminishing supply of petroleum and the pollution problems associated with their combustion necessitates the search for alternative fuel sources. One sustainable source of energy are alcohols, which can be directly oxidized in fuel cells to generate electricity. Methanol is of particular interest because of its high energy density, safe handling and easy synthesis from a variety of sources, including fossil fuels, renewable (biomass) sources [1, 2], or even atmospheric CO_2 and H_2 [3], and as a means of hydrogen storage [4-7]. Methanol can easily be converted into a H_2-rich gas mixture (up to 75%) at relatively low temperatures (200-300 °C) using catalytic methanol oxidation [8-11]. Methanol has a high hydrogen/carbon ratio (4:1), consists solely of C, O, and H, and – in contrast to other fuels – contains no carbon-carbon bonds. Thus, the risks of coke formation and catalyst fouling are minimized, the quantity of combustion reaction by-products (such as CO_2, which contributes to global warming) is reduced, and sulfur is not present in the fuel. Therefore, the next generation of methanol-based energy devices, which include Direct Methanol Fuel Cells (DMFCs), are strong candidates for clean energy generation [12-17].

Hydrogen can be obtained directly from methanol by a variety of processes such as Steam Reforming (SR) [18-21] and the Partial Oxidation of Methanol (POM) [9, 22]. The overall reactions are summarized in Equation (1-1—1-2):

$$\text{(POM):}\quad CH_3OH + \frac{1}{2}O_2 \rightarrow 2H_2 + CO_2 \qquad \left(\Delta H^0_{298} = -191.9 kJ/mol\right) \tag{1-1}$$

$$\text{(SR):}\quad CH_3OH + H_2O \rightarrow 3H_2 + CO_2 \qquad \left(\Delta H^0_{298} = +49.4 kJ/mol\right) \tag{1-2}$$

Steam reforming gives the highest hydrogen concentration; but the main disadvantage of the SR reaction is its endothermicity, which inhibits short start-up and fast transient behavior due to the required external heating. Moreover, the need to produce steam makes the process even more energy-demanding. In comparison, hydrogen can be produced with no need for external heating through the partial oxidation of methanol with oxygen or air, and this process can respond quickly to the fuel cell in which it is performed at any given moment. Therefore, the experiments in this work are mainly focused on POM.

Partial oxidation of methanol is typically catalyzed by metal. The most widely used catalysts for hydrogen production from methanol by partial oxidation are Cu-containing catalysts over conventional supports (such as Al_2O_3 and SiO_2) [23-28]. Cu-based catalysts have also been used in MeOH synthesis and oxidation for decades [29-31]. So far, much effort has been invested in understanding the impact of Cu loading and the addition of metal promoters, in order to improve catalyst stability and catalytic performance [32-37]. Although Cu is generally believed to require low-temperature POM, the exact identity of the active species (Cu^0 or Cu^{1+} or Cu^{2+}) of copper [10, 38-55] and the effect of microstructural features, such as defects and surface orientations, of copper catalysts on their reactivity are currently unclear[56-58].

Both Cu^0 and Cu^{1+} species have been speculated to be essential for hydrogen generation from MeOH [59, 60]. For example, Huang et al. proposed that Cu^+ species help to increase the activity of Cu-based catalysts, in which both Cu^0 and Cu^+ species are essential for hydrogen generation from CH_3OH and catalyst activity is dependent on the ratio of Cu^+/Cu^0 [61]. Recent work furthermore has shown that co-feeding product gas (H_2 and CO_2) to the reaction can modify Cu oxidation state and hence catalytic performance. This work suggested that higher Cu^0 and Cu^{1+} content leads to higher H_2 selectivity [62]. However, other studies have suggested that, under similar conditions, Cu^0 is active for MeOH oxidation to H_2 and CO_2, Cu^{1+} is active for H_2O and CO formation, and Cu^{2+} – as the least active species – only actively produces H_2O and CO_2 [33, 35, 62].

For any heterogeneous catalytic system including Cu based catalysts, only very limited work on the relationship between structural features, such as surface structure, interface and defects, of metal catalysts and their reactivity exists. However, the potentially dramatic impact of structural changes on catalyst behavior is well-recognized. Reactions in which some crystal facets are much more active than others are called structure sensitive [63]. One example is ammonia synthesis over Fe catalysts, in which the Fe(111) surface is found to be more active than other Fe surfaces [63, 64]. Although the activity of metals is influenced by pretreatments such as cold-working, ion-bombardment, quenching, and annealing [65, 66], lattice defects and threading dislocations at the surface of metal catalysts could also play an important part in catalytic reactions.

So far, the study of the impact of copper's structural features on its catalytic activity in methanol oxidation has been mainly using theoretical calculation methods such as density function theory and Kinetic Monte Carlo simulations[67-70]. Although energetics of some key reaction steps such as methanol dissociative adsorption and reaction intermediates such as methoxy and formate from methanol oxidation have been calculated for certain Cu single crystal surfaces and Cu oxides, direct experimental observation of the impact of these structural aspects of Cu that is required to build structural-activity correlation is still insufficient. Lawton et al. have recently observed that methoxy prefer to form and buildup at the Cu(111)/CuO_x interface using scanning tunneling microscope (STM) [71]. Behrens et al. reported that Cu steps decorated with Zn atoms, stabilized by a series of well-defined bulk defects revealed by a combination study of density function theory and transmission electron microscopy (TEM) are responsible for methanol synthesis reaction[72]. Lunkenbein et al. observed the formation of metastable amorphous ZnO layers around Cu during reduction activation of methanol synthesis [73]. With the significant advancement of in situ techniques such as Environmental Transmission Electron Microscopy (ETEM) in recent years, Cu based material and its structural impact in a catalytic reaction ought to be better understood.

1.2 *IN SITU* CHARACTERIZATION OF CATALYTIC REACTIONS

The controversies and questions that arise in the understanding of heterogeneous catalysis, such as Cu-catalyzed POM, are in part due to the lack of correlated structural and chemical information of the catalysts under reaction conditions. Dynamic studies of catalysts are important because post-reaction examinations of a static catalyst do not often accurately represent its states in reaction environments [74]. For example, the morphology and the surface structure of metal particles upon cooling differ from those under dynamic conditions [63], and catalytic surfaces have been shown to reconstruct – often reversibly – upon exposure to adsorbates [75]. Another issue for post-examination is atmospheric contamination that may also contribute to these controversies.

Catalytic gas-surface reactions are dynamic processes, therefore the dynamic structure and chemistry of catalysts under working conditions play a pivotal role in these processes. Due to the complexity of catalytic reactions, which involve the interplay between surface structure and surface chemistry, a single characterization technique is usually not sufficient to provide a complete picture of their reaction mechanisms. Thus, a combination of *in situ* techniques providing complementary information will be very helpful in solving the complex problems mentioned above. These techniques and this information range from the nanoscale structure and morphology given by Environmental Transmission Electron Microscopy (ETEM) to the overall surface structure and chemistry provided by X-ray Photoelectron Spectroscopy (XPS). In order to correlate structural changes to catalytic properties, kinetic measurements can also be performed by applying reactor systems to samples matching those used in the *in situ* experiments.

Direct observations of the micro-structural evolution and active sites of catalysts under reaction conditions are critical for understanding the catalytic mechanism [63, 76-83]. *In situ* E-TEM is a powerful technique that can provide direct real-time dynamic information that cannot be readily obtained other techniques such as XPS. Using *in situ* TEM techniques, the nanoscale morphological evolution and chemical modifications and crystallographic orientation of a catalyst can be visualized directly under gas environments, and therefore provide essential insights into catalytically active phases, transient states, and reaction mechanisms [63, 78-83]. As an example, using *in situ* E-TEM, Gai et al [78-83] has directly correlated the selectivity and reactivity of a catalyst with the formation and density of defects such as crystallographic shear (CS) planes in some oxide catalysts (e.g. Mo_3O, TiO_2, V_2O_5) in C_3H_6 and methanol oxidation reaction. The dynamic E-TEM observations have shown that CS defects in oxide catalysts form and grow by consuming anion vacancies and the correlation studies with the reactivity indicate that CS planes are detrimental to catalytic reactivity [63] and the CS planes are the consequence of catalyst reduction reactions rather than the origins of catalytic reactivity [79-81, 84].

The above *in situ* techniques can provide important fundamental insights into the catalytic mechanisms for specific catalyst structures. For example, they can help identify critical structural aspects controlling POM reactions, such as Cu orientation, Cu defect structure, and oxide nanostructure, while also measuring Cu catalyst performance using microreactor systems.

1.3 STRUCTURE AND PHASE CHANGE OF CU DURING REACTIONS

Clean copper surfaces are relatively inactive for methanol oxidation while the presence of oxygen strongly promotes the decomposition of methanol on copper [85-91]. In general, the standard method for determining the activity and performance of copper-containing catalysts includes a reductive pretreatment in a diluted hydrogen stream carried out *in situ* and prior to the activity measurement. The reduction pretreatment controls the structure and morphological characteristic of the catalyst surface. These initial characteristics play a central role in the evolution of the oxidation state and structural morphology during the reaction since the dynamic behavior of the catalyst surface is determined by the gas atmosphere under the reaction. However, the poor control in this pretreatment step in many studies contributes to the controversies in the literature. *In situ* techniques such as TEM are good at addressing the structure stability of different oxidation phases and surface defects under the POM reaction conditions, with the goal of gaining deeper insight into the elementary steps governing the catalytic reaction. This is because the reactivity of heterogeneous metal catalysts can be a strong function of the surface coverage of oxides, quantifying the structures, properties, and especially the conditions that produce various oxidation species is essential to developing both qualitatively and quantitatively correct models of surface reactivity.

The initial stage of forming oxides through surface oxidation features oxygen surface chemisorption. It has been observed that Cu(100), Cu(110) and Cu(111) surfaces exhibit different structures upon oxygen surface chemisorption which can significantly change the reactivity of methanol oxidation and methanol decomposition [92, 93]. As shown schematically in Figure 1, oxygen chemisorption on Cu(100) and Cu(110) results in restructuring of the surfaces with $\left(\sqrt{2}\times 2\sqrt{2}\right)$R45° O-Cu(100) and (2×1) O-Cu(110) structures, respectively [94-98]. The oxygen adsorption on Cu(111) results in the adlayer domains with ordered '29'-$\left(\sqrt{13}R46.1^\circ \times 7R21.8^\circ\right)$ and '44'-$\left(\sqrt{73}R5.8^\circ \times \sqrt{21}R-10.9^\circ\right)$ lattice structures comprising distorted hexagonal arrays of O atoms which were considered to be analogous to the planes of $Cu_2O(111)$ [99-103].

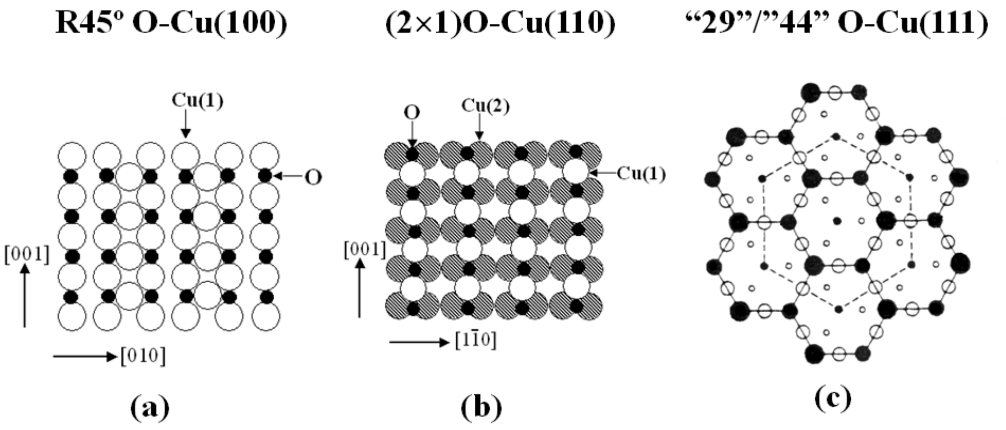

Figure 1. Oxygen chemisorption induced surface reconstruction on (a) Cu(100); (b) Cu(110); and (c) Cu(111).

Continued oxidation of the Cu surfaces will eventually lead to the formation of bulk oxides. The oxidation of Cu surfaces results in two oxide phases, Cu_2O or CuO, depending on the oxidation conditions. The information gap between the above surface-science studies and such bulk oxides for the POM reaction can be bridged by *in situ* environmental TEM, which is an ideal tool for visualizing the dynamic changes of nanoscale oxides.

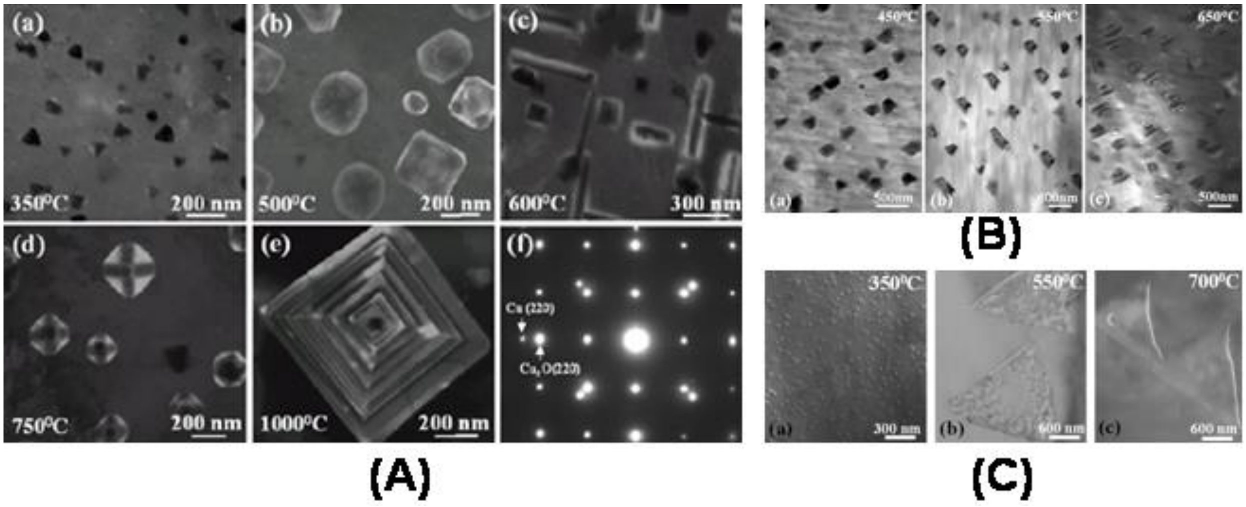

Figure 2. Effects of surface orientation and oxidation temperature on the morphology of oxide islands formed during the in situ oxidation ($P_{O2}=5\times10^{-4}$ Torr): (A) Cu(100); (B) Cu(110) and (C) Cu(111)

The Cu film can be cleaned *in situ* inside the TEM chamber by high-temperature annealing in hydrogen gas to remove any native oxide on the surfaces. The production of Cu oxide islands with controlled structure and phase can be achieved by oxidation of Cu under controlled conditions. Past study (Figure 2) has revealed that the structure and morphology of Cu oxide islands on Cu surfaces are sensitive to the oxidation conditions (e.g., temperature, oxygen gas pressure, surface orientation, etc.) [104-111]. By controlling the oxidation conditions inside the TEM, one can form Cu_2O on Cu surfaces. Electron diffraction is normally utilized to identify the phase and structure of the oxide islands on Cu surfaces. A sequential change in the oxide morphology/structure obtained by *in situ* oxidation of Cu surfaces inside the TEM will offer a wide variety of oxide structures and chemistry for establishing a comprehensive understanding of the structure-reactivity relationships of copper catalysts for the POM reaction.

2.0 OBJECTIVE

The major goal of this project is to elucidate the relationship between the structure/chemistry characteristics of copper catalysts and their reactivity. In spite of the widespread use of Cu-based catalysts for methanol reactions, a microscopic understanding of their role in these reactions is still lacking, especially in regard to the catalytically active sites and structural morphology. The objective of this study is to address these issues by a systematic examination of methanol oxidation over copper, copper oxides, and nanoparticle surfaces using *in situ* microscopy complemented with kinetics measurements. The *in situ* techniques enable us to create and/or modify the physical and chemical states of the catalyst surface as well as monitor structural changes *in situ* and microreactor studies of similar samples provide the kinetics measurements needed to elucidate the relationship between microstructures and reactivity/selectivity. The potential impact of this project is the identification of the critical structural factors that control the catalytic reaction of methanol oxidation that will lead to new fundamental understanding of the active sites and reaction mechanisms as well as strategies for designing new catalysts with tailored reactivity and selectivity.

In this project, nanoscale structure and morphology information were acquired by environmental transmission electron microscopy (E-TEM), the overall surface structure and chemistry through X-ray photoelectron spectroscopy (XPS). To correlate the structural changes to catalytic properties, kinetic measurements were also conducted from a microreactor system designed in the lab. Different crystal orientations of Cu thin films with Cu_2O nano-islands, Cu nanoparticles sitting on faceted ZnO rods and ZnO thin film were created as model catalysts to evaluate their hydrogen production ability in methanol partial oxidation. In addition, Cu-ZnO-based powder catalysts was also be synthesized as an analogue of the catalysts used in industry to enable a more direct comparison of performance with the model systems. The structural changes of various Cu surfaces, Cu oxides and Cu-ZnO interface were also measured using *in situ* transmission electron microscopy (TEM) to elucidate the critical structural and chemistry factors affecting reactivity, leading to a better microscopic picture of catalytic reactions.

3.0 ROLE OF CU OXIDATION STATES IN PARIAL OXIDATION OF METHANOL

3.1 INTRODUCTION

As mentioned in Chapter 1.0 , both Cu^0 and Cu^{1+} species have been considerred to be important for hydrogen production from methanol [59, 60]. However, other studies have also suggested that, under similar conditions, Cu^0 is active for methanol oxidation to H_2 and CO_2, Cu^{1+} is active for H_2O and CO formation, and Cu^{2+} – as the least active species – only produces H_2O and CO_2 [33, 35, 62]. Furthermore, recent work has indicated that co-feeding product gas (H_2 and CO_2) to the reaction can modify the oxidation state of Cu and hence its catalytic performance. This work suggested that higher Cu^0 and Cu^{1+} content leads to higher H_2 selectivity [62]. However, mechanistic insight into the correlation between Cu oxidation state and POM reaction selectivity is still largely lacking. Given the hypothesis that different Cu oxidation states can alter the reactivity and selectivity of POM reaction, this chapter aim to investigate the specific role of each Cu oxidation state in POM reaction.

In this chapter, 30 wt. % Cu/ZnO catalysts were synthesized and evaluated in POM. Methanol conversion, and H_2 and CO_2 selectivity were monitored as a function of the oxidation state of the active Cu phase in the catalyst, in order to elucidate correlations between these experimental observables with different O_2 feed conditions. X-ray photoelectron spectroscopy

(XPS) was used to characterize the Cu oxidation states of the catalyst at various stages of the reaction. Based on the experimental observations, POM reaction pathways on Cu_2O and Cu surfaces are proposed, and key assumptions are probed using density functional theory (DFT) calculations in order to gain an improved atomistic understanding of the POM mechanism as a function of reaction conditions.

This chapter is structured as follows. Chapter 3.2 provides experimental and computational methods and details. In the first two parts of Chapter 3.3, Cu/ZnO catalysts are synthesized and characterized using multiple techniques such as SEM, TEM, XRD, etc. Catalysts' performance is then evaluated during partial oxidation of methanol with inside a home-built microreactor which is essentially a fixed-bed set up. In the latter sections including Chapter 3.2.4 and Chapter 3.3.4, the impact of gas phase O_2 and reaction time to reactivity and selectivity of POM was showed. And an unexpected correlation between POM selectivity and Cu oxidation state concentration during the reaction was found. Chapter 3.4 discusses experimental results by proposing and verifying a new reaction mechanism of POM on Cu_2O surfaces, followed by conclusions.

3.2 EXPERIMENTAL SECTION

3.2.1 Catalyst Preparation

30 wt. % Cu/ZnO nanoparticle (NP) catalysts were prepared by co-precipitation from an aqueous zinc and copper nitrate solution. Specifically, $Cu(NO_3)_2 \cdot 3H_2O$ and $Zn(NO_3)_2 \cdot 6H_2O$ (both >99%, Sigma-Aldrich) were dissolved in deionized water (Milli-Q, 18.2 MΩ·cm) to make a 1 M metal nitrate solution with a mass ratio of Cu:Zn = 3:7. Na_2CO_3 (> 99%, Sigma-Aldrich) was dissolved

in deionized water to make 1 M solution as a precipitation agent. The mixed metal solution (50 ml) was added dropwise to 300 mL of deionized water at 70 ℃ under stirring. The pH was monitored by pH meter (OAKTON) and maintained at pH = 7 by adding Na_2CO_3 solution *via* a burette. The mixture was stirred at 70℃ for 2 h; during this time, the pH increased to ~8.4. The resulting blue precipitate was then separated by centrifugation and washed with deionized water until the pH was 7. The remaining paste was dried at around 90℃ in a vacuum oven overnight and calcined in air at 400℃ for 3 h.

3.2.2 Catalyst Characterization

X-ray diffraction (XRD; Bruker D8) was used to check the catalyst crystal phase, using CuK_α radiation at a wavelength of 1.54 Å, a beam voltage of 40 kV, and a current of 40 mA. The pattern was recorded with a 2θ range from 20° to 90° and a scanning rate of $3.5^\circ min^{-1}$. After baseline subtraction and smoothing via fast Fourier transform (FFT), the particle sizes of Cu, CuO, and ZnO were calculated using the Scherrer formula.

Scanning electron microscopy (SEM, JEOL JSM-6510LV) was used to determine the catalyst morphology at low magnification (X3300) with a beam voltage of 15 kV. In order to increase the electron conductivity of the sample and avoid charging effects, a thin palladium film was sputter-coated onto the sample surface before measurement. The elemental composition was determined by using an energy dispersive X-ray spectroscopy (EDX) detector mounted on the SEM device.

High-resolution transmission electron microscopy (HRTEM, JEOL JEM-2100F) was used to observe catalyst morphology at the nanoscale with an accelerating voltage of 200 kV. The TEM sample was prepared by re-dispersing powder in an ethanol solution, dropping solution on a Cu type-B support grid (Ted Pella, Inc.) and vacuum drying. The size distributions of the resulting NPs were determined using TEM images from various areas on the grid. ImageJ 1.47d (National Institutes of Health, USA) was used to measure NP sizes and generate a histogram. In order to generate an elemental mapping from the high-resolution image, different crystal phases were identified from FFT processed images of lattice fringes of the crystals. By applying masks on a given lattice position in an FFT processed image and inverting those positions, spatial locations of Cu and ZnO were obtained and colored in red and blue, respectively.

3.2.3 Reactivity Measurements

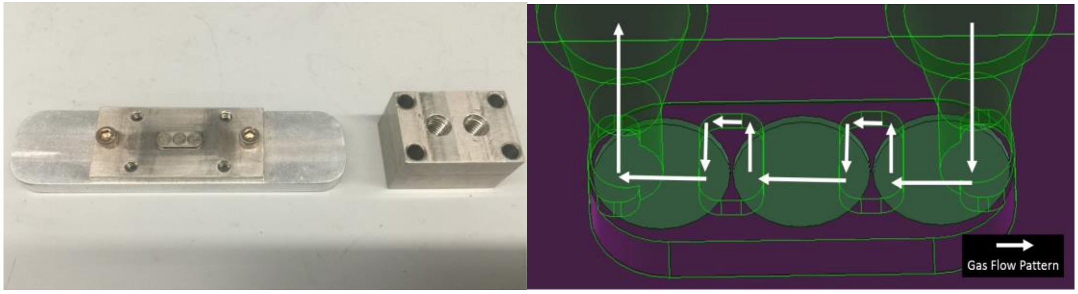

Figure 3. The microreactor(Left): sample boat that holds three TEM grids and Reactor lid with gas inlet and outlet. Schematic Schematic of gas flow pattern inside the microreactor.(Right)

The conversion of methanol (>99.8%, Fisher Scientific), as well as H_2 and CO_2 selectivities, were determined in an in-house manufactured microreactor made of an iron/chromium alloy coated with Au to avoid blind activity (as verified over the range of experimental conditions, Figure 3). The 30 wt% Cu/ZnO catalyst (2 mg) was packed inside the microreactor and methanol was introduced to the setup through a syringe pump at an injection rate of 0.127 cc/h. The entire setup was maintained at 200℃ via heating tape in order to avoid condensation of reactants or products. The molar ratio between O_2 (99.995%, Matheson) and methanol was controlled at 0.1, 0.3, and 0.5. Ar (99.995%, Matheson) was used as a carrier gas to maintain a fixed gas hourly space velocity (GHSV) of 3150 h^{-1}. Methanol molar concentration in the feed gas (MeOH, O_2, and Ar) was fixed at 62.5 mol%. The outlet gas composition which consisted of only H_2, H_2O, CO_2, CO and methanol was measured by a mass spectrometer (Pfeiffer Omnistar QMS 200), and the corresponding molar flow rates (ni) were calculated.

The experiments were run until steady state was attained (defined as no more than 10% change of measured concentrations over 10 min) which occurred within 1 h for all experiments shown. The selectivity (S) and conversion (X) of various gaseous products were calculated according to Equations (3-1) -(3-3):

$$X_{CH_3OH} = \frac{n_{CH_3OH,in} - n_{CH_3OH,out}}{n_{CH_3OH,in}} \times 100\% \tag{3-1}$$

$$S_{H_2} = \frac{n_{H_2}}{2 \times (n_{CH_3OH,in} - n_{CH_3OH,out})} \times 100\% \tag{3-2}$$

$$S_{CO_2} = \frac{n_{CO_2}}{n_{CH_3OH,in} - n_{CH_3OH,out}} \times 100\% \tag{3-3}$$

Since CO, CO_2, H_2, and H_2O were the only detectable products, CO and H_2O selectivities are simply the “mirror image” of CO_2 and H_2 selectivities (i.e. S_{CO2}= 1-S_{CO2} and S_{H2O}= 1-S_{H2}). In order to check the accuracy of the reactivity measurements, the carbon molar balance was calculated and found to be within <10% for all reported experiments [Equation (3-4)].

$$n_{CH_3OH,in} = n_{CH_3OH,out} + n_{CO} + n_{CO_2} \tag{3-4}$$

3.2.4 Analysis of Cu Oxidation State

X-ray photoelectron spectroscopy (ESCALAB 250XI, Thermo Scientific, Inc.) was used to determine the Cu oxidation states in the catalysts *ex-situ* after undergoing POM for various extents of time. After a specified time interval, the reaction was stopped by purging the system with Ar gas flow, and the sample was cooled to room temperature in Ar flow and stored under vacuum for transfer to XPS analysis. A fresh catalyst sample was used for measurement at each time interval. Cu $L_3M_{45}M_{45}$ Auger spectra were obtained for each sample with a monochromated, micro-focused Al Kα X-ray source (spot size = 200 µm; step size = 0.1 eV, pass energy = 50 eV). In order to identify and quantify Cu oxidation states from Cu Auger spectra, reference spectra of each copper oxidation state were collected from pure Cu NPs with similar particle size by the same instrument. Each reference spectrum has a characteristic peak at an electron kinetic energy of 918.7 eV, 916.8 eV, and 917.6 eV for Cu, Cu_2O, and CuO, respectively. The quantification of Cu oxidation states *via* Cu Auger lines was implemented following Holse et al. [112]. A linear combination of three reference spectra was fitted to Cu $L_3M_{45}M_{45}$ Auger lines collected *via* XPS, and the relative amount of each oxidation state was determined from this fit. The errors in the relative ratios were determined at the 99% confidence level, or 3 standard deviations (3σ) of the mean relative ratio values.

3.2.5 First-Principles Calculations

Theoretical calculations that are included in this chapter were conducted by collaborators. First-principles DFT calculations were performed using the Vienna Ab-initio Simulation Package (VASP)[113-116] with the PW91 parameterization of the generalized gradient approximation (GGA) functional[117] and projector augmented wave (PAW)[118, 119] pseudopotentials. Atomic structures and charge differences were visualized via the VESTA package [120, 121]. The climbing image nudged elastic band (CI-NEB) method[122] was applied to calculate POM reaction energy barriers, applying five intermediate images between initial and final stable adsorption states. In order to account for the strong electronic correlation shown to affect the energetics of Cu_2O and related systems, [123, 124] the rotationally invariant Dudarev implementation of the Hubbard U model was used to account for electron-electron interaction error in DFT calculations, combining both Coulombic and exchange terms into a single effective U parameter (U_{eff}) to account for exchange-correlation errors on Cu 3*d* orbitals[125]. To account for Hubbard U induced changes on Cu-O structures adjacent to reactant species and related energetics [126, 127]. An *a priori* resolved bulk Cu_2O U_{eff} value of 7.45 ± 0.54 eV was found, which was applied to Cu in surface calculations as 7.5 eV. [128, 129] Relative to past research, the measurement uncertainty in this Hubbard U calculation spans the effect magnitude (about 0.3 eV) observed when changing the coordination of oxygen-bonded metal atoms in similar surface systems [130], while also being consistent with previously fitted empirical properties involving Cu-O bulk and surface systems. [69]

Cu_2O surfaces were simulated by slabs including 4 Cu layers. Since the unit cell sizes associated with the (100), (110) and (111) surfaces differed, different periodic surface repetitions were applied to obtain similarly sized surfaces. The bottom two layers of each surface were fixed at their bulk determined positions, while all other atoms were allowed to fully relax during structural optimization. Overall, structural specifications for modeling the surfaces studied in this work were established through past work on related systems [131].

3.3 RESULTS

3.3.1 Cu/ZnO Characterization

30 wt% Cu/ZnO catalysts were synthesized by co-precipitating copper nitrate and zinc nitrate aqueous solution and calcination in air at 400℃, resulting in the formation of copper oxide and zinc oxide. Subsequent reduction with H_2 under 250℃ for 2 h reduced the CuO phase, yielding the final Cu^0/ZnO catalyst[32, 33, 60]. Characterization of the powdered catalysts by XRD (Figure 4) confirms that Cu oxide was reduced to metallic Cu while ZnO remained oxidized under these conditions. Based on Scherrer’s equation, the crystallite sizes of CuO and ZnO after calcination were calculated to be 4.0 nm and 7.8 nm, respectively. After reduction, Cu and ZnO showed crystallite sizes of 6.7 nm and 10.3 nm, respectively.

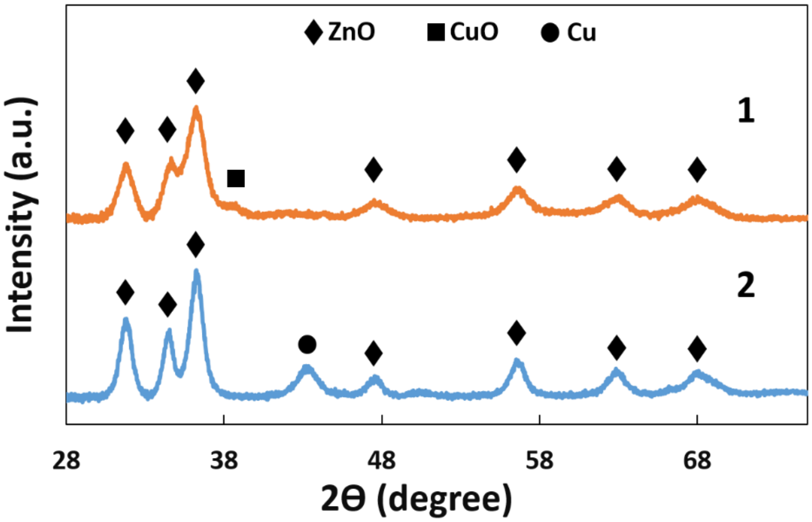

Figure 4. Powder XRD patterns of as-prepared CuO/ZnO (1) and Cu/ZnO after being reduced in H_2 at 250 ℃ for 3 h (2).

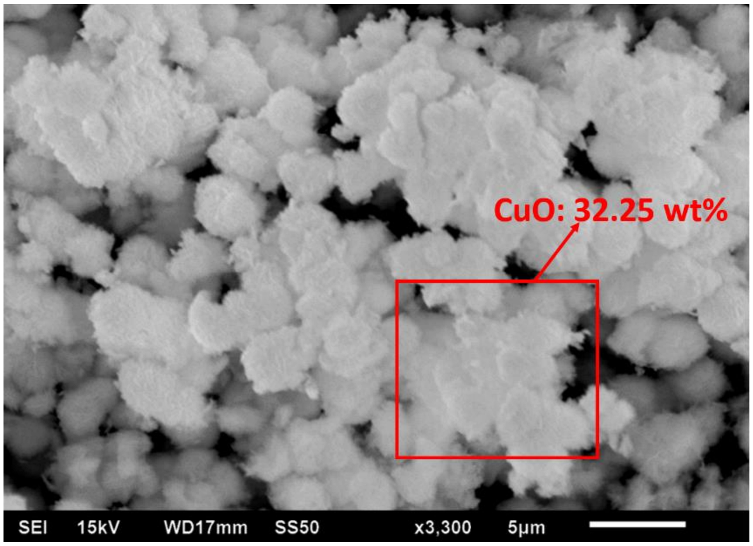

Figure 5. SEM image of CuO/ZnO as prepared. EDX indicates 32.25 wt% CuO for the area marked by the red box.

SEM measurements (Figure 5) reveal the morphology of the CuO/ZnO catalyst. EDX measurements show a weight loading of CuO 32.25wt%, close to the initial mass ratio applied during synthesis (Cu:Zn = 3:7). Cu and ZnO NPs are randomly dispersed in the catalyst (see Figure 6B) and show similar sizes with a fairly narrow size distribution and an average particle size of 7.31 ± 1.49 nm (inset, Figure 6), in good agreement with the particle sizes calculated from XRD. HRTEM (Figure 6) confirms the random localization and spatial elemental distributions of Cu and ZnO on the nanoscale.

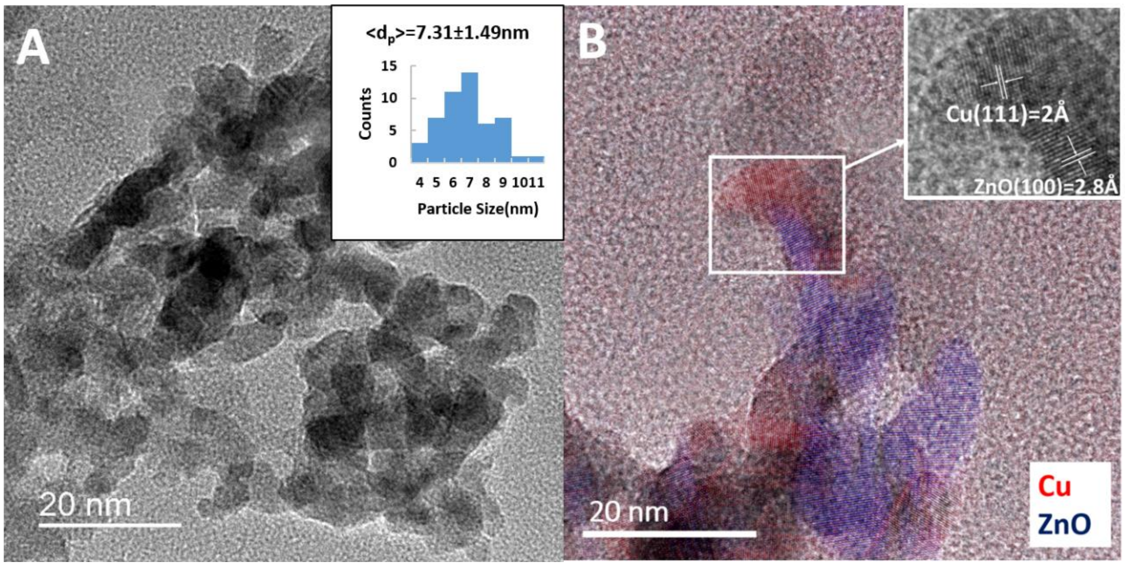

Figure 6. (A) TEM image of the Cu/ZnO NPs after reduction. Inset: Cu and ZnO NP size distribution. (B) HRTEM image with superimposed (colored) crystal phase domains of Cu and ZnO. Inset: Example of a high magnification image showing Cu and ZnO lattice spacing.

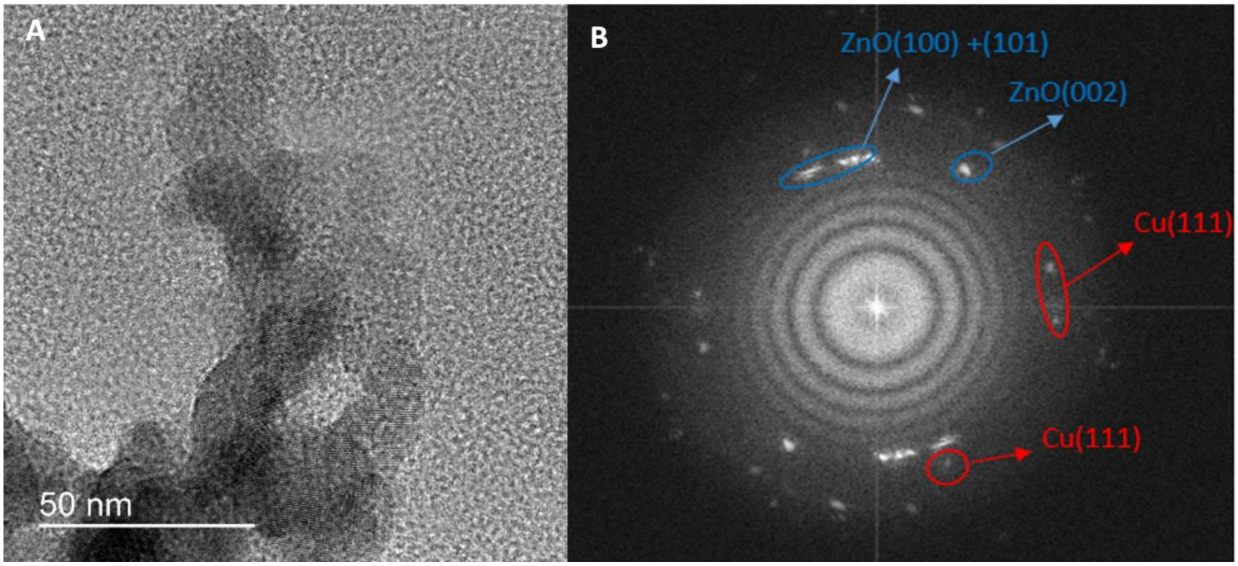

Figure 7. High-resolution TEM image of 30% Cu/ZnO. (b) Fast Fourier Transform (FFT) shows crystal lattice vectors.

3.3.2 Impact of O_2/MeOH Molar Feed Ratio on POM Reactivity

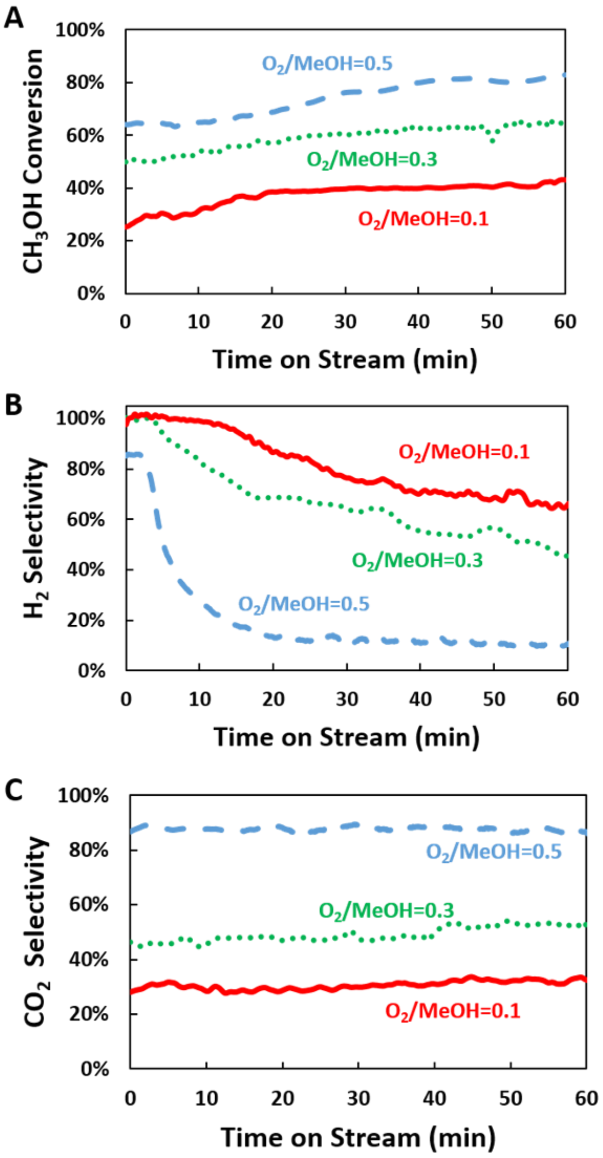

Figure 8. POM reactivity measurements showing the methanol conversion (A), H_2 selectivity (B), and CO_2 selectivity (C) vs. time-on-stream during POM at 250℃ for three different O_2/MeOH molar ratios (red = 0.1, green = 0.3, and blue = 0.5). MeOH conversion increases and H_2 selectivity decreases with O_2/MeOH molar ratio and time-on-stream. CO_2 selectivity increases with O_2/MeOH molar ratio but remain constant with time-on-stream.

The catalytic performance of the 30 wt% Cu/ZnO during the partial oxidation of methanol (POM) was evaluated in a microreactor setup. Figure 8 shows measurements of POM reactivity at 250^{o}C for three different O_2/MeOH molar feed ratios.

The conversion of methanol as a function of time-on-stream is shown in Figure 8A. At O_2/MeOH = 0.1, methanol conversion increases from 25% to about 40% after 1 h. With increasing O_2/MeOH ratio, methanol conversion increases overall and continues to show this increase with time on stream (from 52% to 64% for O_2/MeOH = 0.3, and from 63% to 81% for O_2/MeOH = 0.5 over 1 h time-on-stream). It is reasonable to assume that these gradual increases result from a slow oxidation of the Cu phase in the catalyst, increasing the availability of lattice oxygen for the partial oxidation reaction. Since the relative concentration of O_2 in the feed is below or equal to the O_2/MeOH stoichiometric ratio of 0.5, O_2 is a limiting reactant and O_2 conversion is hence complete at all three feed ratios (not shown here).

Selectivity of the POM reaction is shown in Figure 8B and 8C for H_2 and CO_2 formation, respectively. H_2 selectivity (Figure 8B) starts at 100% and 86% for O_2/MeOH = 0.3 and 0.5 and subsequently drops to 70% and 15%, respectively. For O_2/MeOH = 0.1, the H_2 selectivity is maintained at ~100% for 15 min and then decreased gradually over time. Finally, for the stoichiometric feed (O_2/MeOH = 0.5), H_2 selectivity levels off after ~20 min time on stream at 15% and remains unchanged for the remainder of the reaction time.

Unlike the significant change observed in H_2 selectivity, CO_2 selectivity (Figure 8C) remains constant over the entire reaction time (~1h) but drops significantly with decreasing of O_2/MeOH ratio from 88% (O_2/MeOH = 0.5) over ~50% (O_2/MeOH = 0.3), to ~30% (O_2/MeOH = 0.1).

Overall, these results show, unsurprisingly, that both conversion and selectivity in POM strongly depend on oxygen availability, i.e. on the O_2 concentration in the gas phase: Higher O_2 partial pressure leads to higher methanol conversion, lower H_2 selectivity, and higher CO_2 selectivity. This is consistent with prior reports in the literature [32, 132] and is an expected result since increasing availability of the oxidant (O_2) as the limiting reactant at these conditions will result in increased conversion and deeper oxidation of the fuel (methanol).

However, the difference in behavior over time between H_2 selectivity and CO_2 selectivity is surprising: If this trend is correlated with a change in catalyst oxidation state, one would assume that the same trend (i.e. increase or decrease in selectivity) would likely be observed for the selectivity along both the C and the H oxidation pathways. Therefore, the oxidation state of the catalyst at various stages of the reaction was further investigated.

3.3.3 Change of Cu Oxidation State during POM

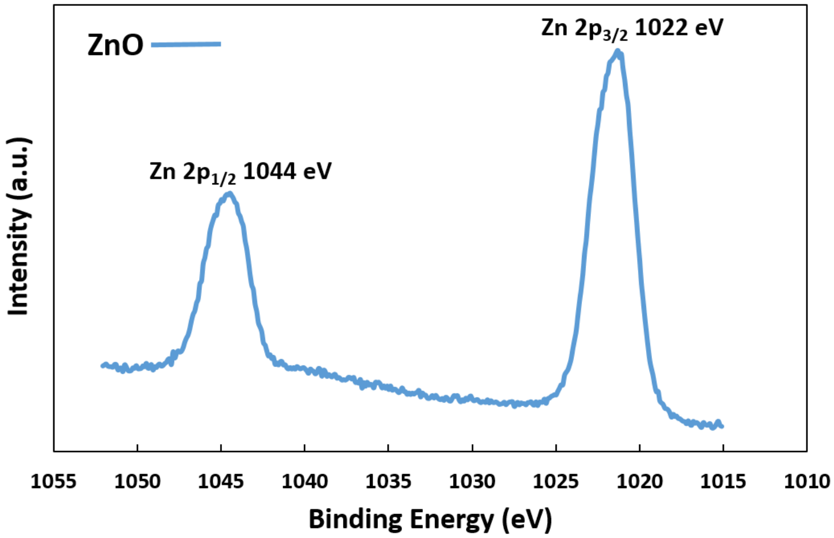

Figure 9. XPS core level spectra of ZnO showing the Zn 2p binding energy. The sample was collected after the reaction (250℃, O_2/MeOH=0.1).

In order to trace the oxidation state of Cu in the catalyst during the reaction, the samples were quenched *via* Ar purge and cooled to room temperature, followed by transfer under a vacuum to XPS studies. Previous studies reported that ZnO remains in its oxidized form during POM [34, 133-135], which was also confirmed from the present study (Figure 9). In contrast, Cu is easily oxidized and reduced at POM conditions, and the Cu oxidation states present in the Cu/ZnO-catalysts were hence determined from the positions of the Cu Auger $L_3M_{45}M_{45}$ peaks. Cu^0 and Cu^{1+} present very similar Cu $2p_{3/2}$ peak positions of ~932.8 eV but show distinct Cu $L_3M_{45}M_{45}$ energies of 918.7 eV and 916.8 eV, respectively, with the Cu^{2+} $L_3M_{45}M_{45}$ peak positioned at 917.6 eV [33, 35, 62] (Figure 10). Therefore, Cu $L_3M_{45}M_{45}$ Auger spectra were collected to analyze Cu oxidation states.

Figure 11 shows representative Cu $L_3M_{45}M_{45}$ Auger spectra taken after different times on stream during POM for a feed ratio (O_2/MeOH) of 0.1. The spectra confirm qualitatively that Cu^0 is being gradually oxidized to Cu_2O throughout the POM reaction. A similar analysis was conducted for samples collected at 0.3 and 0.5 O_2/MeOH feed ratios (Figure 12 and Figure 13).

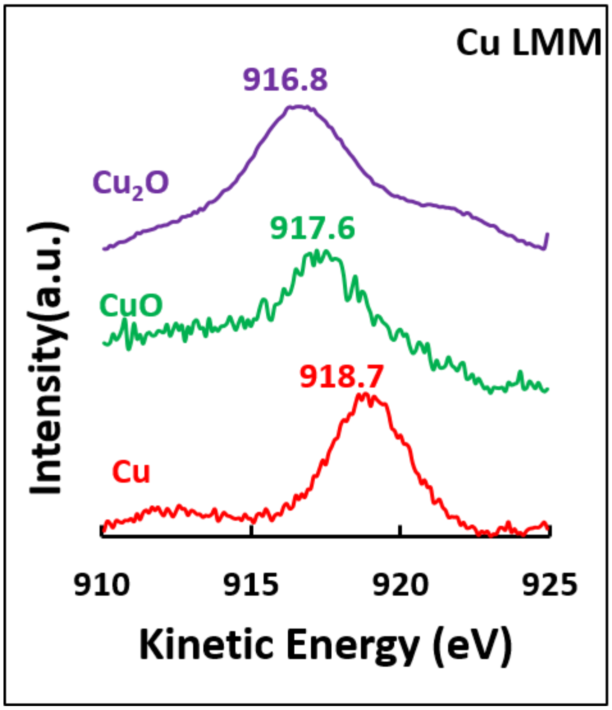

Figure 10. Reference spectra of each copper oxidation state collected from pure Cu NPs. Each reference spectrum has a characteristic electron kinetic energy of 918.7 eV, 916.8 eV, and 917.6 eV for Cu, Cu_2O, and CuO, respectively. The fits in Figure 11, Figure 12 and Figure 13 are obtained by fitting a linear combination of the three Cu $L_3M_{45}M_{45}$ basis reference spectra.

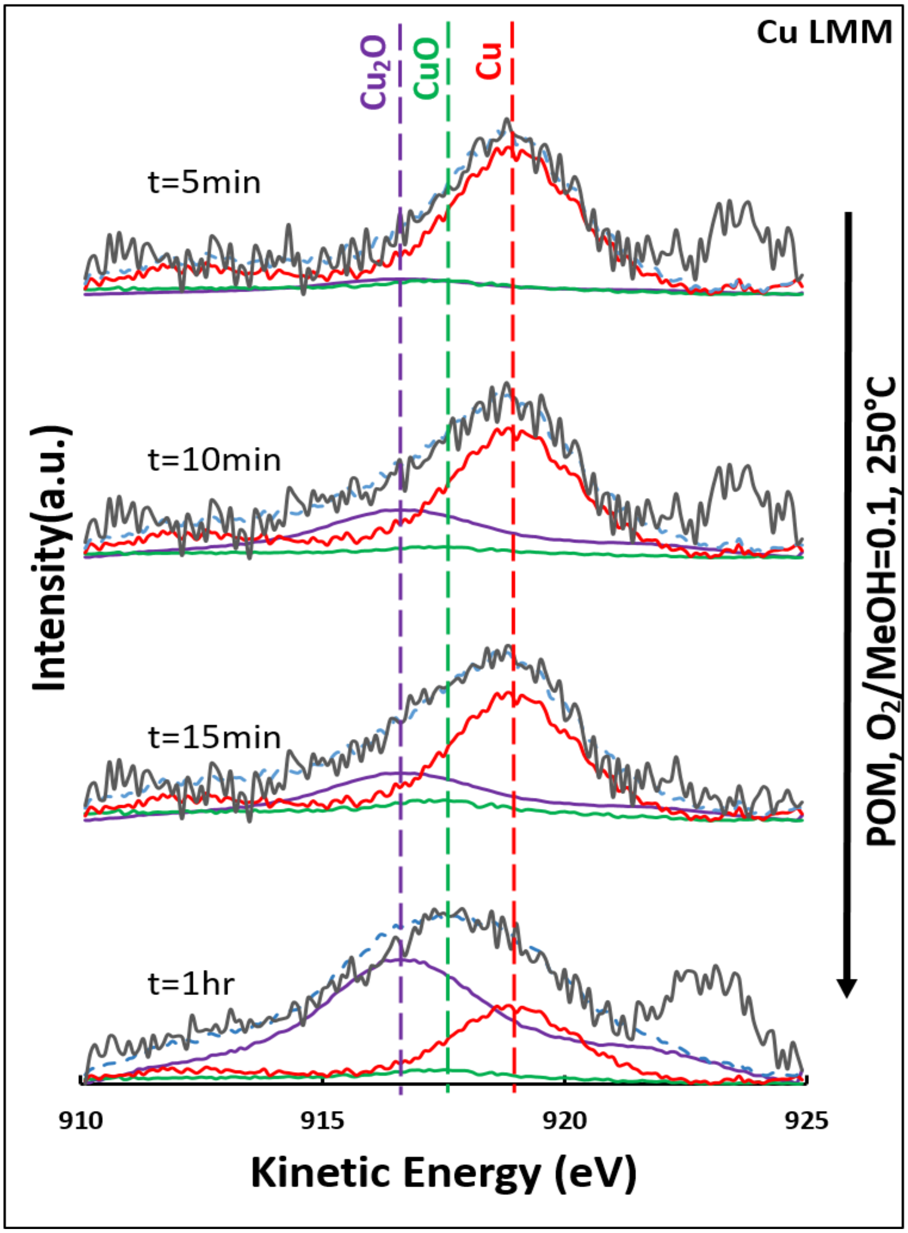

Figure 11. Changes to the XPS Cu $L_3M_{45}M_{45}$ feature during POM at 250℃, O_2/MeOH = 0.1. Data points are shown as black lines, while the light blue dashed lines indicate fitted results. The vertical lines indicate peak position for Cu (red), CuO (green), and Cu_2O (purple). The fit is obtained by fitting a linear combination of three Cu $L_3M_{45}M_{45}$ basis reference spectra (see Figure 10).

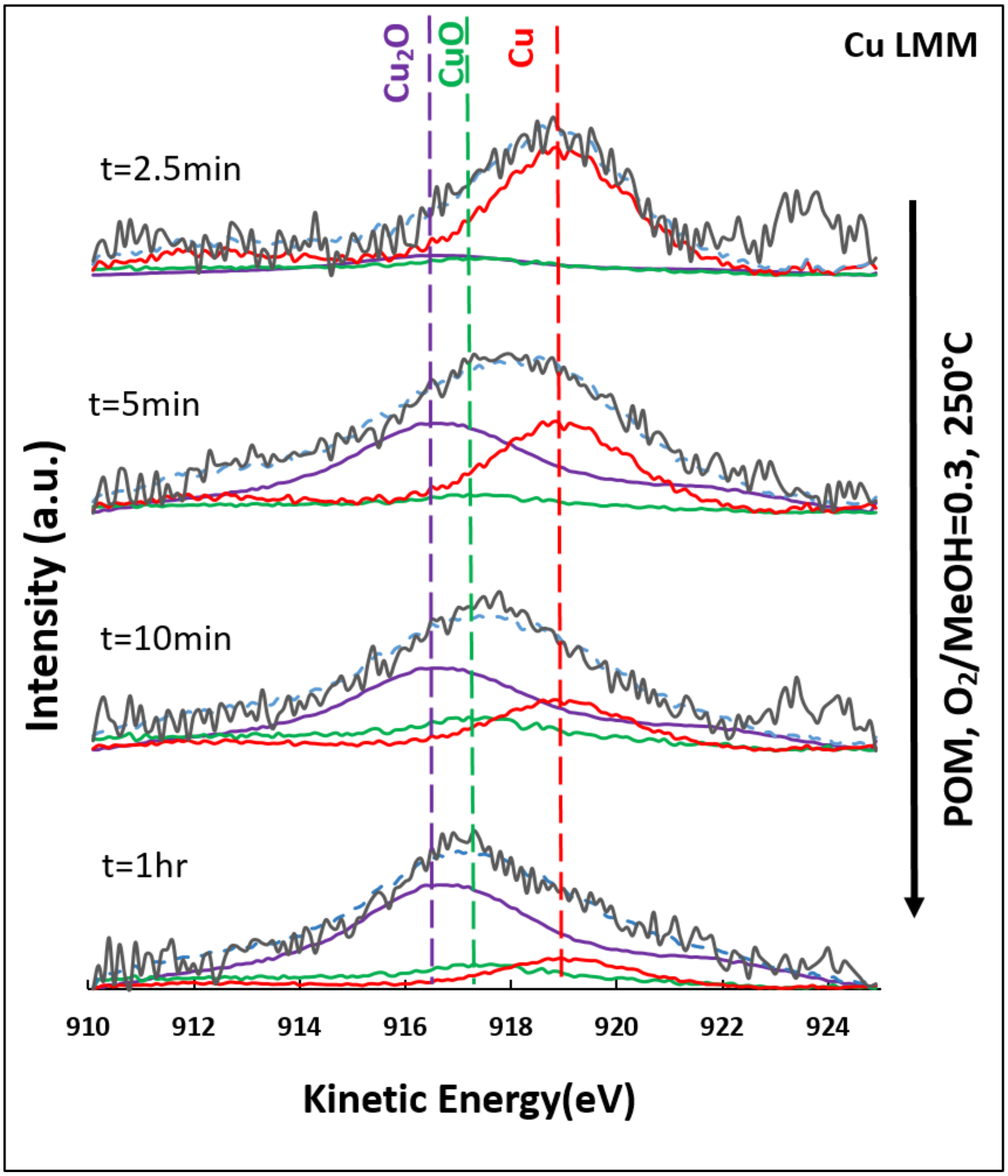

Figure 12. Changes to the XPS Cu $L_3M_{45}M_{45}$ feature during POM at 250℃, O_2/MeOH=0.3. Data points are shown as black lines, while the light blue dashed lines are fits. The vertical lines indicate peak positions for Cu (red), CuO (green), and Cu_2O (purple).

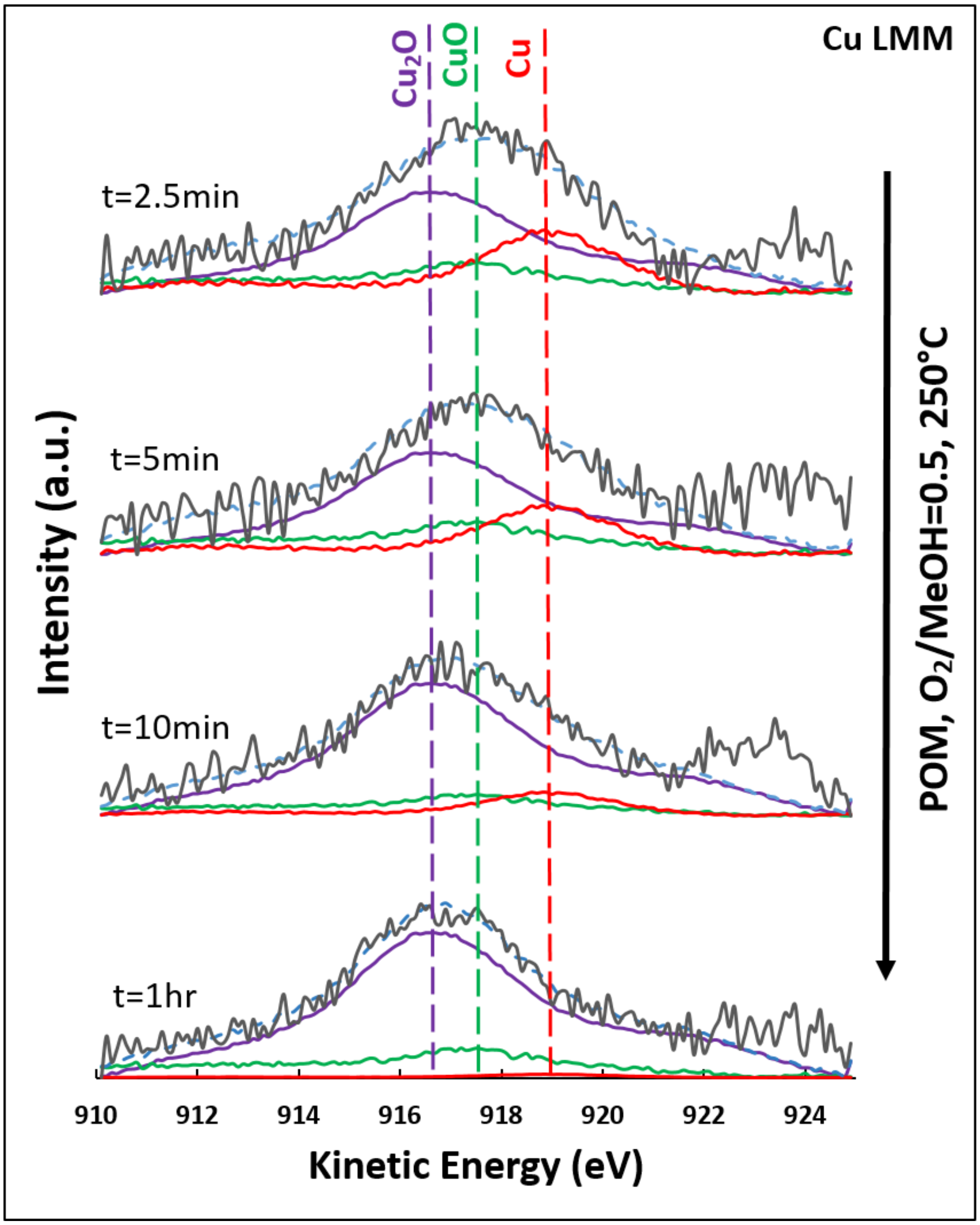

Figure 13. Changes to the XPS Cu $L_3M_{45}M_{45}$ feature during POM at 250℃, O_2/MeOH=0.5. Data points are shown as black lines, while the light blue dashed lines are fits. The vertical lines indicate peak positions for Cu (red), CuO (green), and Cu_2O (purple).

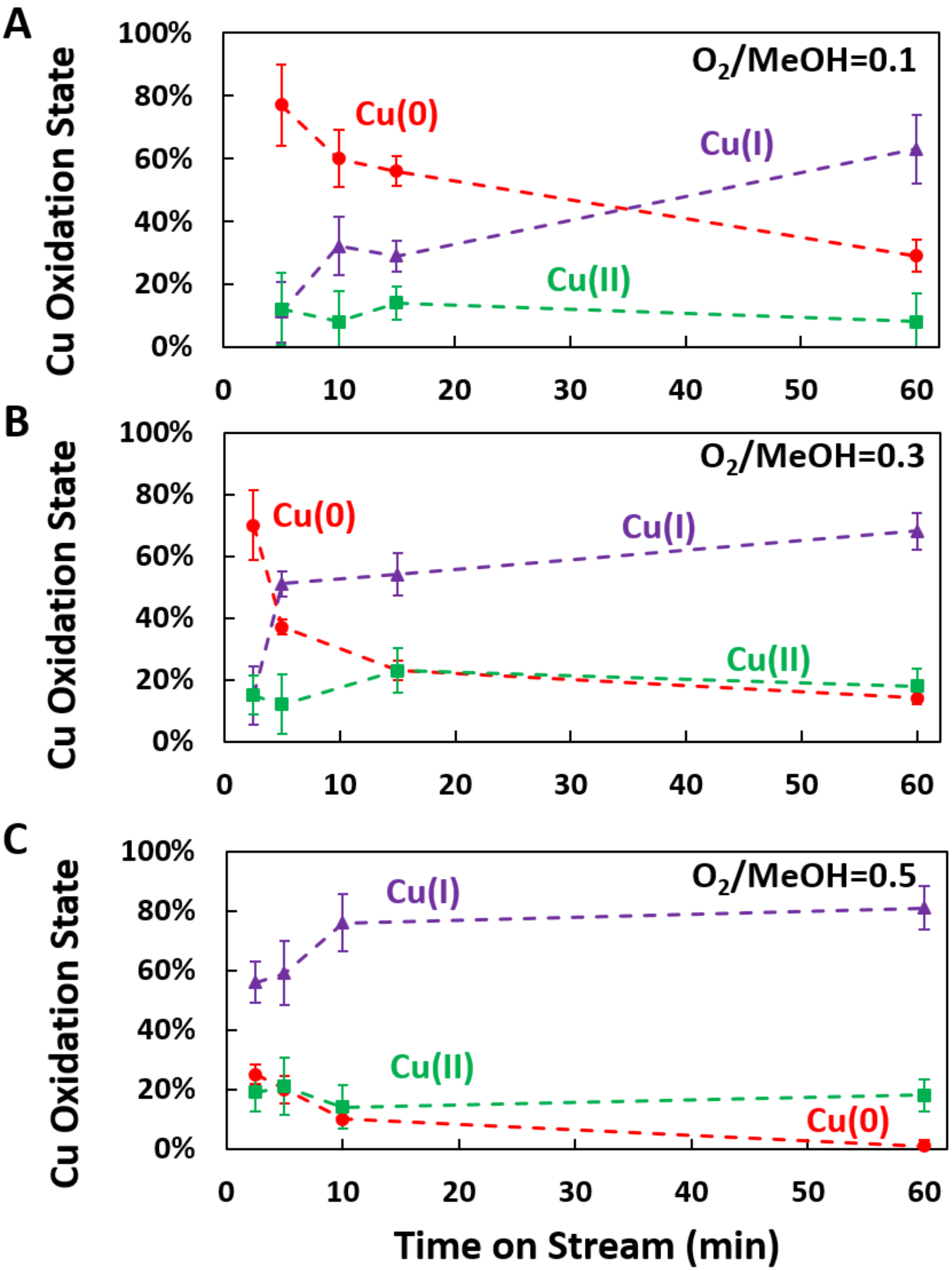

Figure 14. The relative amount of each Cu oxidation state observed in the catalyst as a function of reaction time at the three molar O_2/MeOH feed ratios of 0.1 (A), 0.3 (B), and 0.5 (C).

This observation is quantified further in Figure 14, where the XPS data for the three different feed ratios are summarized by showing the relative percentage of Cu^0, Cu^{1+}, and Cu^{2+} vs time-on-stream. For the lowest O_2/MeOH ratio of 0.1 (Figure 11), one can see that 5 minutes after the start of the reaction, the relative Cu^0 concentration has dropped from 100% to 80% and subsequently decreases further to ~30% at t=1 h. In parallel, the relative Cu^{1+} concentration increases from 10% to > 60%. The Cu^{2+} concentration remains at ~10% or below for the entire duration of the reaction, indicating that oxidation to Cu^{2+} is hindered by the low oxygen availability.

Figure 14B and Figure 14C show the temporal evaluation of Cu for the other two O_2/MeOH ratios studied (0.3 and 0.5, respectively). Changes in Cu oxidation state follow the same trends as those described above for O_2/MeOH = 0.1. However, with increasing O_2 concentration in the gas phase, the oxidation of Cu^0 proceeds more rapidly and Cu^{1+} quickly becomes the dominant oxidation state in the catalyst. Specifically, for O_2/MeOH = 0.5, the Cu^{1+} concentration rapidly increases from 0% to almost 60% already after 5 min on stream, while at the same time this concentration only increased to ~50% and 10% for O_2/MeOH = 0.3 and 0.1, respectively.

Overall, these results demonstrate that the Cu oxidation state in the Cu/ZnO catalyst is changing dynamically during POM and that this change is strongly influenced by the feed composition. Cu^{2+} remains below 20% at all conditions and shows no significant change over time, indicating that it is not a reaction-relevant species. The dominant Cu oxidation state over a wide range of reaction conditions is Cu^{1+}, in agreement with previous reports [133].

3.3.4 Effect of Cu Oxidation State on POM Selectivity

In order to illustrate correlations between reactivity and Cu oxidation state, Figure 15 combines the results from the reactivity studies (Figure 8) and the XPS investigations (Figure 14). Figure 15 plots methanol conversion and H_2 and CO_2 selectivities vs. relative amounts of oxidized Cu species (i.e. Cu^{1+} and Cu^{2+}) in the catalyst over time, displaying all three O_2/MeOH feed ratios studied (O_2/MeOH = 0.1, circles; O_2/MeOH = 0.3, triangles; and O_2/MeOH = 0.1, squares).

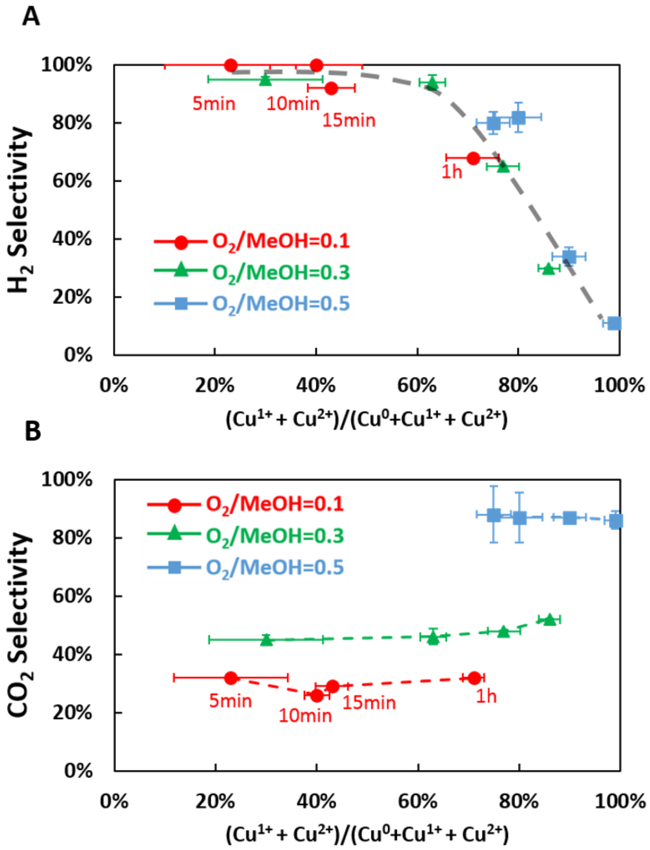

Figure 15. H_2 selectivity (A) and CO_2 selectivity (B) versus percentage of combined oxidized Cu during the POM reaction at 250 °C and over three different O_2/MeOH molar ratios (red circles = 0.1, green triangles = 0.3, and blue squares = 0.5).

Remarkably, the H_2 selectivity data gathered at the three different feed ratios collapse onto a single curve (Figure 15A), i.e. H_2 selectivity appears to *only* depend on the (average) Cu oxidation state in the catalyst: H_2 selectivity is near 100% up to ~50% Cu^0 content, and then drops rapidly with further increase in the degree of Cu oxidation (Cu^{1+} and Cu^{2+}) in the catalyst. This apparent oxidation of H_2 with lattice O in Cu oxides, reducing Cu oxides while producing H_2O, is in agreement with previous reports [33, 35, 60, 62, 133]. The O_2 concentration in the gas phase hence seems to impact H_2 selectivity only indirectly via controlling the oxidation state of Cu.

In contrast to that, Figure 15B shows that CO_2 selectivity has virtually no correlation with the Cu oxidation state as CO_2 selectivity remains constant over a wide range of Cu^0 concentrations at any given O_2/MeOH ratio. Instead, CO_2 selectivity depends strongly on the O_2 concentration in the feed gas. This observation contradicts previous work, which suggests, somewhat counter-intuitively, that Cu^0 favors formation of CO_2 and Cu^{1+} favors CO formation [33]. However, the transient, time-resolved reactivity measurements in the present study (compared to steady-state measurement in the previous work) [33] enable us to capture the temporal dynamics of the reaction kinetics and thus reveal a rather clear and unambiguous correlation of CO_2 selectivity with gas phase oxygen, rather than lattice oxygen.

Overall, results in this chapter thus show that H_2 production is entirely controlled by the Cu oxidation state, while no correlation between CO_2 production and Cu oxidation state is observed and CO_2 production is entirely governed by the oxygen partial pressure in the gas phase. Furthermore, the concentration of Cu^{1+} increases with reaction time, consistently becoming the dominant Cu oxidation state at each feed condition as the reaction approaches steady state. This suggests different reaction pathways of the metallic Cu and Cu_2O surfaces, respectively, observed at the earlier and later stages of the POM reaction, which will be further discussed below.

3.4 DISCUSSION

3.4.1 Proposed POM mechanism on Cu and Cu_2O

Overall, results showed above suggest that the POM reaction mechanism is controlled both by the oxidation state of the catalyst and the prevalence of gas-phase oxygen. It seems hence helpful to break down the mechanistic discussion of the reaction into four cases: POM on metallic (Cu^0) and on oxidized (Cu^{1+}) surfaces, respectively, each in the presence and absence of gas phase oxygen, respectively.

Numerous mechanisms for POM on Cu^0 surfaces have been derived either experimentally or theoretically [59, 132, 136-138]. As previous studies have mentioned, the overall reaction pathway for POM may be considered as a combination of partial oxidation, steam reforming, methanol decomposition, water-gas shift, and reverse water-gas shift reactions, all of which share the same set of reaction intermediates [132]. In fact, POM on Cu^0 surfaces also shares reaction intermediates with methanol synthesis from H_2 and CO_2 (a slightly modified inverse reaction to POM) such as CH_3O^*, CH_2O^*, and $HCOO^*$ that are well-studied in the literature [72, 126, 139]. Therefore, the POM reaction mechanism on Cu^0 surfaces is summarized in Figure 16A: In the presence of gas phase oxygen (Pathway A), the reaction starts with O-H bond activation facilitated by chemisorbed O on the surface. The resulting CH_2O^* is further oxidized by neighboring OH^* to form $HCOOH^*$ and then $HCOO^*$. Finally, decomposition of $HCOO^*$ gives CO_2 and H_2 as final products [62, 140]. In the absence of O_2 in the feed gas (Pathway B), methanol will follow a decomposition pathway on metallic Cu to generate CO and H_2, i.e., the reverse reaction of methanol synthesis via CO hydrogenation, as shown in Figure 16B [141]. Both of these mechanisms on a Cu^0 surface have been studied in detail before and are hence supported by multiple studies in the existing literature [33, 37, 132, 133, 136, 142].

In contrast, very few studies investigated the influence of Cu oxidation state on the POM mechanism [143]. Therefore, a mechanism for POM on Cu_2O is proposed in order to explain the impact of the Cu oxidation state on POM selectivity observed in experiments.

Figure 16C illustrates the proposed POM reaction pathway on Cu_2O in the presence of gas phase oxygen. CH_3OH, CH_3O^* and CH_2O^* bond to Cu_2O surfaces via their O atoms, according to previous studies [69]. The H atom from dissociative methanol adsorption bonds to lattice oxygen and can reduce the oxide surface via water formation [126]. In the presence of gas phase O_2, O vacancies resulting from this desorption can be refilled quickly by chemisorbed O [144]. In contrast with the reaction pathway on Cu^0 (Figure 16A), in which CH_2O^* is oxidized by adjacent OH^* to form $HCOOH^*$, the corresponding pathway on Cu_2O (Figure 16C) features further decomposition of CH_2O^* to CHO^* via O-H bond activation is proposed [126]. The CHO^* on Cu_2O then gives H to neighboring lattice O, subsequently becoming further oxidized by OH^* to $COOH^*$ via a reverse water gas shift reaction step[145]. In this proposed mechanism, further decomposition of $COOH^*$ will then yield CO_2 as the final product [126, 145].

In contrast, the POM reaction pathway on Cu_2O in the absence of gas phase oxygen (Figure 16D) is proposed to proceed via a sequence of CH_3OH dehydrogenation steps, since there is no surface O to facilitate OH^* formation. This sequence forms CO as a final product, while the dissociated H^* atoms will be oxidized by lattice O and form H_2O as the final product.

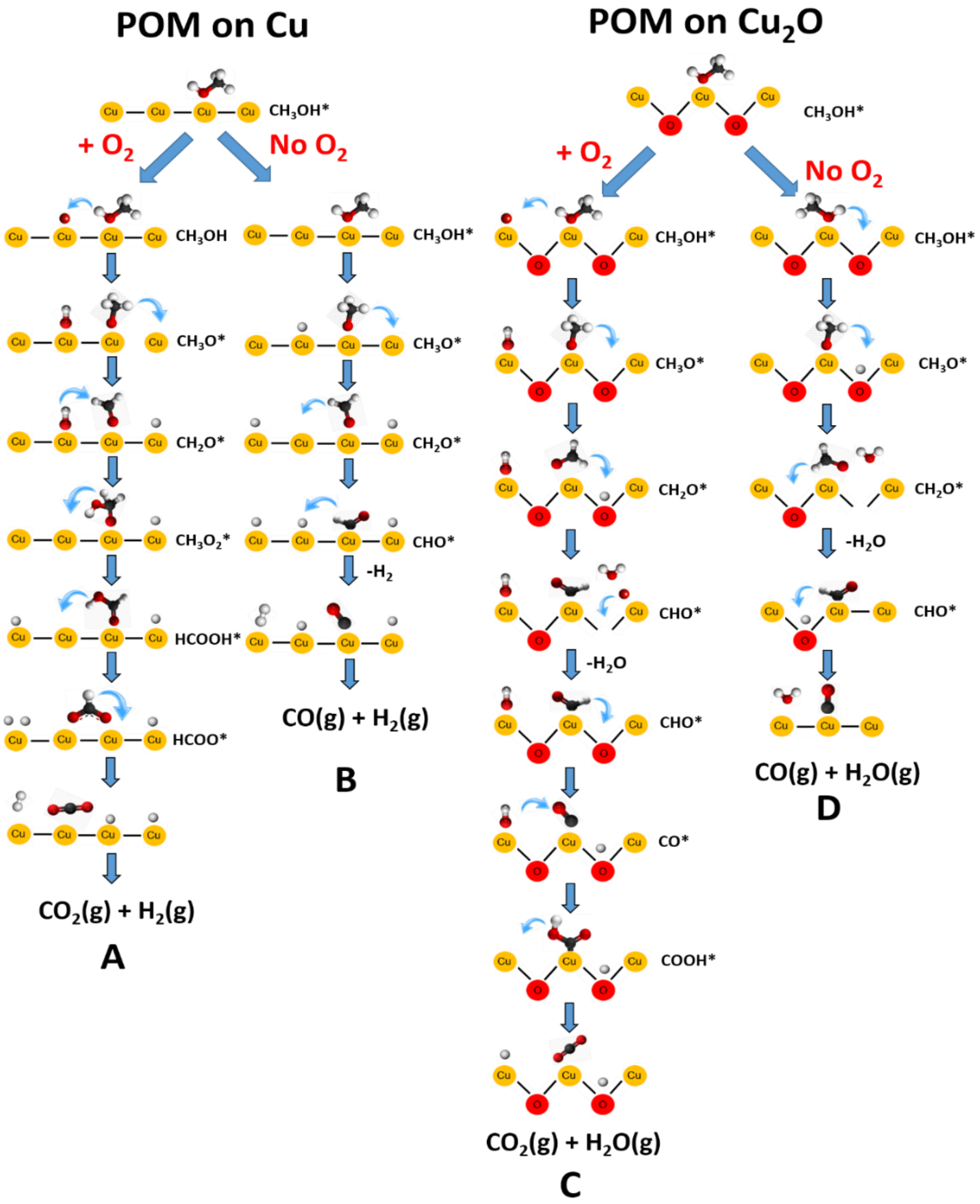

Figure 16. Proposed schematic reaction pathway of POM on Cu and Cu_2O at different feed conditions, namely: POM (A) and methanol decomposition (in the absence of gas phase O_2; B) on metallic Cu, respectively, and POM in the presence (C) and in absence of gas phase O2 (D) on Cu_2O. Atoms C (black), H (white), O (red), and Cu (yellow) are colored accordingly.

3.4.2 First-Principles Evaluation of Proposed Reaction Mechanisms

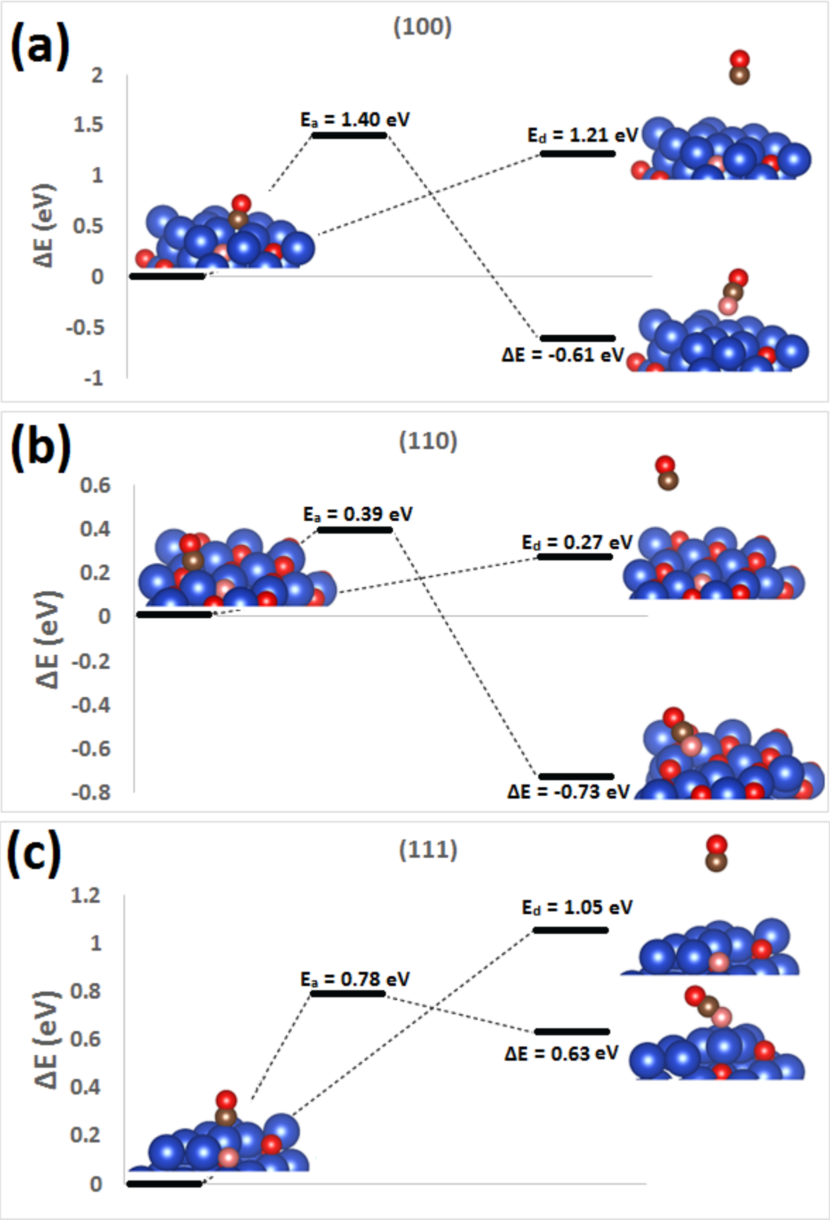

Figure 17. Energy differences and activation barriers for CO_2 formation and CO desorption on Cu_2O (a) (100), (b) (110), and (c) (111) surfaces. Atoms C (brown), Cu (blue), O (red; marked in light red if the lattice O is used to form CO_2) are colored accordingly.

The proposed mechanisms are consistent with the experimental observations summarized in Figure 15: Regarding the dependence of H_2 selectivity on Cu oxidation state, the proposed mechanisms show a switch from H_2 to H_2O as a predominant final product when moving from metallic Cu to Cu_2O, since lattice O can be accessed by H and removed *via* water formation. Therefore, H_2 selectivity is controlled by the Cu oxidation state. This observation is further supported by recent literature which indicates that the energy barrier of forming H_2 from associative desorption of two H* (0.29 eV) is much lower than the energy barrier of forming H_2O from H* and OH* (1.39 eV) on Cu(111) surfaces[126, 127]. Similar results can also be found on the Cu(110) surface[137]. Thus, H_2 formation would be energetically favored over H_2O on Cu surface ever with O_2 present in the gas phase.

As to CO_2 selectivity, in agreement with experimental observations, the formation of CO_2 is favored over the formation of CO in the presence of gas phase oxygen (Figure 16A, Figure 16C). Switching from Cu (Figure 16A, Figure 16B) to Cu_2O (Figure 16C, Figure 16D) does not shift the preference of product formation from CO to CO_2, mainly because lattice O does not directly interact with adsorbed CO species.

The methanol synthesis/POM reaction system has been studied previously in much detail for (metallic) Cu surfaces and is well reported in the published literature [29, 30, 41]. In contrast, the reaction mechanism over Cu_2O has been studied much less and is hence less well understood. The key – and so far unproven – assumption in the proposed mechanism is hence the lack of lattice O interaction in Cu_2O with CO, which results in the preference for CO over CO_2 selectivity that is particularly prevalent in environments featuring a high Cu oxidation state (Cu_2O) and low O_2 partial pressure (Figure 16D). In order to verify this assumption, DFT calculations were employed to evaluate the formation of CO_2 from surface CO and subsequent desorption of CO_2, as well as the direct desorption of surface CO, on the three low index planes [(100), (110), and (111)] of Cu_2O. The results of these calculations are shown in Figure 17. Since the facets present on the actual catalytic NPs are unknown, these three low index surfaces were selected, as testing every possible facet is computationally unfeasible and these low index planes are the most stable and hence typically most prevalent surface orientations. The energy barriers for the formation of CO_2 (E_a) and CO desorption (E_d) reactions were compared over the three surfaces, as well as the total energy differences between initial reactants and final products (ΔE). CO_2 is formed by CO bonding with a nearby lattice O atom, which was highlighted in Figure 17 in light red for clarity. The O-terminated (100) and (111) surfaces are covered with O atoms that have low coordination numbers, which make the O atoms behave like adsorbed O atoms, rather than lattice O. In addition, O-terminated surfaces indicate a high O_2 partial pressure scenario not representative of the previously mentioned environment in which CO desorption is selected over CO_2 formation [144]. Thus, Cu-terminated surfaces were chosen for (100) and (111) surfaces. The Cu-O terminated surface was used for the (110), as this termination contains lattice O in the uppermost layer. These terminations feature lattice O near the surface accessible to adsorbed CO species for CO_2 formation.

The most stable configurations for CO and CO_2 on Cu_2O surfaces were found by testing different orientations and adsorption sites (i.e. horizontal and vertical orientations and bonding via C or O). For the (100) surface, CO and CO_2 are found most stable on the Cu bridge sites. For the (110) and (111) surfaces, CO and CO_2 are found most stable on the Cu top sites. CO_2 was found to be weakly adsorbed on all three surfaces compared to CO. Adsorption configurations and energies can be accessed in the Supporting Information. CO_2 is adsorbed on the surface, with the single lattice O atom removed. CO desorption was simulated by placing the CO molecule far above the surface (over 4 Å above the surface).

Figure 17 summarizes the key results: For the (100) and (110) surfaces, the energy barriers for CO_2 formation (E_a) are higher than the CO desorption energies (E_d), indicating a preference for CO desorption. In contrast, for the (111) surface, the energy barrier for CO_2 formation is lower than the CO desorption energy. Differences between initial and final state energies (ΔE) of adsorbed CO oxidizing to CO_2 are negative for (100) and (110) surfaces (-0.61 and -0.73 eV, respectively), while the ΔE between adsorbed CO and desorbed CO are positive (1.21 and 0.27 eV). However, the ΔE between adsorbed CO and CO_2, and the ΔE between adsorbed vs. desorbed CO for the (111) surface are both positive (0.63 and 1.05 eV, respectively). Since the activation barrier for CO_2 decomposition on (111) is only 0.15 eV, CO desorption may be competitive with CO oxidation. The positive ΔE for CO oxidation on the (111) surface could be explained by the formation of an oxygen vacancy in the second layer. Compared to the (100) and (110) surfaces, the oxygen vacancy formation energy on (111) surface is 1.39 eV and 0.48 eV higher, respectively. This indicates that the oxygen vacancy causes the (111) surface to be more unstable after CO oxidation compared to oxygen vacancies for the (100) and (110) surfaces. Note that the CO desorption barriers (E_d) are the same as ΔE for CO desorption, since CO desorption is a non-activated step.

Theoretical results for the (100) and (110) surfaces support the key experimental observations of unidentifiable catalyst surface facets. Even on oxidized Cu surfaces, adsorbed CO prefers to desorb rather than interact with lattice O atoms to form CO_2 in low O_2 partial pressure environments, hence rendering CO_2 selectivity insensitive to the oxidation state of the catalyst.

3.5 CONCLUSION

The study in this chapter aimed to elucidate the reaction mechanism of methanol partial oxidation to H_2 and CO_2 on Cu catalysts. A specific focus was the dependence of reaction selectivity on the oxidation state of the catalyst. It was found that MeOH conversion and reaction selectivity to H_2 and CO_2 is strongly affected by the O_2/MeOH feed ratio and shows a strong dependence on time-on-stream while approaching steady state. Post-reaction analysis by XPS revealed that during this transient Cu^0 was gradually oxidized to Cu_2O and that the rate of this oxidation depends on the O_2 partial pressure in the gas phase. Crucially, H_2 selectivity depends strongly on the presence of metallic Cu, i.e. it increases with increasing concentration of Cu^0. On the other hand, CO_2 selectivity shows no dependence on Cu oxidation states and instead is controlled by the O_2 concentration in the gas phase. These observations were explained by a lack of interaction between adsorbed CO and lattice oxygen in Cu_2O, i.e. by the fact that CO_2 formation occurred exclusively through interaction with chemisorbed surface oxygen, as confirmed via DFT calculations. In contrast, H_2 can easily access lattice oxygen to form H_2O. It is worth to mention that possible reaction pathways on Cu/Cu_2O are just proposed to explain the experimental observation and providing necessary DFT calculation to the unproven assumption. The present study focused entirely the role of Cu oxidation states in partial oxidation of methanol. It is well known that in methanol synthesis the Cu-ZnO interface plays an important role as well. While ZnO remains oxidized under all conditions of the reported experiments is verified experimentally, it hence seems likely that the Cu-ZnO interface also affects reactivity in partial oxidation of methanol. However, this aspect was beyond the scope of the present studies and suggests that combination of in situ environmental TEM studies with reactivity studies as reported here will be helpful to shed further light on structure-activity correlations for Cu-ZnO catalysts in partial oxidation of methanol.

Overall, the study thus not only produced new insights into the POM mechanism on Cu-based catalysts, but along the way also suggests a rational procedure for optimizing catalyst selectivity in POM: A logical conclusion from this study is that maximizing selectivity toward H_2 and CO_2 requires maintaining Cu in a metallic state within the Cu/ZnO catalyst while at the same time maintaining a high oxygen partial pressure. Clearly, these are contradictory demands, as higher oxygen partial pressures will generally result in faster and deeper oxidation of the catalyst. This hence points towards a target for rational design of next-generation POM catalysts: It is well known that alloying metals can strongly affect their resistance to oxidation [146-149]**.** Hence, identifying components for alloying of Cu-based catalysts which help to suppress or minimize Cu oxidation may be a promising way to optimize Cu-based POM catalysts for future clean energy applications. First-principles calculations could be used further as a guide and screening tool in such an undertaking.

4.0 ACTIVE SITE OF CU_2O ISLAND UNDER METHNAOL REDUCTION

4.1 INTRODUCTION

Cu and copper oxides are applied in a wide range of applications especially in heterogeneous catalysis[72, 150-153]. The oxidation of Cu and reduction of Cu oxides (Cu_2O, CuO) as well as the formation of a metal/oxide interface play an important role in controlling reaction mechanisms of catalytic reactions. Phase transformations between Cu and Cu oxides under oxidizing or reducing conditions are usually found to alter the reactivity and selectivity of the reaction during many catalytic prcoesses such as methanol oxidation [62, 143, 150, 154], water-gas shift [155, 156], and methanol synthesis [153, 157, 158]. For example, Cu^0 can be oxidized to Cu^{1+} and Cu^{2+} during methanol oxidaiton or steam reforming. Previous investigators have suggested that Cu^0 is active for methanol oxidation to H_2 and CO_2, Cu^{1+} is active for H_2O and CO formation, and Cu^{2+} – as the least active species – only produces H_2O and CO_2 [33, 35, 62]. The first reaction step that these catalytic reactions share involves dissociative adsorption of methanol into methoxy speices (CH_3O) and H on Cu surfaces which still requires structual observation at atomic scale using in situ techniques. [92, 159, 160]

Previous experimental studies showed that methanol interacted weakly on clean Cu(100) [160], Cu(110) [159] and Cu(111) [92] surfaces. Yates et. al showed that pre-absorbed O are necessary to activate Cu surfaces for methanol adsorption and determining subsequential reaction pathways using Auger electron spectroscopy (AES) [92]. Sexton [160]used electron energy loss spectroscopy (EELS) to investigate the structure of methoxy on Cu(100) and concluded that the reaction was not sensitive to the crystal plane. Besides, the oxygen coverage on Cu surfaces also plays a key role in determining the reactivity and reaction pathway of methanol reforming reactions. There have been many theoretical studies on methanol oxidaiton on low-index Cu surfaces. Sakong et al. studied partial oxidaiton of methanol (POM) on clean and oxygen-covered Cu(100) and Cu(110) surfaces using density funtional theory (DFT) and kinetic Monte Carlo (kMC) [67, 70, 161, 162]. Methanol has been studied on Cu(111) with several isolated oxygen atoms or a chemisorbed O layer [69, 141, 163] using DFT. Both experimental measurements and theoretical calculations consistently suggested that decomposition of methanol on Cu is strongly promoted by the presence of surface oxygen. Under realistic methanol oxidation conditions, Cu is likely to be oxidized to Cu_2O, which make studies on Cu_2O another important step towards understanding these catalytic reactions [68, 69, 164, 165]. Previous studies found that Cu_2O(111) is more effective than Cu_2O(100) for methanol dehydrogenation because both CH-bond breaking and CO-scission are active on its surface that has co-existing of copper vacancies and oxygen [68, 165].

While these reactions have been studied in much detail in terms of active oxidation states on Cu with methanol using a range of spectroscopic techniques, such as photoelectron spectroscopy (XPS) [71, 92, 150], infrared reflection adsorption spectroscopy (IRRAS) [166-168], x-ray power diffraction (XRD) [150, 169, 170] and computational methods[151, 171, 172], the active structure of Cu and the microstructural evolution of the concomitant phase tranformations under methanol is little explored. Recent study on methanol synthesis showed that the active site of this system consists of Cu steps decorated with Zn atoms, and stablized by well-defined bulk defects using a combination appoach of XPS, TEM and theoretical modeling [72, 153, 157] However, understanding of the structural evolution of the Cu catalyst, especially at the atomic scale, is required to furhter attain a fundamental understanding of the processes and reaction mechnisms governing these transformations.

In situ Environmental Transmission Electron Microscopy (ETEM) has emerged in recent years as a powerful technique to bridge this gap. By introducing gas to the sample area, together with other external stimuli like heat, ETEM allows the study of atomic-scale structural evolution during gas-solid reactions, thus enabling new insights into reaction mechanisms and active sites of gas-solid reactions [73, 173-179]. During the past, people have employed in situ TEM techniques to study the nucleation, stability, kinetics, and morphology of Cu oxide islands formed during Cu oxidation under different temperatures, gas pressures, and substrate orientations [180-182]. However, for the interaction of Cu_2O with methanol, which has much broader applications especially in heterogeneous catalysis [68, 92, 93], there is no literature report on the microstructure evolutions so far.

Here, we use *in situ* ETEM to observe the reduction dynamics of Cu_2O on Cu(100) under methanol (MeOH) vapor. We find that the MeOH induced reduction of Cu_2O proceeds via a two-stage shrinking process of Cu_2O islands, characterized by a transition from anisotropic to isotropic shrinking. This transition is explained by the preferential adsorption and dissociation of MeOH along Cu_2O surface steps, a connection that is verified by Density Functional Theory (DFT). These investigations hence yield a new atomistic understanding of the active sites of Cu_2O during MeOH reforming reactions.

This chapter is structured as follows. Chapter 4.2 provides experimental preparation and video processing details. In the first two parts of Chapter 4.3, ETEM was used to grow Cu_2O nano-islands under controlled oxidation and reduce them under MeOH environment. Then the island dimension profile during reduction reaction was quantitatively measure. In Chapter 4.3.3, a uniform two-stage shrinking behavior from anisotropic to isotropic shrinking was identified statistically. And such observation was explained by the preferential adsorption of MeOH on $Cu_2O(100)$ step edges which was further verified using Density Functional Theories (DFT) in Chapter 4.4 followed by conclusions in Chapter 4.5.

4.2 EXPERIMENTAL SECTION

4.2.1 Sample Preparation

Multiple single-crystalline Cu(100) films used in this work were produced by *e*-beam evaporation of 99.999% pure Cu pellets on NaCl(100) substrates. The films were grown in a UHV evaporator system with an approximate base pressure of 1×10^{-9} Torr. The deposition rate was measured by quartz crystal thickness monitors and the NaCl substrate was heated by *e*-beam with a temperature stability of ±5 K. Prior to mounting the substrate into the evaporator, the single-crystalline NaCl(100) substrate was cleaved under ambient atmosphere along its (100) surface to get fresh, atomically flat (100) surfaces. Cu(100) thin films were epitaxially grown on the NaCl(100) substrate, with a deposition rate of 1.2 Å/s and a substrate temperature of 300 °C. Cu films with an average thickness of 60 nm were used in this study. After deposition, Cu films were cut into TEM sample sizes and then floated off from the NaCl substrate in deionized water (Milli-Q, 18.2M

Ω cm). Residual NaCl on the films was removed by transferring the films into fresh deionized water several times. Films were then floated onto sample supports, namely Cu TEM mesh grids purchased from Ted Pella.

4.2.2 *In situ* Oxidation and Reduction

A differentially pumped ETEM (Hitachi H-9500, LaB_6) operated at 300 keV, equipped with a double-tilt heating holder (Hitachi) and a homemade gas injection system with up to 3 lines of gas injection (NFCF, University of Pittsburgh) is used for this study. Real-time TEM videos and images were recorded by an Orius SC1000A camera at a frame rate of 5 frames/s.

Since Cu oxidizes when exposed in air, the *in situ* TEM experiment contains three steps: H_2 annealing, growing of Cu_2O nano-islands, and Cu_2O reduction under MeOH. First, the native oxide (Cu_2O) on Cu films was removed by applying H_2 at a partial pressure of 7.6×10^{-6} Torr to the oxidized film, while keeping the sample at 650 °C. The elevated temperature annealing also facilitates the formation of faceted holes – with (100) and (110) facets – on Cu films, which enables ensuing observation of Cu_2O nano-island reduction from the edge-on view. H_2 was then pumped out of the microscope. Second, Cu_2O nano-islands were grown under O_2 partial pressure $P_{O2}=1.5\times10^{-4}$ Torr and $T=350$ °C for ~5 min, which is a typical condition for Cu_2O nano-island growth [180, 183]. In order to observe the subsequent reduction of Cu_2O under MeOH, O_2 is pumped away and then MeOH vapor is introduced into the specimen chamber controlled by a needle valve. *In situ* TEM observation of Cu_2O reductive shrinking is carried out by imaging the overall Cu_2O nano-island geometry under MeOH vapor at 7.6×10^{-6} Torr and 250°C. To rule out any geometric change induced solely by *e*-beam, the Cu_2O nano-islands were observed under relatively low beam dosage; before MeOH injection, each island was illuminated under vacuum condition for 5 min. No significant geometric change of Cu_2O was captured during this period, which diminishes the possibility of *e*-beam effects impacting Cu_2O island shrinking. In comparison, all of reported Cu_2O nano-islands can be reduced completely by MeOH within 3 min.

4.2.3 Images and videos analysis

All TEM images are processed and edited using Gatan Micrograph and Fiji ImageJ. All useable frames of videos are aligned to compensate for thermal drift and were measured using Fiji ImageJ. To properly process the in situ videos which have a format of MP4. The “ffmpeg” plugin for Fiji-ImageJ is installed to analyze MP4 videos. The stabilization of videos is achieved through template matching function which is also available online as a plugin for Fiji-ImageJ.

The measurement of island dimension during one piece of video is achieved through reslicing the video under certain line of interest. The outcome will be a figure that plotting the contrast along line of interest versus time. By properly adjusting the tolerance of wand tool from imageJ, the boundary of contrast reflected from different subjects can be easily generated and transferred to XY coordinates (Pixel location and frame) through Fiji-ImageJ, which can be further converted to distance of measurement versus video time.

4.3 RESULTS

4.3.1 Cu_2O nano-islands on Cu(100) facets

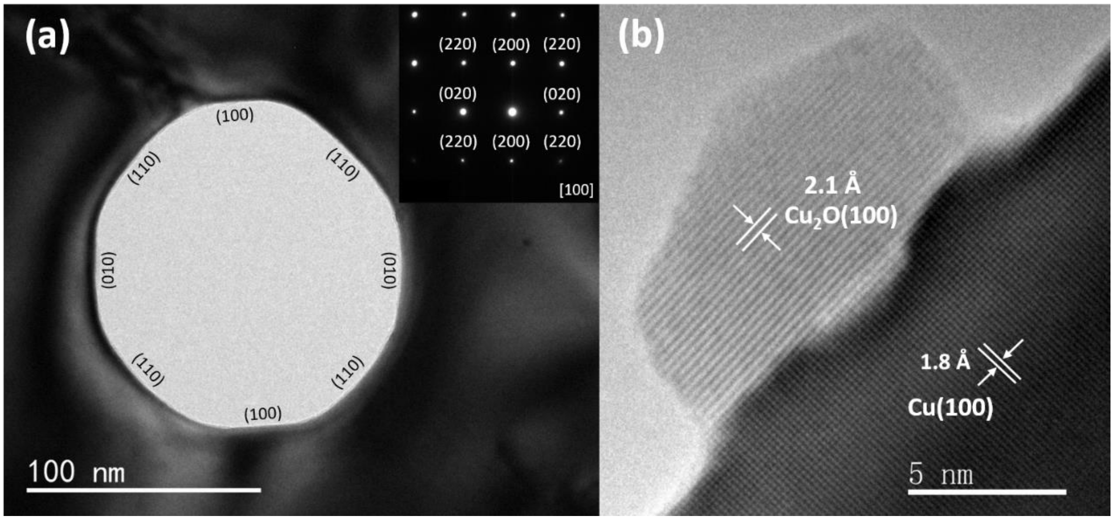

Figure 18. In situ formation of Cu_2O nano-island. (a) Bright-field TEM image of an as-prepared faceted hole on Cu(100) film after annealing at 600 °C and 7.6×10^{-6} Torr H_2; the inset shows the corresponding diffraction pattern. (b) HRTEM image of a Cu_2O nano-island on Cu(100) facet formed at 350 °C and 1.5×10^{-4} Torr for 5 min.

Figure 18(a) shows a faceted hole with well-defined (100) and (110) facets after annealing under 7.6×10^{-6} Torr H_2 at 600 °C. These freshly created facets are atomically clean and well-suited for growth of Cu_2O under O_2. Figure 18(b) shows a typical High Resolution TEM (HRTEM) image of a Cu_2O nano-island on a Cu(100) facet generated under 1.5×10^{-4} Torr O_2 at 350 °C. The Cu_2O phase is confirmed by measuring the periodic lattice spacing, which has an epitaxial relationship of $Cu_2O(100)//Cu(100)$. This Cu_2O island generally has a trapezoidal shape, with a top facet of $Cu_2O(100)$ and higher indexed side facets.

4.3.2 *In situ* reduction of Cu_2O under MeOH

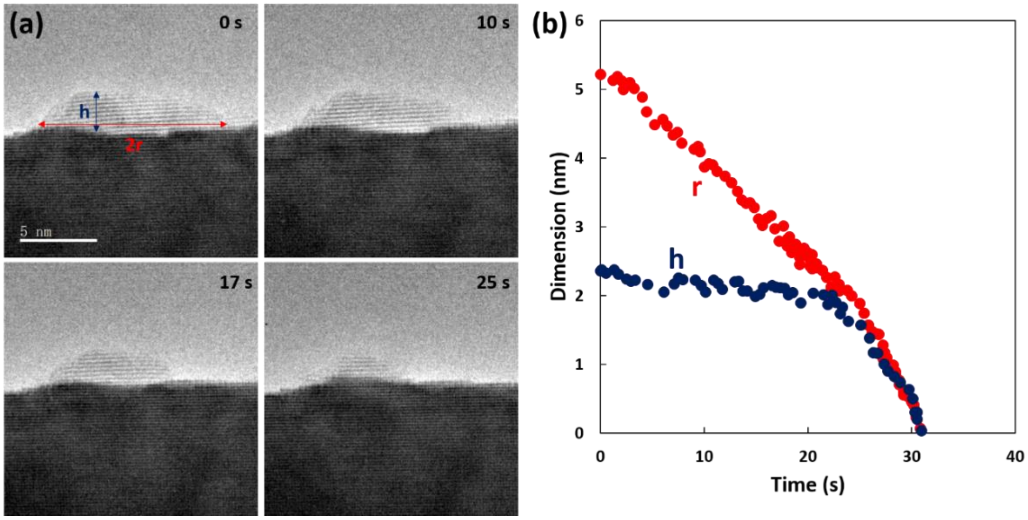

Figure 19. Reduction process of Cu_2O nano-island on Cu(100) facets under 7.6×10^{-6} Torr MeOH vapor and at 250°C. (a) HRTEM images depicting Cu_2O nano-island shrinking over time. (b) Time-dependent change of the radius (r) (half width) and height (h) of the Cu_2O nano-island during reduction.

The Cu_2O nano-islands formed from *in situ* oxidation are ideal for studying oxide dynamics during reduction by MeOH. Figure 19 shows a time-sequence of TEM images depicting the Cu_2O island during a reductive shrinking process under MeOH vapor (7.6×10^{-6} Torr MeOH and 250°C; fig. 19a) along with the dimensional change (radius and height) of the Cu_2O island during reduction (fig. 19b). The Cu_2O nano-island is located on the Cu(100) facet with an initial height of 2.3 nm and radius (half of the width) of 5.2 nm. During the first 20 s of reduction, Cu_2O island structural dynamics demonstrate a pronounced anisotropic shrinking, in which the island radius strongly decreases from 5.2 to 2.3 nm while the island height remains virtually constant (minor decrease from 2.3 nm to ~2 nm). When the measured island radius roughly matches its height of 2 nm (at t= 23 s), island shrinking suddenly switches from anisotropic to isotropic, as both island height and radius decrease with similar rates until the whole island is removed at around t= 31 s.

4.3.3 Identification of two-stage shrinking

To further confirm this two-stage shrinking behavior, i.e. the transition from anisotropy to isotropy, careful statistical analysis of the data was conducted before fitting the change of island radius and height in two parts. (Details of the statitistical data analysis is given in the supplemental information). As Figure 20b and Table 1 demonstrate, both island radius and height can be fitted into linear and parabolic parts using piecewise fitting. The linear radial shrinking rate (0.14 nm/s) is an order of magnitude larger than that of island height (0.017 nm/s), indicating the anisotropic shrinking of the island. In the parabolic regime, the radial shrinking rate (0.015 nm^2/s) is close to that of height (0.011 nm^2/s), confirming isotropic shrinking. The transition dimensions between anisotropic and isotropic shrinking for radius and height are determined to be 2.2 and 2.1 nm, respectively.

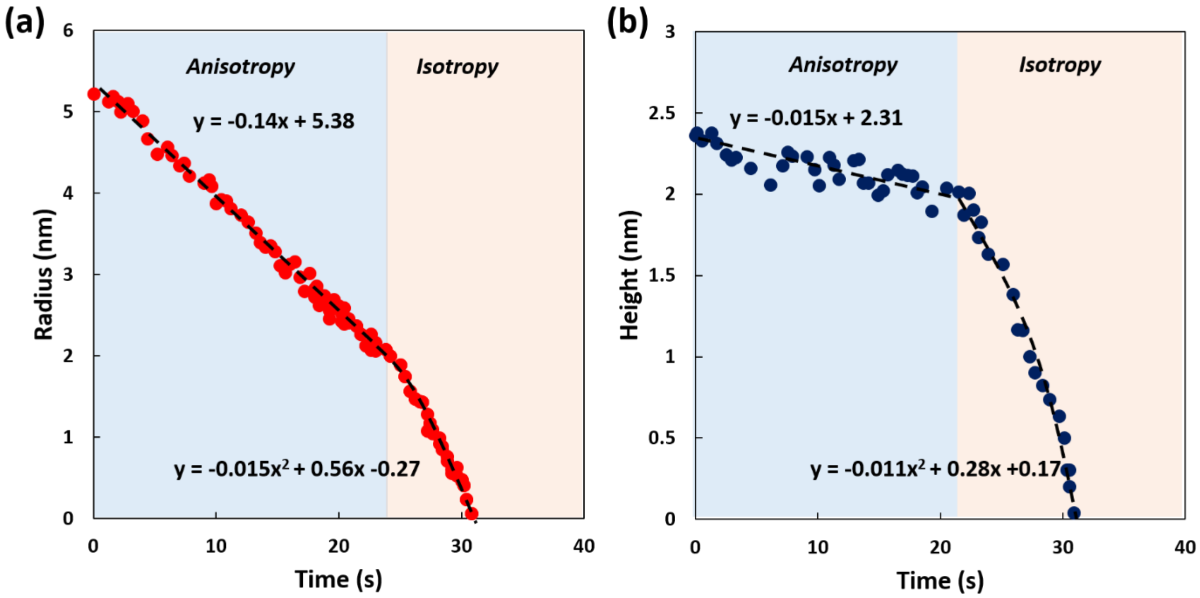

Figure 20. The time dependence of Cu_2O island radius (red) and height (yellow) during reduction. The dashed lines correspond to linear fitting for anisotropic shrinking and parabolic fitting for isotropic shrinking.

Similar analysis was adapted for six additional Cu_2O islands and found that their shrinking profiles (radius and height) can be best fitted with two regimes describing linear and parabolic shrinking (Figure 22, Table 1) [184]. Fitting parameters and determined transition dimensions for each island were summarized the results in Table 1. By comparing the linear shrinking rates of radius and height, all island radii have significantly higher decreasing rates than heights, while decreasing rates of height are all close to zero or slightly above. However, decreasing rates of radius and height are comparable in value during parabolic shrinking. The described observation can be observed more directly from Figure 21, in which radius and height shrinking rate ratios are compared in a logarithmic scale for both linear and parabolic shrinking regimes. Ratios for the linear regime (blue) are all significantly higher than ratios for the parabolic regime (orange), emphasizing the two-stage shrinking from anisotropy to isotropy. The isotropic shrinking region is highlighted in purple and defined by observed radius and height shrinking rate ratios between 0.25 and 4. Moreover, the radii at transition points (between linear and parabolic shrinking) of all islands are around or below 2 nm, regardless of their initial sizes (Figure 23). The fact that shrinking rates during isotropic shrinking are generally faster than those during anisotropic shrinking indicate that all islands start collapsing when their radii drop to 2 nm or below (Figure 22).

Table 1. Fitted island shrinking rate (linear and parabolic) for radius and height, with transition island dimensions between both shrinking regimes.

Island #	Linear Shrinking Rate (nm/s × 10^3)		Parabolic Shrinking Rate (nm^2/s × 10^3)		Initial Dimension (nm)		Transition Dimension (nm)	
	r	h	r	h	r	h	r	h
1	-22.3±0.22	-0.420±0.41	-6.23±0.61	-2.73±0.37	2.94	1.40	1.72±0.02	1.30±0.06
2	-12.2±0.10	-2.19±0.14	-0.450±0.02	-1.14±0.02	2.35	1.92	1.67±0.21	1.54±0.22
3	-31.3±1.21	-0.910±0.66	-7.01±2.63	-4.81±0.24	2.62	1.61	1.73±0.12	1.43±0.12
4	-24.7±1.25	-0.230±0.19	-0.680±0.03	-0.270±0.05	2.41	1.88	1.70±0.12	1.81±0.04
5	-235±2.97	-39.2±2.89	-8.86±4.44	-8.95±3.37	5.49	1.97	1.63±0.03	1.36±0.21
6	-144±1.80	-0.680±0.54	-1.55±0.82	-1.28±0.20	4.66	2.14	1.83±0.11	2.08±0.05
7	-142±1.55	-14.7±1.94	-15.3±1.85	-9.10±2.36	5.22	2.36	2.18±0.07	2.06±0.08

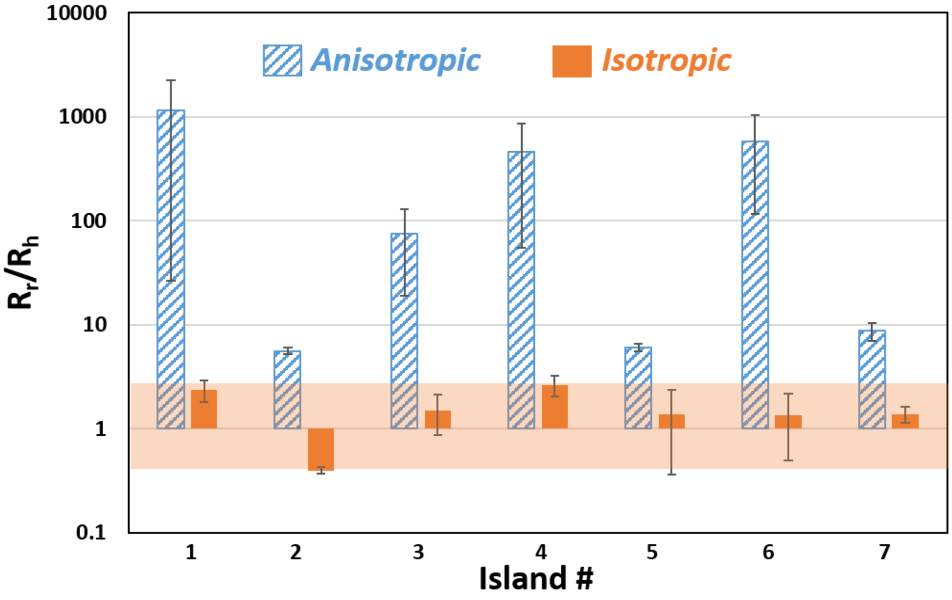

Figure 21. Ratio (radius/height) of shrinking rate for linear (orange) and parabolic shrinking (blue with stripes). The region defined by isotropic shrinking is highlighted in purple. The isotropic shrinking region is highlighted in light orange and defined by observed radius and height shrinking rate ratios between 0.25 and 4.

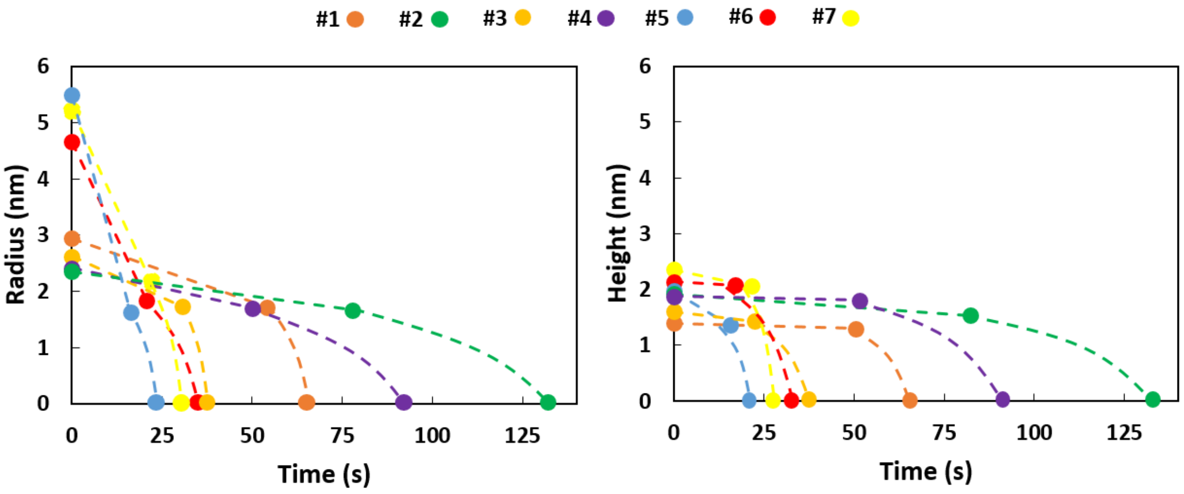

Figure 22. Radius and height magnitudes of all Cu_2O islands at starting, transition (between linear and parabolic shrinking) and end points during island shrinking.

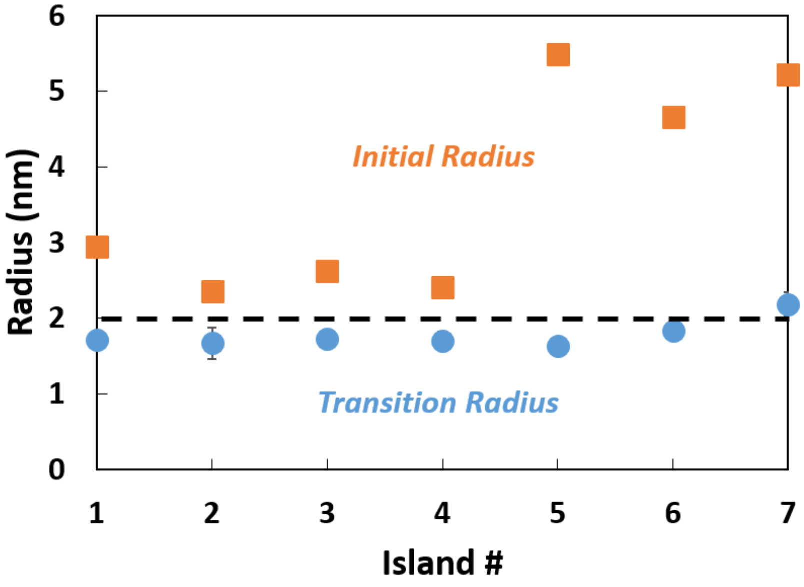

Figure 23. The radii of Cu_2O islands at initial (orange squares) and transition stages (blue circles).

4.4 DISCUSSION

Past literature has shown that the shape transition of Cu_2O islands under oxidative conditions was controlled by the energetic balance between surface and interface energies, as well as elastic stress relaxation [185, 186]. Besides thermodynamics, kinetics also plays an important role in determining metal oxide morphology during gas reactions [181, 183, 185, 187]. Cu_2O island shrinking under vacuum annealing has been shown to follow linear decay behavior, while a kinetic model based on the dissociation along the island perimeter was developed [183].

The reduction of Cu_2O under dissociative adsorption of MeOH can be described by $Cu_2O + 2CH_3OH \rightarrow 2Cu + 2CH_3O + H_2O$, yielding Cu atoms that diffuse back to Cu substrate and water molecules that desorb from the surface [188]. Our results suggest that the structural dynamics of Cu_2O islands on Cu(100) under MeOH are controlled by the molecular interaction between MeOH and different Cu_2O structures. Previous experimental and theoretical studies suggest that MeOH binds more strongly to Cu_2O than Cu surfaces, and that they prefer to adsorb and react with lower-coordinated Cu and O atoms [68, 70, 161, 188]. The top surface of an epitaxial Cu_2O island has a well-defined (100) orientation; hence, O atoms on top surfaces are highly coordinated. However, island side facets are made of numerous single or multilayer atomic steps in the (100) direction, which are comprised of different combinations of Cu and O atoms that depend on surface termination. Hence, O atoms on these step edges are generally less coordinated than those at top facets. As a result, we hypothesized that MeOH would most likely adsorb and react at the side steps of an island, causing the anisotropic shrinking that is seen in our experimental observations.

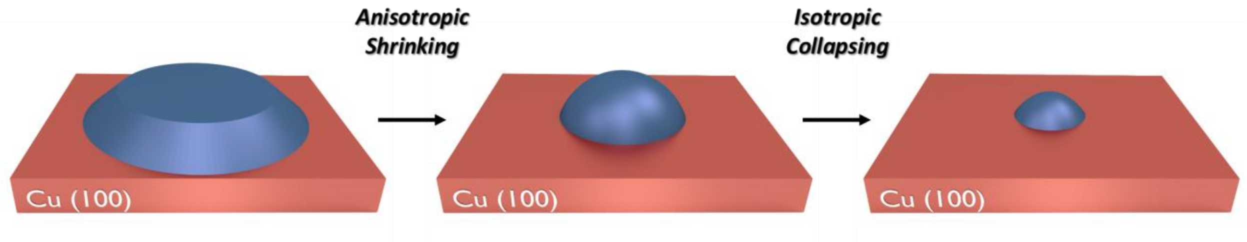

Figure 24. Simple schematic demonstration of two-stage shrinking of Cu_2O under MeOH.

When islands have similar radii and heights (below 2 nm), Cu_2O islands generally have a semi-spherical shape, in which there is no well-defined top surface. For such small nano-islands, radius magnitude equals approximately only four Cu_2O unit cell lengths. At the atomic level, interfacial Cu and O atoms should hence all become undercoordinated, regardless of placement on top or side facets. We hence expect that MeOH molecules will favorably absorb and react with Cu and O atoms on all island surfaces proportionally, resulting in the observed isotropic shrinking. Our proposed shrinking mechanism also qualitatively explains the linear and parabolic shrinking rates we observed in island dimension profiles. During the anisotropic shrinking, MeOH molecules preferentially adsorb and react on Cu_2O side facets, which, for constant island height, scale directly with the island radius ($A_{sf} = 2 \pi r h$, where A_{sf} is the area of the side facet, and r and h are the island radius and height, respectively). In contrast, during isotropic shrinking, reactions take place on the entire island surface (A_T), which scales parabolically with the island radius ($A_T = n \pi r^2$, where n is a constant determined by the overall island shape and volume).

In order to further verify our hypothesis, we employed DFT calculations to compare the dissociative adsorption processes of MeOH molecules on $Cu_2O(100)$ flat surfaces and $Cu_2O(100)$ atomic steps. This is accomplished by comparing the adsorption and dissociation barrier energies [189, 190] of flat and stepped interfaces using three-step models, as is shown in past work on Cu-containing surfaces [191-193]. All adsorption energies (E_{ads}) for systems with adsorbates are set relative to the energies of corresponding surfaces without adsorbates. MeOH dissociation barriers (E_{diff}) to CH_3CO (MeO) and H adsorbate formation are set relative to undissociated MeOH E_{ads}, and are calculated using the Climbing Image Nudged Elastic Band (CI-NEB) method [194, 195]. A linear response derived Hubbard U of 9.3 eV is applied to Cu 3*d* orbitals based on previously developed techniques when evaluating the sensitivity of results to electronic correlation correction [128, 129]. Further information on all DFT results used to validate the anisotropic relationship observed in previous experiments can be found in the Appendix D, which contains selected candidates for tested adsorption sites generally based on past work [68, 165].

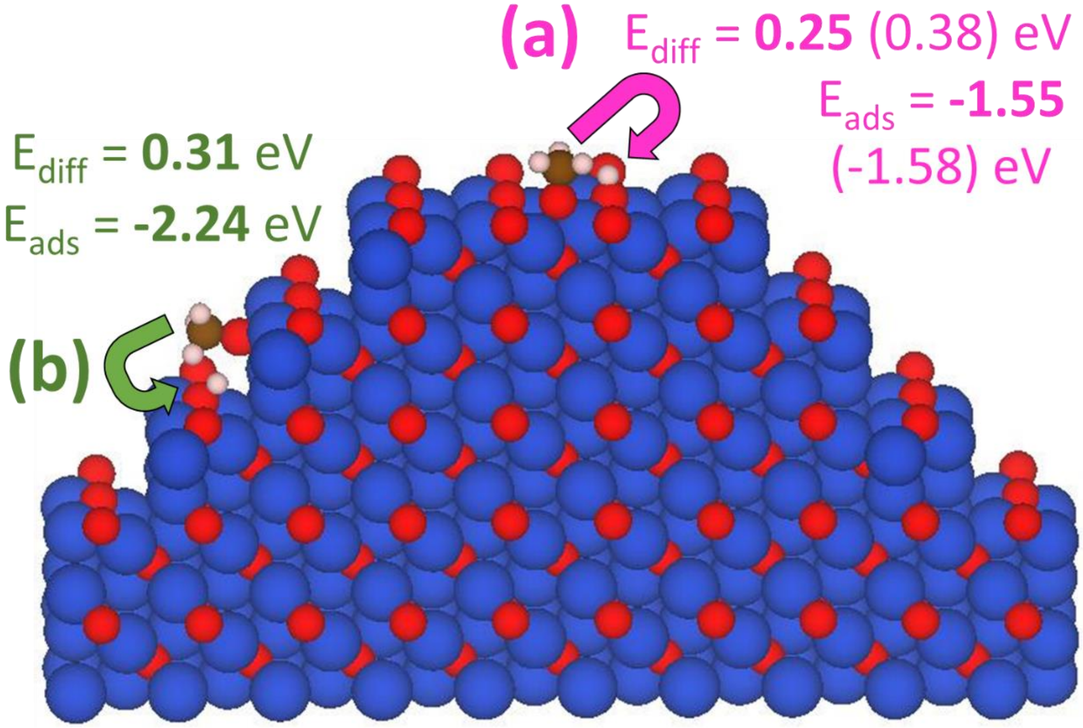

Figure 25. DFT calculated adsorption (E_{ads}) and dissociation barrier (E_{diff}) energies of methanol (a) for flat $Cu_2O(100)$ (pink) and (b) stepped $Cu_2O(100)\{100\}$ (green) candidate systems, considering the effects of Hubbard U inclusion for (a) in parenthesis. Cu, O, C, and H atoms are colored blue, red, brown, and white, respectively.

Figure 25 shows the most favorable, O-terminated flat $Cu_2O(100)$ (Figure 25a) and the stepped $Cu_2O(100)\{100\}$ (Figure 25b) interfaces used to validate experimental anisotropic shrinking. Simulation of these dissociated MeO and H adsorbate systems, in addition to the reaction processes needed to achieve them starting from corresponding systems without adsorbates, was completed using separate structures. E_{ads} and E_{diff} for flat $Cu_2O(100)$ surfaces that either consider (bold) or omit (parentheses) Hubbard U agree within 0.13 eV or less, while the E_{diff} of the most favorable stepped $Cu_2O(100)\{100\}$ and flat surface systems not considering electronic correlation agree within 0.06 eV. These differences are small compared to the difference (0.69 eV) between MeOH E_{ads} on the most favorable flat (-1.55 eV) and stepped (-2.24 eV) $Cu_2O(100)$ surfaces. As shown in Appendix D, these most favorable structures were resolved by testing different relative MeO and H adsorbate site configurations on Cu and O terminated interfaces. Ultimately, this evaluation of candidate structures found that the most favorable flat surface featured H adsorbing to nearest neighbor O on O terminated $Cu_2O(100)$, while H and MeO adsorbing to adjacent O terminated steps form the most favorable $Cu_2O(100)\{100\}$ surface. The relative energetic favorability of MeO and H adsorption on stepped $Cu_2O(100)$ structures indicates an initial selective reaction of MeOH with Cu_2O island side facets, supporting the observation of anisotropic island shrinking. The energetic favorability of MeOH adsorbing on Cu_2O steps around island substrate perimeters (Cu_2O//Cu interface) may be slightly different than that on isolated Cu_2O surface steps. However, this energetic difference is expected to be significantly smaller than that between MeOH adsorption energies on flat $Cu_2O(100)$ surfaces and $Cu_2O(100)$ steps, since O atom coordination on steps is generally less than that on flat facets [164, 174].

4.5 SUMMARY AND CONCLUSIONS

The present study employed *in situ* ETEM to capture the structural evolution of Cu_2O nano-islands on Cu(100) during reduction with methanol. By careful statistical analysis of island dimension profiles during reduction, we observed a two-stage reductive shrinking behavior, starting from anisotropic shrinking, in which the island radius shrinks much faster than the island height, to isotropic shrinking, in which island radius and height shrink at a comparable rate. To our knowledge, this is the first time that a careful quantitative statistical analysis was used to identify and justify the presence of such different kinetic regimes. We then proposed that the preferential dissociative adsorption of methanol molecules on Cu_2O(100) atomic steps compared to flat terraces led to the dominantly observed anisotropic shrinking from island side facets, which was further verified by DFT calculations. This explanation is furthermore consistent with the fact that the anisotropic regime can be described with a linear rate law for the radius while the isotropic regime shows a parabolic behavior.

Overall, our study produced new atomistic insights on the active sites of Cu_2O nano-islands on Cu(100) during reductive shrinking under methanol. Our results suggest that stepped surfaces on small Cu_2O nanoparticles (radius<2 nm) significantly enhance the rates of methanol reformation on such nanoparticles, yielding a clear target for rational design of optimized nanocatalysts for this reaction. Furthermore, our work demonstrated that the combination of *in situ* ETEM experiments with DFT computational studies is a powerful approach towards gaining fundamental insights into important catalytic reactions. Given the increasing access to this high-end instrumentation, our understanding of heterogeneous catalysis and related gas-solid phenomena is poised to make significant advances over the near future.

5.0 DYNAMICS OF CU_2O ISLAND AND INTERFACE TRANSFORMATION UNDER METHANOL REDUCTION

5.1 INTRODUCTION

Cu-based material is very good option for making heterogeneous catalysis due to its active nature and inexpensive cost [72, 158, 196]. The oxidation of Cu to CuO_x under oxidzing condition and the reduction of CuOx to Cu under reducing condition are very important processes during a wide range of catalystic reactions that mainly contain solid-gas reactions [30, 150, 183, 197]. Specifically, redox processes of Cu-based catalysts are found to be able to alter the reactivity for reactions such as partial oxidaiton of methnaol, methanol synthesis and water-gas shift [32, 150-152]. Additionally, reduction of Cu oxides under methanol (MeOH) is also applied in the pretreatment or regeneration of a catalyst [73, 151, 152]. Although Cu-based catalytic reactions have been studied in much detail in terms of active phases of Cu using both experimental and theoretical methods [67, 71, 92, 150, 169-171, 198], observing atomic scale transformations among different Cu phases under real catalytic conditions is still necessary to gain a fundamental knowledge on active sites of reactions and underlying reaction mechnisms.

Thanks to the recent development of in situ transimission electron microscopy (TEM). We are now able to observe atomic-level structual evolutions of nanomaterials under heat and gas enviroments which are trying to mimic real reaction conditions [73, 173, 174]. For example, Topsøe et.al showed supported Cu nanoparticles undergo dynamic reversible shape changes in response to change of gaseous environment using in situ TEM [199]. So far, in situ TEM has been used to study many fundamental solid-gas reactions such as oxidation and reduction. Nickel oxide reduction in H_2 has been studied using in situ TEM in the past few years because of its importance in heterogeneous catalysis [200]. Jeangros et.al observed that the growth of Ni crystallites and the movement of interfaces result in the formation of pores whin the NiO grains to accommodate the volume shrinkage associated with the reduction [201]. Crozier et. al found that the NiO reduction mechanism under CH_4 involved diffusion of Ni cations along grain boudnaries and extended defects, and syngas formation only takes place during the later stages of NiO reduction, when Ni metal nanoparticles have broken through the NiO shell [202]. Recently, study on redox reactions between different Fe oxides using in situ TEM elucidated the atmomistic mechanism for the formation of hybrid structures of Fe oxides [175, 176, 203]. During the past, people have also employed in situ TEM techniques to study the nucleation, stability, kinetics, and morphology of Cu oxide islands formed during Cu oxidation under different temperatures, gas pressures, and substrate orientations [180-182]. However, few studies focused on atomic level observation of reduction of Cu oxides. Under vacuum annealing condition, the decomposition of Cu_2O islands back to Cu was reported to proceed along Cu_2O island perimeters, rather than the surface of Cu_2O island or interface between Cu_2O and Cu substrate[181]. A recent *in situ* TEM study done by Zhou et. al demonstrated that the reduction dynamics of Cu_2O islands under H_2 is governed a layer-by-layer transformation from Cu_2O to Cu occurring at the Cu_2O//Cu(100) interface [174]. However, for the reduction of Cu_2O under methanol, which has much broader applications especially in heterogeneous catalysis [68, 92, 93]. The limited amount of *in situ* work on Cu_2O reduction emphasizes the ambiguity of atomic-level Cu_2O reduction, especially under different reducing environments, and hence requires further study to more comprehensively understand.

In the present work, we use enviromental TEM to investigate the structural dynamics of Cu_2O nano-island and its interfaces with Cu(110) substrate which is different from the Cu(100) substrate that we investigated from our previous work [204] in order to show the impact of changing Cu_2O/Cu interface on the reaction under similar conditions. Besides, we will focus on the atomic level dynamic under real time reduction by MeOH inside the microscope in this work. The Cu_2O/Cu(110) serves as a model system for us to undertand the stability of Cu_2O nano-island and its interface, as well as crystalography dependent reactivity under MeOH reducing environment. We find that the MeOH-induced Cu_2O reduction results in monolayer by monolayer shrinking on side layers of Cu_2O nano-island which is caused by preferencial adsorption of MeOH on island perimeter sites that is verified by Density Functional Theory (DFT). This study demonstrates the importance of Cu_2O/Cu internface in determining active sites of Cu_2O at atomic level during MeOH reforming reactions.

This chapter proceeds in the following sequence. Chapter 5.2 describes sample preparation, in situ oxidation and reduction procedures. Chapter 5.3 demonstrates the high-resolution results collected from ETEM and frame-by-frame analysis.

5.2 EXPERIMENTAL SECTION

5.2.1 Sample Preparation

Single-crystalline Cu(100) films used in this work were produced by *e*-beam evaporation of 99.999% pure Cu pellets to NaCl(100) substrates. The films were grown in a UHV evaporator system with an approximate base pressure of 1×10^{-9} Torr. The deposition rate was measured by quartz crystal thickness monitors and the NaCl substrate was heated by *e*-beam with a temperature stability of ±5 K. Prior to mounting the substrate into the evaporator, the single-crystalline NaCl(100) substrate was cleaved along its (100) surface. Cu(100) thin films were epitaxially grown on the NaCl(100) substrate, with a deposition rate of 1.2 Å/s and a substrate temperature of 300 °C. Cu films with an average thickness of 60 nm were used in this study. After deposition, Cu films were cut into TEM sample sizes and then floated off from the NaCl substrate in deionized water (Milli-Q, 18.2MΩ cm). Residual NaCl on the films was removed by transferring the films into fresh deionized water several times. Films were then floated onto Cu TEM mesh grids purchased from Ted Pella.

5.2.2 In situ Oxidation and Reduction

Same ETEM and operation conditions as stated in Chapter 4.0 was used in this chapter. Since Cu is easy to oxidize when exposed in air, such as during sample preparation and transfer, and the morphology of these native oxides is not suitable for this study, the *in situ* TEM experiment contains three steps: H_2 annealing, growing of Cu_2O nano-islands, and Cu_2O reduction under

MeOH. First, the native oxide (Cu_2O) on Cu films was removed by applying H_2 at a partial pressure of 7.6×10^{-6} Torr to the oxidized film, while keeping the sample at 650 °C. The elevated temperature annealing also facilitates the formation of faceted holes – with (100) and (110) facets – on Cu films, which enables ensuing observation of Cu_2O nano-island reduction from the edge-on view. H_2 was then pumped out of the microscope. Second, Cu_2O nano-islands were grown under O_2 partial pressure P_{O2}=1.5×10^{-4} Torr and T=350 °C for ~5 min, which is a typical condition for Cu_2O nano-island growth [180, 183].

In order to observe the subsequent reduction of Cu_2O under MeOH, O_2 is pumped away and then MeOH vapor is introduced into the specimen chamber controlled by a needle valve. *In situ* TEM observation of Cu_2O reductive shrinking is carried out by imaging the overall Cu_2O nano-island geometry under MeOH vapor at 7.6×10^{-6} Torr and 250°C. To rule out any geometric change induced solely by *e*-beam, the Cu_2O nano-islands were observed under relatively low beam dosage; before MeOH injection, each island was illuminated under vacuum condition for 5 min. No significant geometric change of Cu_2O was captured during this period, which diminishes the possibility of *e*-beam effects impacting Cu_2O island shrinking. In comparison, all of reported Cu_2O nano-islands can be reduced completely by MeOH within 3 min.

5.2.3 Images and videos analysis

All TEM images are processed using Gatan Micrograph and Fiji ImageJ. All useable frames of videos are aligned to compensate for thermal drift and were measured using Fiji ImageJ. To properly process the in situ videos which have a format of MP4, he “ffmpeg” plugin was installed for Fiji-ImageJ to analyze MP4 videos. The stabilization of videos is achieved through template matching function which is also available online as a plugin for Fiji-ImageJ.

The measurement of island dimension during one piece of video is achieved through reslicing the video under certain line of interest. The outcome will be a figure that plots the contrast along line of interest versus time. By properly adjusting the tolerance of the wand tool from imageJ, the boundary of contrast reflected from different subjects can be easily generated and transferred to XY coordinates (Pixel location and frame) through Fiji-ImageJ, which can be further converted to distances of measurement versus video time.

5.3 RESULTS

5.3.1 Cu_2O nano-islands on Cu(110)

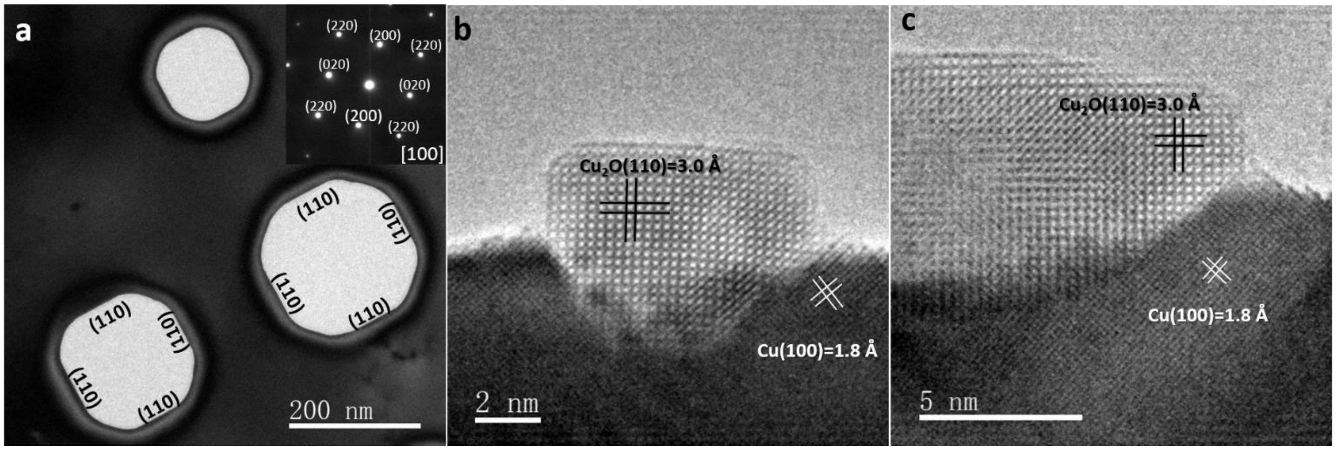

Figure 26. In situ formation of Cu_2O nano-island. a Bright-field TEM image of an as-prepared faceted hole on Cu(100) film after annealing at 600 °C and 7.6×10^{-6} Torr H_2; the inset shows the corresponding diffraction pattern. b, c HRTEM images of a Cu_2O nano-island on Cu(110) facet formed at 350 °C and 1.5×10^{-4} Torr for 5 min.

Figure 26(a) shows multiple faceted holes with well-defined (110) and (100) facets identified using a diffraction pattern, after being annealed under 7.6×10^{-6} Torr H_2 at 600 °C. These facets are atomically clean and flat, providing an ideal substrate for substantial growth of Cu_2O nano-islands under controlled oxidation. Figure 26(b) and Figure 26(c) show high-resolution TEM (HRTEM) images of a Cu_2O nano-island on Cu(110) facets generated under 1.5×10^{-4} Torr O_2 at 350 °C. The epitaxial relationship between the Cu_2O nano-island and its Cu(110) substrate is confirmed by measuring the periodic lattice spacing of the image. Figure 26(b) shows a Cu_2O island that has a rectangular shape, with a well-defined Cu_2O(110) surface on its top and side facets. The Cu_2O nano-island also has a large part at its bottom that is buried into Cu(110) substrate. The buried Cu_2O island has inverted trapezoid shape. Figure 26(c) demonstrates another Cu_2O island that has similar geometry as a comparison for *in situ* experiments. The island’s right side contains Cu_2O(110) surface on its top and side facets. It also has its bottom part buried into Cu(110) substrate.

5.3.2 In situ reduction of Cu_2O under MeOH

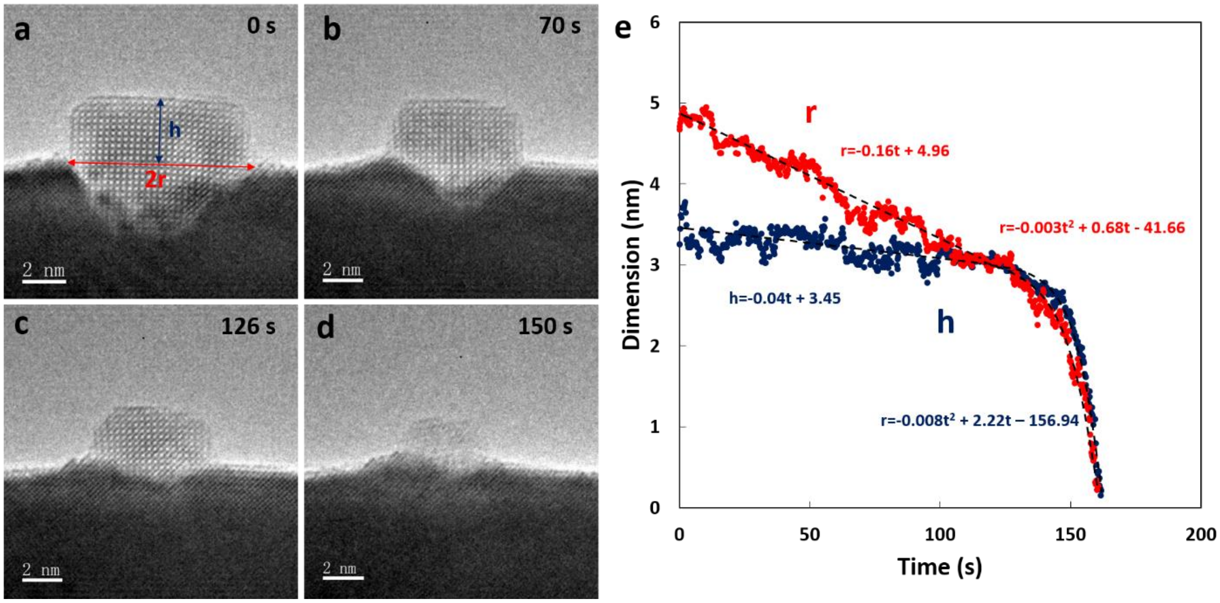

Figure 27. Reduction process of Cu_2O nano-island on Cu(110) facets under 7.6×10^{-6} Torr MeOH vapor and at 300°C. a-d HRTEM images depicting Cu_2O nano-island shrinking over time. e Time-dependent change of the radius (half width) and height of the Cu_2O nano-island (marked in a) during reduction.

The Cu_2O nano-islands could be formed during controlled *in situ* oxidation under 350 °C and 1.5×10^{-4} Torr of O_2 for 5 min. These islands are ideal for studying oxide dynamics under MeOH reduction. Figure 27a-d shows time-sequence TEM images of the Cu_2O island during a reductive shrinking process under MeOH vapor. As can be seen, the Cu_2O island can maintain its rectangular shape during reductive shrinkage until its tilting at 148 s as shown in Figure 27d. To further reveal the structural evolution of the island during reduction, the dimension change (radius and height) of the Cu_2O island (marked in Figure 27a) during the entire reduction is measured as shown in Figure 27e. This profile can be further fitted into a linear and a parabolic part based on AIC comparisons [184]. As shown from Figure 27e, the Cu_2O nano-island is initially located on the Cu(110) facet with a maximum height of 3.5 nm and radius (half of the width) of 4.8 nm. During the first 120 s of reduction, Cu_2O island structural dynamics demonstrate a unique anisotropic shrinking similar to what was observed in previous work, in which island radius gradually decreases from 4.8 to 3.1 nm. However, island height barely changes during this period by maintaining its height at around 3.2 nm during the initial 130 s. The anisotropic shrinking can be confirmed quantitatively when comparing the fitting parameters. The linear shrinking rate (0.016 nm/s) for radius is about 4 times larger than that for height (0.004 nm/s).

When the measured island radius roughly matches its height of 3 nm at around 130 s, island shrinking switches from anisotropic to isotropic, as both island radius and height begin simultaneously decreasing with comparable rates (0.003 and 0.008 nm^2/s, respectively) that are both faster than the initial anisotropic shrinking rate. The transition time between anisotropic and isotropic shrinking is determined to be about 125 s which is around the time when the buried part of Cu_2O almost gets reduced as can be seen from Figure 27c. The reducing reaction now has no additional source of lattice O to react, leading to the removal of lattice oxygens at the bottom layer of the Cu_2O nano-island and causing the island height to start deceasing. The island after this point starts shrinking in both directions (horizontal and vertical), leading to the observed parabolic shrinking profile. Moreover, there is a Cu pile forming at the bottom leftward perimeter of the island. This is probably due to the accumulation of freshly reduced Cu from side layers. At around 148 s, the Cu_2O nano-island radius and height have decreased down to a bit over 2 nm, and Cu pile at the bottom perimeter have grown bigger, destabilizing the entire Cu_2O nano-island and causing the island to tilt towards its left side (Figure 27d). Followed by the island tilting, both island dimensions start decreasing drastically and the entire island is removed within 10 s as is shown in Figure 27e. On the other hand, the buried Cu_2O bottom shows a different reductive shrinking dynamic. As shown in Figure 28, the buried part has an initial radius of 4.5 nm and height of 3.8 nm. By fitting the change of island radius and height into a linear and a parabolic part using piecewise fitting based on AIC [184], it can be seen that both radius and height of buried Cu_2O nano-island gradually decreases at comparable rate until the entire buried bottom part is reduced at around 135 s. The geometry of the buried Cu_2O has initially maintained the trapezoid shape until the bottom side shrinks to almost a point at around 70 s. After that, the buried Cu_2O has been able to maintain a triangle shape as shown in Figure 28b until its total removal at around 136 s. This could be attributed to the faster phase transformation from $Cu_2O \rightarrow Cu$ along Cu_2O//Cu(100) interface which essentially make of the two sides of the buried Cu_2O island shrink faster than the Cu_2O//Cu(110) interface which is the orientation of top and bottom surfaces of the trapezoid island.

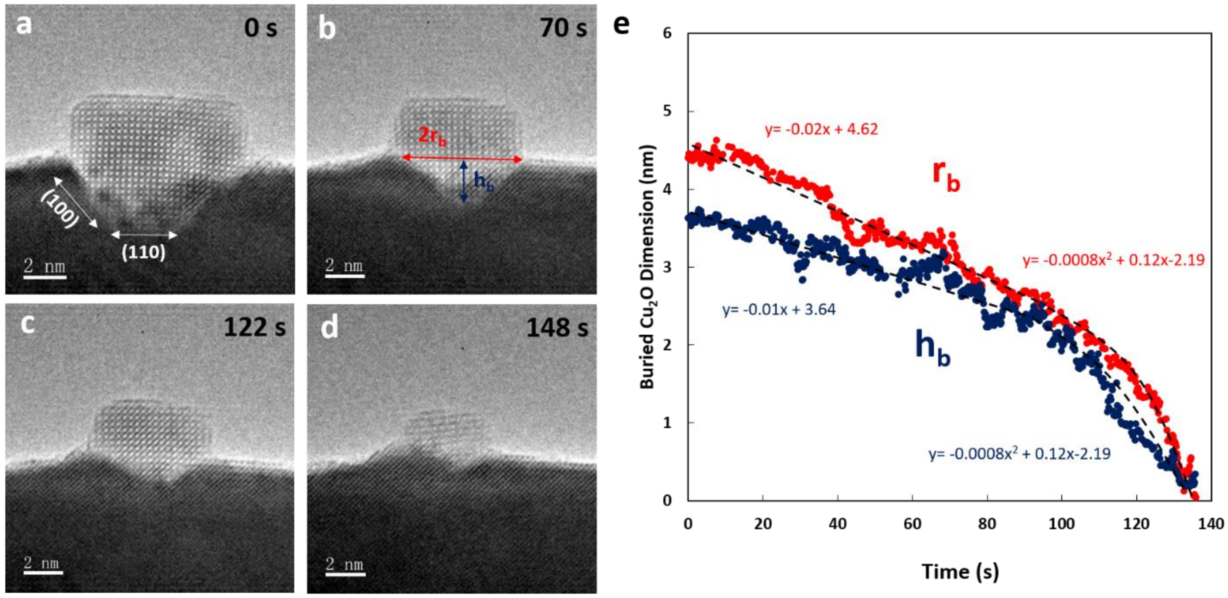

Figure 28. Reduction process of buried part of Cu_2O nano-island on Cu(110) facets under 7.6×10^{-6} Torr MeOH vapor and at 300°C. a-d HRTEM images depicting Cu_2O nano-island shrinking over time. e Time-dependent change of the radius (half width) and height of the buried Cu_2O nano-island (marked in b) during reduction.

5.3.3 Atomic-scale dynamic of Cu_2O and interfacial transformation

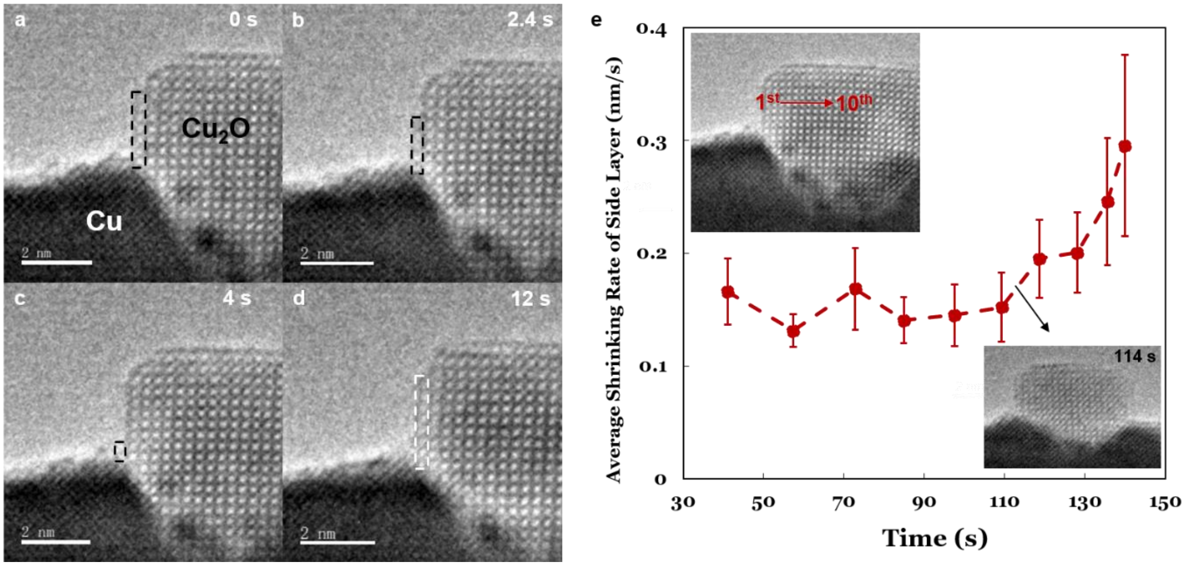

Figure 29. Monolayer by monolayer reduction of Cu_2O nano-island in Figure 26(b) under MeOH. a-d high magnification view of the dynamics of the Cu_2O monolayer reduction at under 7.6×10^{-6} Torr MeOH vapor and at 300°C, the black dashed box marks the vertical atomic side layer of Cu_2O nano-island. e Average shrinkage rate of 10 side layers on the left (dark red) before the island start tilting and collapsing, the inset image shows the appearance of Cu pile at 114 s and leads to subsequential acceleration of shrinkage of each layer.

In situ videos during reduction also reveals atomic-scale dynamics of the Cu_2O nano-island. Figure 29 shows an in situ TEM observation of how the Cu_2O nano-island in Figure 26(b) is being reduced monolayer by monolayer under MeOH. Black dashed frames highlight the vertical atomic layers on the side of the island. Figure 29a mark the starting point (0 s) for this time sequence. During the reduction process, the side layer of Cu_2O island perpendicular to the Cu(110) substrate is being reduced, while its height decrease vertically until the entire layer is removed as shown in Figure

29c. This entire process takes about 4 s before the next side layer starts being reduced at around 12 s (Figure 29d). However, the top layer of the oxide island does not change at all during this process. It maintains its initial position and the overall island height does not change by comparing Figure 29a→d. Therefore, the Cu_2O nano-island is being reduced by MeOH solely from the side through this iterated monolayer-by-monolayer removal process. The observation here is consistent with the measurement from Figure 29e, in which only radius is decreasing during the first 120 s of reaction. Similar shrinking dynamic of side layers can be also observed in Figure 30 a→d. The rate of shrinkage for each side atomic layer can be further quantified through *in situ* videos. Figure 29e shows an average shrinking rate of 10 side layers on the left side of the island before the island start tilting and collapsing. As can be seen, the shrinking rate of the left side of the island generally stays at around 1.5 nm/s during the first 6 layers (before 110 s). Starting at the 7th layer, the shrinking rate starts increasing for each layer and finally reaches about 3 nm/s for the 10th layer which happens right before the island starts tilting at around 147 s. The shrinking rate of layers on the right side of the island are also quantified. However, they observe a lower shrinking rate with only 4 layers being reduced within the same amount of time. This is probably due to the uneven reaction rate on both sides of the island, which could be caused by present defects. Shrinking rate of layers for the island in Figure 26(c) is also quantified and showed in Figure 30(e). Unlike the rate acceleration for the first island observed in Figure 29(e), the average shrinking rate of side layers for the second island is around 1 nm/s and the rate stays generally constant for total of 20 side layers that are quantified as shown in Figure 30(e).

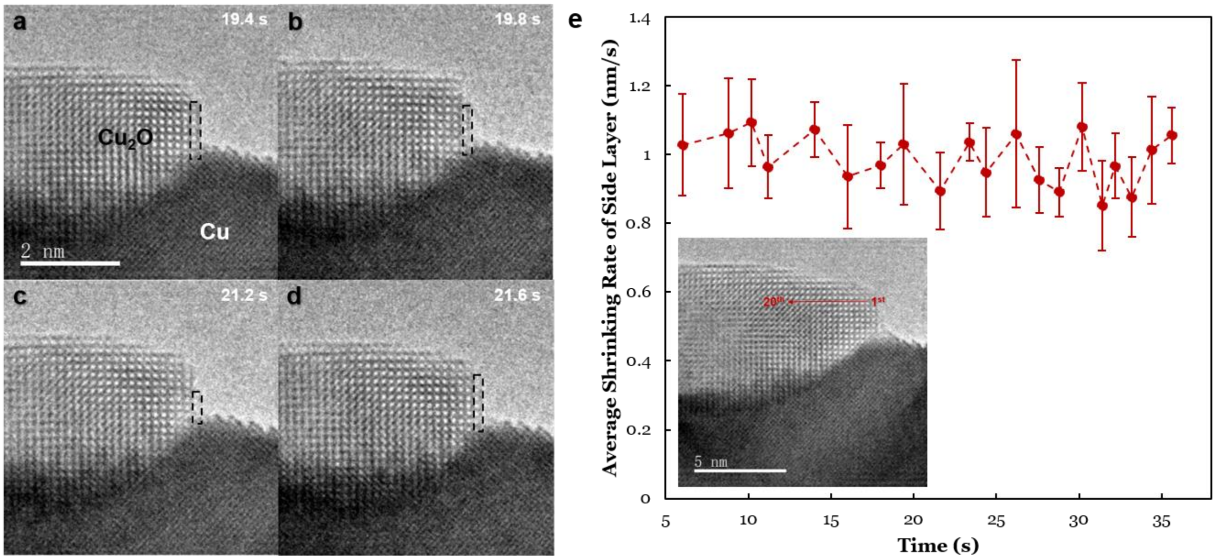

Figure 30. Monolayer by monolayer reduction of Cu_2O nano-island in Figure 26(c) under MeOH. a-d high magnification view of the dynamics of the Cu_2O monolayer reduction at under 7.6×10-6 Torr MeOH vapor and at 300°C, the black dashed box marks the vertical atomic side layer of Cu_2O nano-island. e Average shrinkage rate of 20 side layers on the right (dark red).

The removal of buried Cu_2O is attributed to the interfacial transformation from Cu_2O to Cu. Figure 31a-c show snapshots of the Cu_2O//Cu interface around the buried Cu_2O portion at higher magnification. The blue, red and yellow arrows help to trace the movement of the Cu_2O/Cu interface depicted in Figure 31. The Cu_2O//Cu interface is initially flat with the presence of atomic steps highlighted by blue arrow at Figure 30a. The atomic step at the interface serves as a starting point for the $Cu_2O \rightarrow Cu$ transformation. The conversion propagates along the Cu_2O/Cu interface which has a (100) orientation. The red and yellow arrows in Figure 31b & 31c point to the new locations of atomic steps at 8.4 s and 10.6 s, respectively. Therefore, the side of buried Cu_2O is being reduced via the $Cu_2O \rightarrow Cu$ interfacial transformation along the (100) direction.

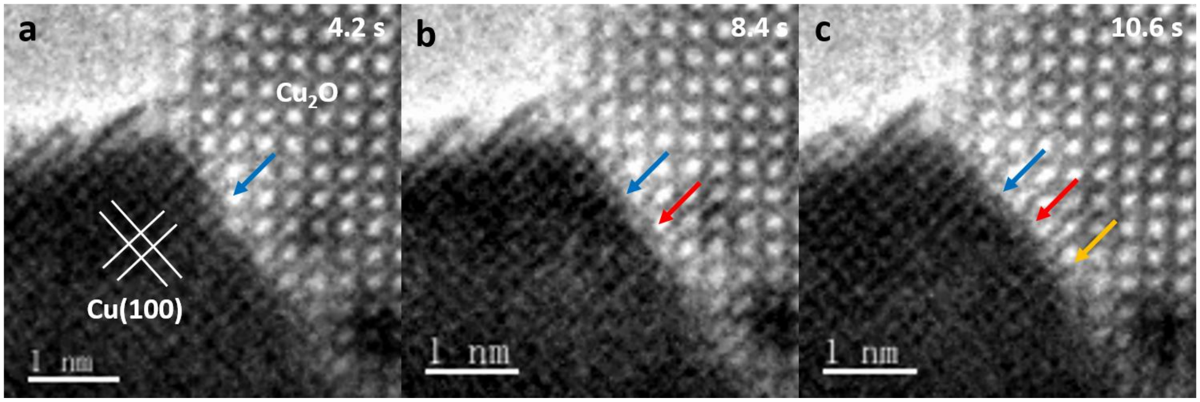

Figure 31. Cu_2O→Cu interfacial transformation at Cu_2O nano-island bottom in Figure 26(b). a-c HRTEM snapshots showing the Cu_2O→Cu conversion at the Cu_2O/Cu interface under 7.6×10^{-6} Torr MeOH vapor and at 300°C, the blue, red and yellow arrows point to the Cu_2O/Cu interface step edge at 4.2 s, 8.4 s and 10.6 s, respectively.

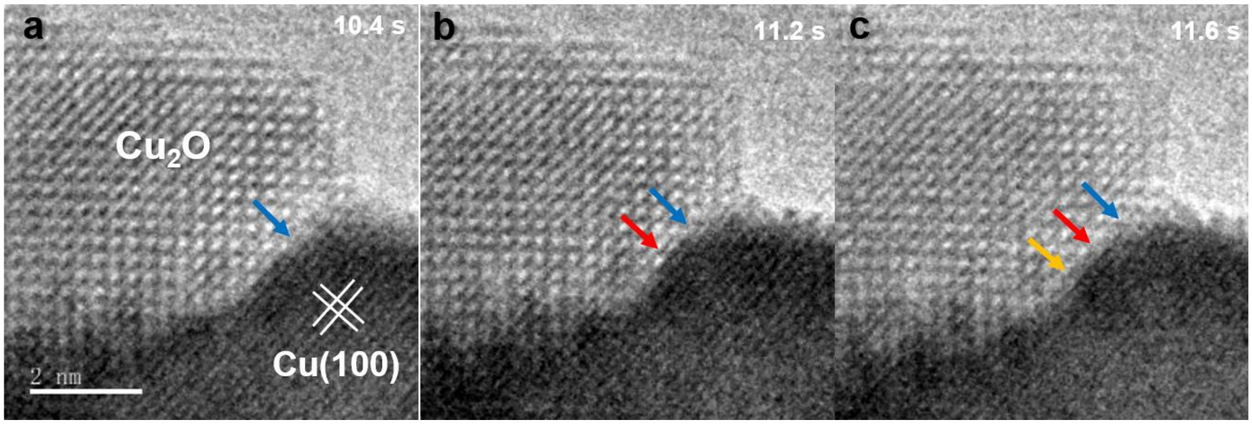

Figure 32. Cu_2O→Cu interfacial transformation at Cu_2O nano-island bottom in Figure 26(c). a-c HRTEM snapshots showing the Cu_2O□Cu conversion at the Cu_2O/Cu interface under 7.6×10^{-6} Torr MeOH vapor and at 300°C, the blue, red and yellow arrows point to the Cu_2O/Cu interface step edge at 10.4 s, 11.2 s and 11.6 s, respectively.

5.3.4 Tilting and collapsing of Cu_2O island

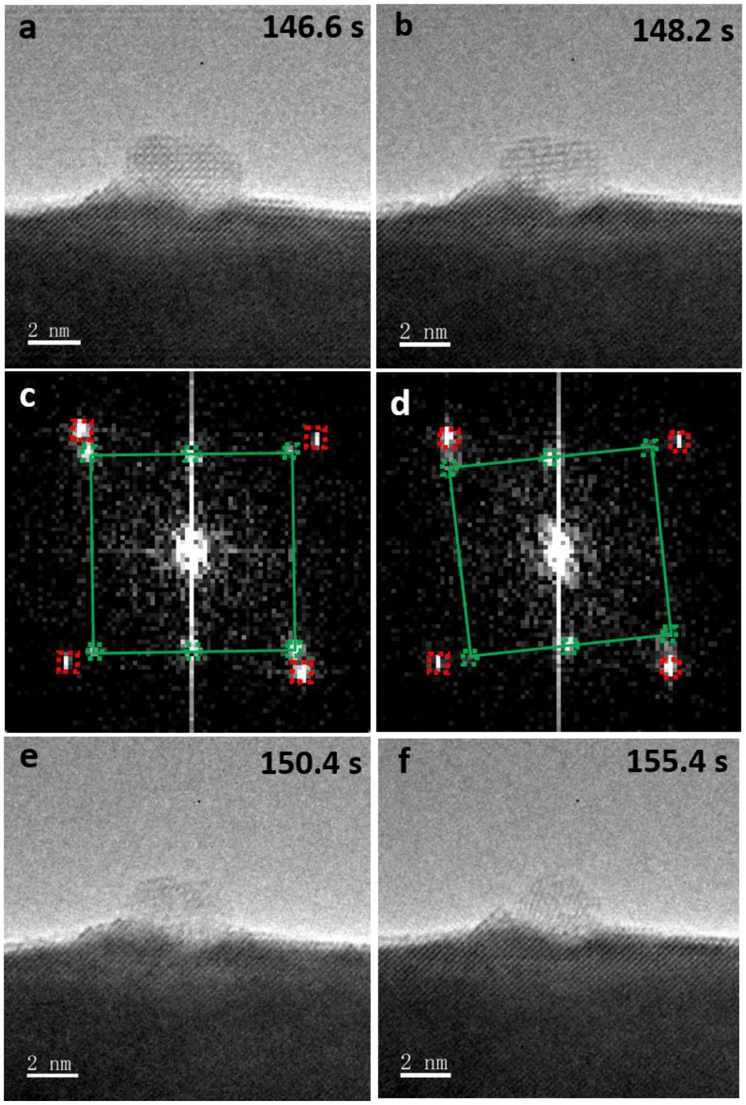

Figure 33. Tilting and collapsing of Cu_2O nano-island under MeOH. a, b, e, f Time-sequence HRTEM images of late-stage of Cu_2O reduction under 7.6×10^{-6} Torr MeOH vapor and at 300°C. c, d FFT of HRTEM images a and b, red dashed squares mark the Cu diffractions spots; green dashed circles and green lines illustrate the diffraction spots for Cu_2O.

During the last 20 s of the reduction, the Cu_2O nano-island starts to tile and then is reduced completely. From Figure 33a to 33b, the island starts tilting towards its left where there is a huge Cu pile accumulated beneath the island. Figure 33c and 33d are the diffractograms of 5a and 5b. As highlighted in green spots and lines from Figure 31c, the Cu_2O island shows two-dimensional lattice fringes and maintains its epitaxy with the Cu(110) substrate (highlighted in red). At 148.2 s, the Cu_2O island start losing its epitaxy with the Cu substrate due to a counter-clockwise tilting of 7°, as is measured from Figure 33d. The island tilts to further to its left and starts losing its lattice fringe contrast at around 150 s. Upon further tilting and reducing, the left half of the island has collapsed and the Cu_2O island has now turned into a round particle, namely with radius less than 2 nm as shown in Figure 33d.

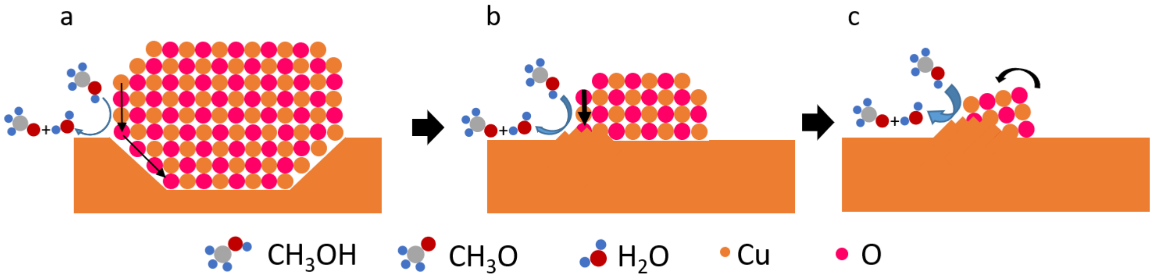

Figure 34. Schematic illustration of the reduction process. Reaction of methanol molecules with lattice oxygen in Cu_2O at perimeter site forms methoxy and water molecules that desorb from the surface, causing layer-by-layer shrinkage for the side layer of Cu_2O. a At the metal oxide interface, Cu_2O is gradually reduced through $Cu_2O \rightarrow Cu$ transformation at Cu_2O//Cu(100) interface. b Cu start accumulating at perimeter site when buried Cu_2O is reduced, the rugged perimeter leads to enhanced reaction rate of MeOH reduction and faster shrinkage rate of side layer. c Cu keeps accumulating and finally lead to tilting of Cu_2O island.

5.4 CONCLUSION

The present study employed the in situ ETEM to monitor the transformation of Cu_2O islands on Cu(110) at atomic level under MeOH reducing environment. We revealed that the reduction of Cu_2O under MeOH on Cu(110) substrate proceeded through layer by layer shrinkage along the side layers of Cu_2O island and interfacial transformation of Cu_2O to Cu initiated at step sites along interface. Additional accumulation of O vacancies on Cu_2O//Cu(110) interface resulted in build-up of Cu along interface, which further accelerate the shrinking process and further lead to the tilting and collapsing of the Cu_2O island. The entire reduction process is demonstrated in schematics shown in Figure 34. We then proposed that the preferential dissociative adsorption of methanol molecules along perimeter of Cu_2O islands led to the atomic dynamic described above which was further verified using DFT.

Although we observed two shrinking regimes existed during the reduction similar to our previous study on Cu(100), we found that the underlying mechanism at atomic level on Cu(110) is distinctly different thanks to the access of in situ capabilities using ETEM. Building on our study on Cu_2O reduction on Cu(100), the present study revealed additional atomistic insights on the active sites of Cu_2O nano-island on Cu(110) during reductive shrinking under MeOH. Our results suggest that creating additional structural irregularity along Cu_2O/Cu perimeter could further enhance the rates of methanol reformation on Cu_2O nanoparticles. Furthermore, our work demonstrated that the fundamental impact of metal substrate on determining reaction mechanisms during metal oxide reduction. The atomic-level evolution observed during the entire Cu_2O reduction process significantly complement and enhance the current understanding of metal oxide reduction as well as reaction mechanisms. These observations have broader impact on understanding supported oxides in heterogeneous catalysis and general gas-solid reaction kinetics.

6.0 OUTLOOK

Overall, this dissertation demonstrates experimental approaches on correlating activity of Cu based material in methanol oxidation with its oxidation states, atomic structure at Cu_2O surface and Cu_2O/Cu interface. In Chapter 3.0 , metallic Cu was found to be responsible for H_2 generation from partial oxidation of methanol while Cu^{1+} promotes water production. In Chapter 4.0 , atomic steps on surface of Cu_2O nanoparticle on Cu(100) was showed to be very effective in facilitating dissociative adsorption of methanol which is one of the key steps for methanol oxidation on Cu catalysts. Chapter 5.0 further shows the decisive role of Cu_2O/Cu(110) interface in determining the preferential adsorption site of methanol and facilitating phase transformation between Cu and Cu_2O during methanol induced reduction. Future investigation should focus on bridging the gap of pressure between current in situ experiments which are running at high vacuum (10^{-4}~10^{-3} Torr) and real catalytic reaction condition which typically runs at atmosphere or even higher pressure. Moreover, upgrade the current Cu single crystal sample (model catalyst) used in in situ TEM experiments to industrial type of Cu nanoparticles should also reveal more direct structural-activity correlation for methanol oxidation catalyzed by Cu based material.

In summary, suggested directions for future work are focused towards three key areas, which can be understood as three projects for future research:

1. Cu_2O/Cu interface has been showed to play a key role in determining the crystal structure of Cu_2O nano island and the preferential site for methanol dissociative adsorption in previous chapters. To further complete and complement the work already done on Cu(100) and Cu(110) facets, probing the structure-activity relationship for Cu oxide island formation and reduction on Cu(111) facet – the remaining unstudied facet among all three Cu lower indexed facets –under MeOH or MeOH/O_2 mixture using ETEM is necessary.

2. One limitation for the experimental approach used in Chapter 3.0 is that sample's reactivity and chemical composition were not evaluated under exact same conditions. In order to extend the understanding of Cu active phase during catalytic reaction, Cu oxidation state should be correlated with Cu catalyst reactivity at elevated pressures (different O_2/MeOH feed ratios) using AP-XPS attached with RGA.

3. To better represent the industrial Cu/ZnO catalysts and correlate the structure aspects such as Cu nanoparticle shape and Cu/ZnO interface with reactivity, model Cu/ZnO catalysts with well-defined structure should be synthesized and investigated under MeOH or MeOH/O_2 mixture using ETEM.

APPENDIX A

COMUTATIONAL DETAILS FOR CHAPTER 3

For calculations assessing adsorption energetics and diffusion activation energy barriers, an energy cutoff of 400 eV was employed. Corresponding Brillouin-zone integration was performed using (4×2×1) *k*-point meshes based on Monkhorst-Pack grids [205] and with broadening of the Fermi surface according to the Methfessel-Paxton smearing technique [206] applying a smearing parameter of 0.2 eV. Derivation of the Hubbard *U* value applied to all Cu_2O surface systems studied was completed by applying first-principles linear response theory [128] to a (2×2×(22), 48 atom bulk Cu_2O system employing a 600 eV energy cutoff and a (8x8x8) Monkhorst-Pack sampled *k*-point mesh set relative to the Cu_2O unit cell.[205] In linear response calculations, Hubbard *U* parameters are applied to the 3*d* orbitals of Cu atoms with 4*b* site symmetry characterized by the *Pn*-3*m* structural symmetry. Projector Augmented Wavefunction (PAW) pseudopotentials and the Perdew-Burke-Ernzerhof (PBE) parameterization of the generalized gradient approximation (GGA) functional were also used in these linear response calculations, [207, 208] with other attributes of these linear response calculations matching those employed in surface adsorption and diffusion calculations or – when this cannot be accomplished – the VASP linear response calculator developed in Curnan et al. [129].

The vector lengths of the planes perpendicular to the cell dimensions of surface adsorption and diffusion calculations containing a vacuum for (100), (110), and (111) surfaces are 8.54 Å x 12.81 Å, 9.80 Å x 13.86 Å, and 6.04 Å x 12.08 Å, respectively. Structural optimizations of these surface slabs were completed until all force components acting on non-fixed atoms were below 0.02 eV/Å. Successive slabs were separated by a vacuum region of 12 Å.

In determining how to address the presence of possibly unphysical electronic correlation interactions affecting Cu-O bonding and thus the results of pertinent adsorption site energy and NEB calculations, multiple issues potentially affecting the magnitude of the Hubbard *U* term modifying this interaction were considered. For example, the application of a Hubbard *U* resolved for a fully coordinated Cu_2O bulk system may not represent the constant partial coordination of surface Cu not directly displaced during NEB calculations or the varying coordination of surface Cu directly involved in the displacements performed through NEB. However, given that the effect magnitude (about 0.3 eV) observed when changing the coordination of oxygen-bonded metal atoms in past research [130] is within the measurement uncertainty of the calculated *U* value (0.54 eV), the magnitude of this concern is not significant with respect to the limitations of the linear response calculation. Given also that a single value of Hubbard *U* is required to directly compare the energetics of different NEB images depicting a common reaction pathway, the resolved *U* value of 7.5 eV is applied to all images of studied diffusion paths. Additionally, note that values of *U* within the uncertainty of the linear response calculation result ($U_{eff} = 7.45 \pm 0.54$ eV) have been applied to successfully describe energetics, electronic structure, and structural characteristics of Cu-O surface systems distinctly different from their analogous bulk structures. [123]

Additional concerns contributing to differences between studied Cu surface systems or corresponding bulk calculations include the effects of surface orientation on the oxidation states of variously layered Cu adjacent to desorbing O, in addition to the varied use of either PW91 or Perdew-Burke-Ernzerhof (PBE) functionals.[207, 208] These concerns can be addressed by observing that empirically fitting *U* to the electronic structure and magnetic properties of CuO and Cu_2O systems with and without defects studied using PBE and PW91 functionals[209, 210], as well as performing first-principles constrained DFT *U* calculations on the 3*d* orbitals of Cu in CuO using the PBE functional[211], yield *U* values (7.00-7.14 eV) within the previously mentioned measurement uncertainty. The additional empirical fitting of *U* to different albeit related properties yields qualitatively consistent values of 6-8 eV,[212, 213] while *U* values lower than this are generally achieved while employing different pseudopotentials.[212, 214] Pseudopotential selection is known to potentially have significant effects on first-principles calculated *U* results.[215]

Though very recent work on CuO surface chemistry has fitted a Hubbard U value of 4.5-5.5 eV to the adsorption energy of H_2 on CuO and less successfully applied a value of $U = 7$ eV to Cu in these calculations, note that this has been applied to describe Cu-O bonding affected by O-H bonding. A range of local structural coordination changes representative of coordination changes occurring during the reaction or diffusion processes affected linear response *U* measurements much less (~0.3 eV) [127, 216] than the range of *U* differences between the values of *U* mentioned previously (1.5-2.5 eV). [217] Changes in Cu oxidation state observed in studied systems from Cu^{+1} to Cu^{+2}, vice versa, or between other oxidation states – which are characteristic of transitions from Cu_2O to CuO bulk structures – also have been demonstrated to likely produce smaller effects on implemented Hubbard *U*, as linear response calculations have resolved smaller differences (~0.3 eV) between linear response derived Hubbard *U* for Cu_2O (7.45 eV in this study) and CuO (7.14 eV) [210]. Consider that the propagated uncertainty from both local coordination and Cu oxidation considerations (~0.43 eV) is less than the uncertainty of the linear response Cu_2O U_{eff} resolved in this study (0.54 eV), as well as that the difference between U values applied to represent Cu-O bonding affected [217] and not affected [123] by H bonding in past work (1.5-2.5 eV) is distinctly greater than both of these quantities. Therefore, the presence of H bonding local to studied reaction pathways – as opposed to isolated structural coordination or Cu oxidation state changes – is likely the most prevalent cause for the discrepancy between U values fitted from H_2 adsorption of CuO surfaces and U values derived for Cu_2O via linear response theory.

Calculations performed in this study do not feature O-H bonding and thus would not be affected by the postulated prevalent effects of H bonding on Hubbard U, rather only the smaller local structural and Cu oxidation state effects mentioned previously. Furthermore, even though anisotropic changes in relative surface defect energetics – which are comparable to adsorption site energetic differences – can occur with changes in Hubbard U, these are generally not sufficiently large to change adsorption site preferences. [123] Perhaps most importantly, energetic barriers to desorption of atomic species from Cu-O surfaces involving lattice O – which are of primary concern to the CO and CO_2 selective desorption energetics evaluated using NEB in this study – are show to change slightly (~0.01 eV) within selected U values ranging from 5 to 7 eV. [217] Therefore, though the effects of excluding consideration of Hubbard U in this study could be demonstrably large, inclusion of U = ~7 eV more accurately represents Cu-O systems excluding H bonding than inclusion of U = ~5 eV (which can be used when H bonding is present), site adsorption preferences are not expected to change within U = ~5-7.5 eV, and relative desorption energetic changes resulting from change within U = ~5-7.5 eV are inconsequential (~0.01 eV) in magnitude relative to the differences in CO vs. CO_2 desorption selectivity measured in this study (0.12-0.27 eV).

The determination of relaxed, bulk, cubic Cu_2O structure proceeded with the calculation of sets of constant volume, constant lattice dimension proportion (ISIF = 2) energies over ranges of consistently incremented lattice dimension or volume around the equilibrium calculated Cu_2O volume. This was completed for 1x1x1 or unit cell Cu_2O, while equilibrium lattice dimensions (a = 4.31 Å) were determined using the Birch-Murnaghan Equation of State (EOS), in strong agreement with analogous experimental results (a = 4.27 Å). [218] The volume fitted from this EOS was applied to 2x2x2 supercell representations of Cu_2O, forming a supercell to be relaxed for linear response analysis.

The bare perturbation response [214] required to calculate linear response derived values of Hubbard U needs an initially converged charge density (CHG) file as input when using the VASP calculation procedure detailed in Curnan et al. The other file contents completed to perform structural relaxations on 2x2x2 Cu_2O supercells are retained. The initial perturbations (χ_0) form the perturbation response over the range of perturbation values [-0.15, 0.15] (LDAUU and LDAUJ below) in increments of 0.05, in conjunction with the CHG file previously mentioned. All other files needed to relax Cu_2O are retained in these calculations. The final perturbations (χ) form the perturbation response over the range of perturbation values [-0.15, 0.15] (LDAUU and LDAUJ below) in increments of 0.05. All other files needed to relax Cu_2O are retained in these calculations.

Adsorption energy calculations for CO and CO_2 were performed on (100), (110) and (111) surfaces. Cu-terminated surfaces were used to model the (100) and (111) surfaces, and a Cu-O terminated surface was used for the (110) surface. For CO_2 adsorption site calculations, an O-deficient surface was used to simulate the removal of a lattice oxygen atom. The most stable configurations were determined by placing CO and CO_2 on the surface and varying the orientation and adsorption sites. The adsorption energy (ΔE) is calculated using the equation:

$$\Delta E = E_{ads} - E_{ref} - E_{gas} \tag{A-1}$$

Where E_{ads} is the total energy of the system including both Cu_2O surface and adsorbate, E_{ref} is the total energy of the surface without its corresponding adsorbate. E_{gas} is the energy of a molecule in its gas phase, calculated by placing an isolated molecule in a box. The table below states the adsorption energies, orientation (vertical or tilted), and the bonding site (Cu top or Cu bridge) for the most stable configurations of CO and CO_2. CO is bonded to the surface by its C atom, while CO_2 is bonded by its O atom.

Table 2. Adsorbate type, adsorption energies, MeOH orientation with respect to adsorbed surface (fully vertical/orthogonal or tilted), and adsorbate site (bridge or top) for the most stable adsorbate configurations on tested Cu(100), Cu(110), and Cu(111) surfaces.

Adsorbate	**(100)**		**(110)**		**(111)**	
CO	1.22 eV	Vertical Cu Bridge	0.26 eV	Tilted Cu Top	1.09 eV	Vertical Cu Top
CO_2	0.03 eV	Tilted Cu Bridge	0.10 eV	Tilted Cu Top	0.05 eV	Tilted Cu Top

APPENDIX B

TEM IMAGES AND QUANTITATIVE ANALYSIS FOR THE REST CU$_2$O ISLANDS IN CHAPTER 4

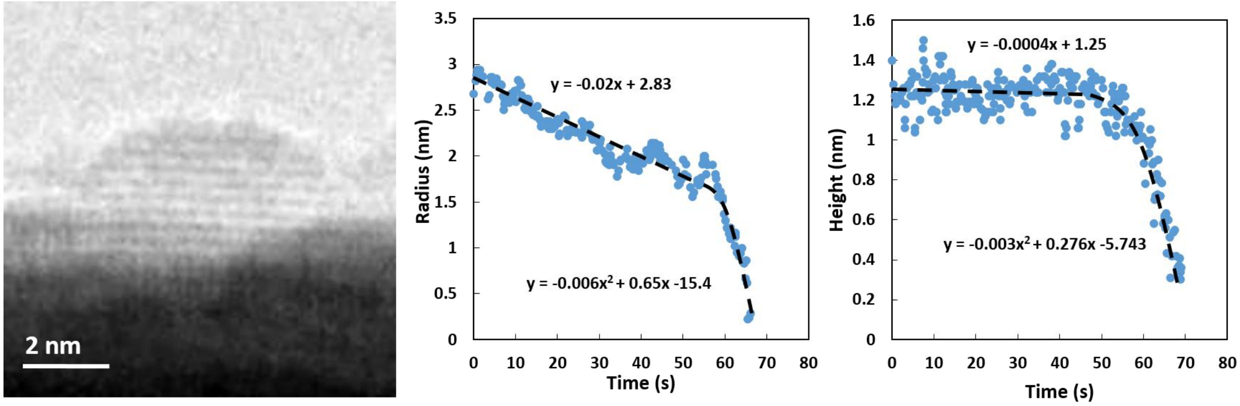

Figure 35. Shrinking profile of Cu$_2$O island (#1 in Table 1) with fitting parameters.

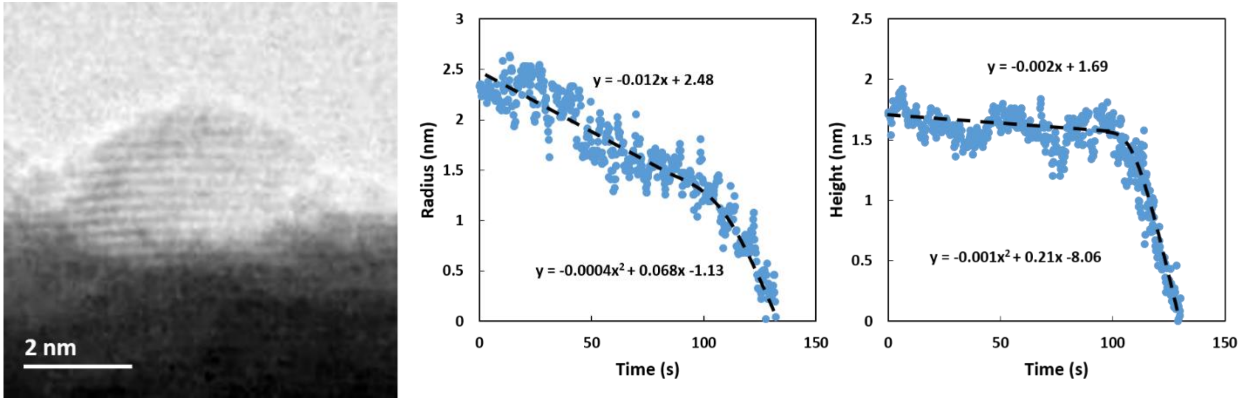

Figure 36. Shrinking profile of Cu_2O island (#2 in Table 1) with fitting parameters.

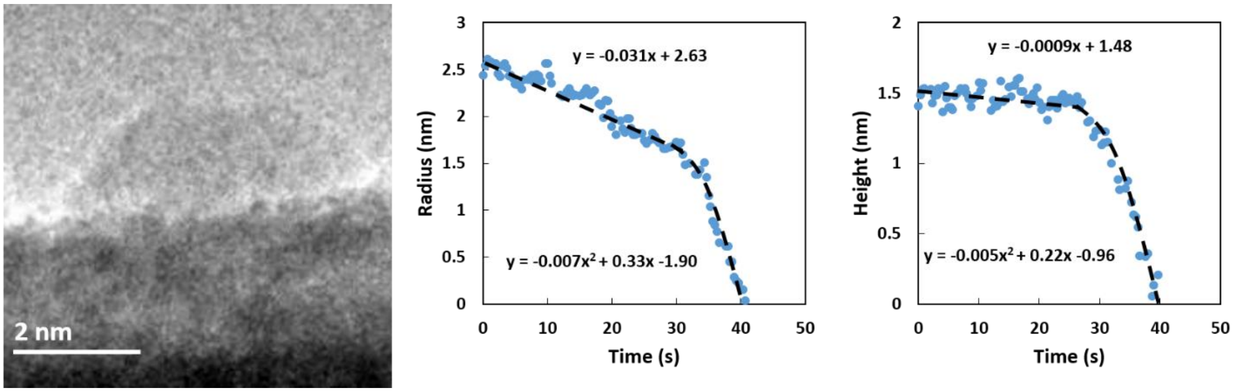

Figure 37. Shrinking profile of Cu_2O island (#3 in Table 1) with fitting parameters.

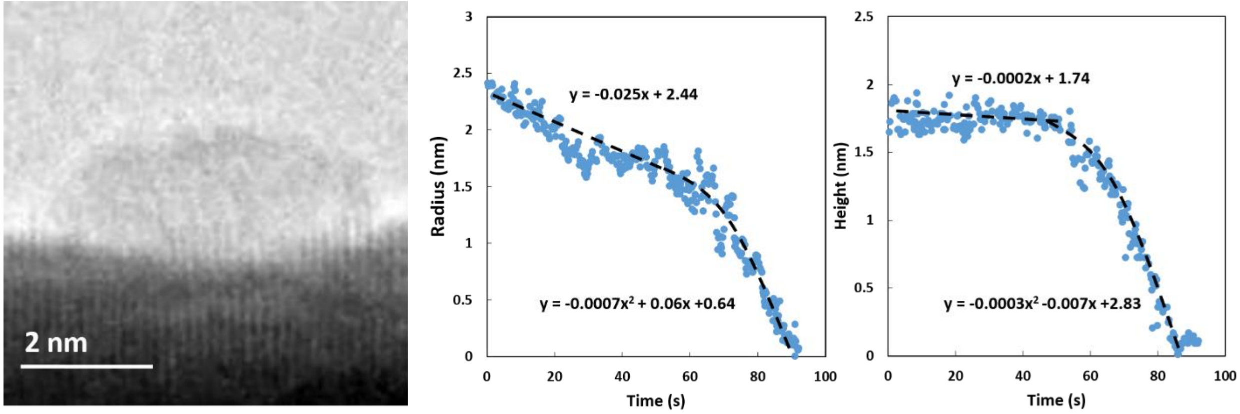

Figure 38. Shrinking profile of Cu_2O island (#4 in Table 1) with fitting parameters.

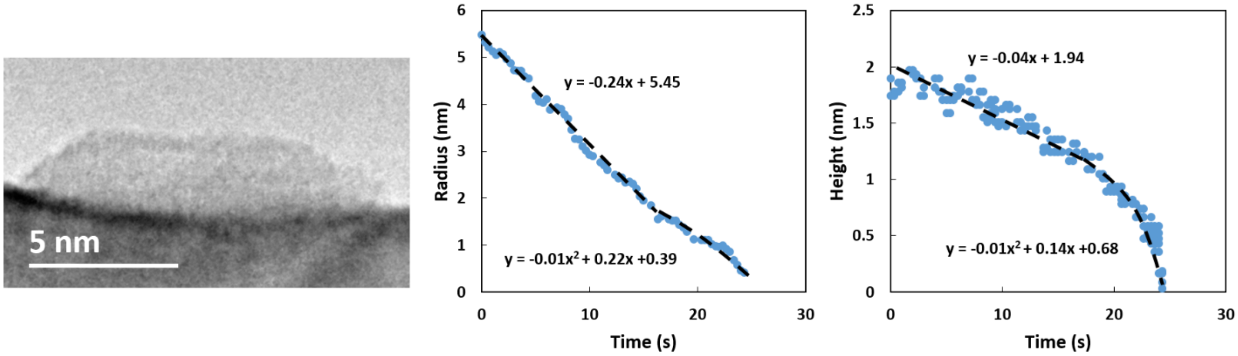

Figure 39. Shrinking profile of Cu_2O island (#5 in Table 1) with fitting parameters.

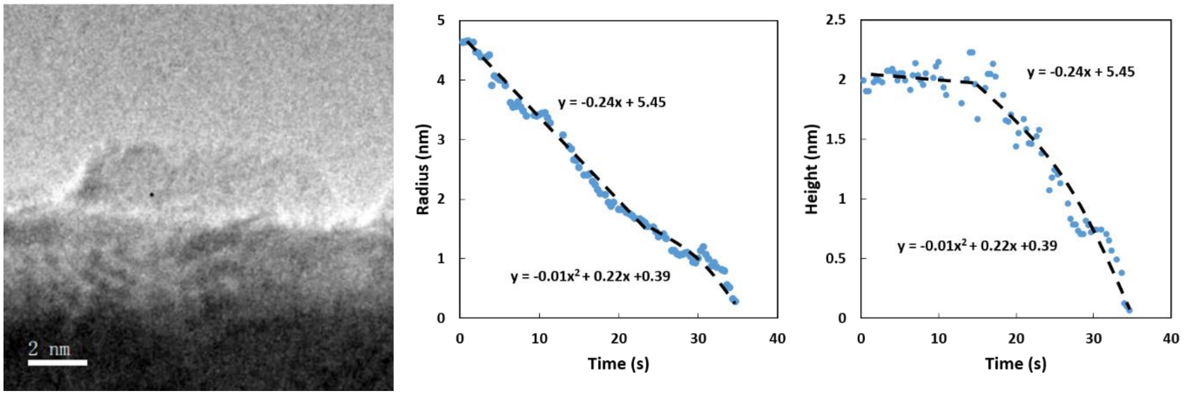

Figure 40. Shrinking profile of Cu_2O island (#6 in Table 1) with fitting parameters.

APPENDIX C

STATISTICAL APPROACH FOR IDENTIFYING CU2O SHRINKING RATE TRANSITIONS

As shown in Figure 35-50, studied Cu_2O islands shrink over two apparently distinct and regimes, the first of which features the anisotropic shrinking of island radius with relatively constant island height. The subsequent regime features the isotropic, relatively proportional shrinking of island radius and height. These two shrinking regimes characterize shrinking rates with different functional forms.

In order to preliminarily evaluate whether defined anisotropic and isotropic shrinking regimes have numerically distinct shrinking rates, the presence of breaks in shrinking rates at anisotropic-isotropic shrinking transition points will be determined via the Chow test which is a test of whether the true coefficients in two linear regressions on different data sets are equal. Modeled shrinking results from the diffusion of Cu away from oxide islands and to the perimeter formed by the island and its Cu substrate. The shrinking or dissociation of Cu_2O oxide islands with methanol (MeOH) reduction has been modeled as linear decay in past work. More specifically, this work has modeled Cu dissociation as linear atom loss along single island perimeter dimensions, as well as linear shrinking of surface areas along sets of two island perimeters. The latter of these descriptions can be equated to parabolic shrinking along single dimensions.

As can be calculated from Table 1 in the main document of this work, anisotropic shrinking rate ratios between radii and height of the seven islands tested observe a mean of 61.07, a minimum of 5.58, and a maximum of 211.09. Respective isotropic shrinking rate ratio statistics include a mean of 1.50, a minimum of 0.39, and a maximum of 2.52. Thus, Cu diffusion occurring in the anisotropic regime appears to occur largely (if not entirely) along a single dimension (radius) in this work. Therefore, anisotropic shrinking will be initially approximated via first-order rate kinetics during the Chow test. In contrast, isotropic Cu diffusion can occur primarily along either the height or the radius of a given island (usually radius), though all radius vs. height ratios are distinctly closer to unity in the case of isotropic than anisotropic shrinking. In this case, either first-order or second-order rate kinetics may potentially model Cu diffusion, depending on the proportionality of island shrinking along radius and height. For the purposes of determining the significance of the break between anisotropic and isotropic rates of shrinking within the limitations of the Chow test, isotropic shrinking will be initially evaluated using first-order rate kinetics. Nevertheless, future analysis within this Supporting Information will seek to determine whether first or second-order kinetics model isotropic shrinking more effectively.

Consistent with the assumptions and approximations made above and in past work, the shrinking of oxide islands can be modeled using the following reaction:

$$Cu_2O\ (s) + 2CH_3OH\ (g) \rightarrow 2Cu\ (s) + 2CH_3O\ (g) + H_2O\ (g) \qquad \text{(C-1)}$$

The methanol decomposition component of this reaction can be stated to explicitly indicate the production of O:

$$2CH_3OH\ (g) \rightarrow 2CH_3O\ (g) + 2H\ (g) \tag{C-2}$$

$$2H\ (g) + O\ (g) \rightarrow H_2O\ (g) \tag{C-3}$$

Combination of [C-1], [C-2], and [C-3] ([C-1] - [C-2] - [C-3]) yields the reaction shown in past work:

$$Cu_2O\ (s) \rightarrow 2Cu^0\ (s) + O\ (g) \tag{C-4}$$

Applying reaction [C-4] and first-order rate kinetics to anisotropic ($r_a = k_a$ [Cu]) and isotropic ($r_i = k_i$ [Cu]) island shrinking as tentative approximations, two linear regression models can be derived from given rate equations for the Chow test as follows:

$$r_j = \frac{d[Cu]}{dt} = k_j[Cu] \mid j = a\ (anisotropic)\ OR\ i\ (isotropic) \tag{C-5}$$

$$\frac{d[Cu]}{[Cu]} = k_j dt \rightarrow \ln([Cu]) = -k_j t + \ln([Cu]_0) \tag{C-6}$$

$$y_j = \ln([Cu])_{t,j} \,\Big|\, y_{0,j} = \ln([Cu]_0)_j \,\Big|\, x_j = k_j t \rightarrow y_{t,j} = -k_j x_{t,j} + y_{0,j} + \varepsilon \tag{C-7}$$

The Chow test evaluates the Sums of Squared Residuals (SSR) of both combined (a + i) and separate (a, i) anisotropic and isotropic shrinking measurement regressions. Given respective sample sizes N_a and N_i, as well as the number of parameters tested (k), the Chow test inferentially evaluates whether the two regressions depicted above are equivalent using the null hypothesis (H_0), alternate hypothesis (H_A), and F-statistic shown below:

$$H_0\colon \ln([Cu]_0)_a = \ln([Cu]_0)_i \ AND\ k_a = k_i \tag{C-8}$$

$$H_A\colon \ln([Cu]_0)_a \neq \ln([Cu]_0)_i \ AND/OR\ k_a \neq k_i \tag{C-9}$$

$$F = \frac{[SSR_{a+i} - (SSR_a + SSR_i)]}{(SSR_a + SSR_i)/(N_a + N_i - 2k)} \tag{C-10}$$

For these calculations, note that the breakpoints or transition points defining the anisotropic and isotropic regimes were taken from Figure 22 and derived using the Levenberg-Marquardt (LM) Algorithm and piecewise function analysis routines of the Origin software platform. Results presented in the table and figures below were achieved using the “gap” and “nortest” packages, as well as other built-in routines, of the R statistical software platform.

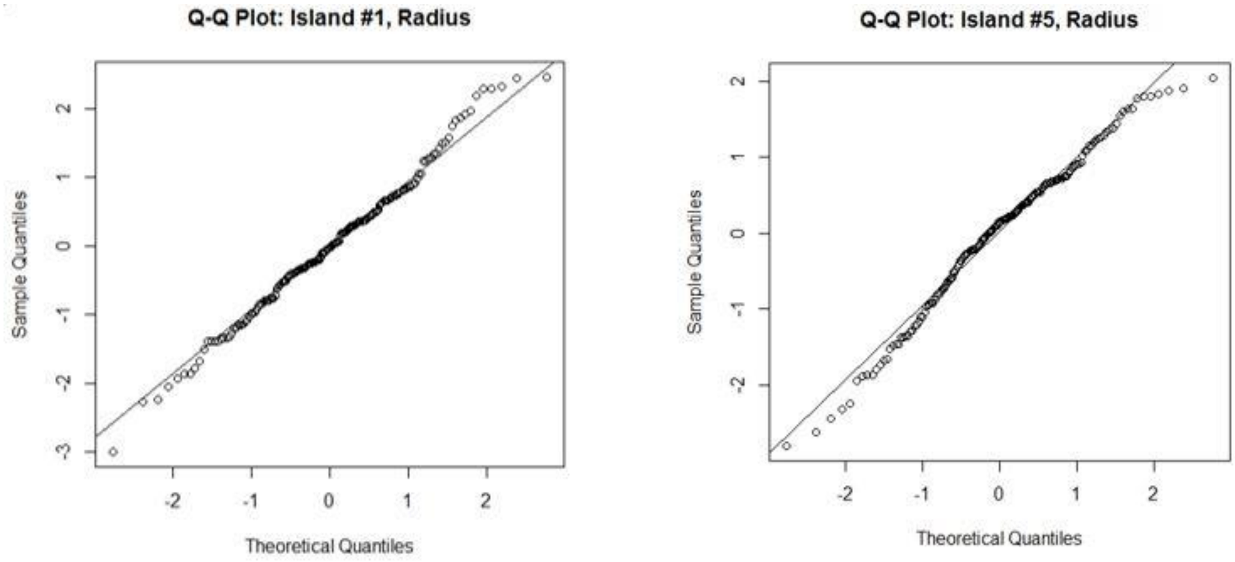

Figure 41. Sample Quantile-Quantile (Q-Q) plots depicting the normality of the regression residuals (ε) of island (#1 and #5) radii shrinking in anisotropic regimes.

The Chow test assumes that regression residuals (ε) are independently and identically distributed from a normal distribution. A representative illustration of the normality of sample regression residuals, which is shown in Figure 41 in Quantile-Quantile (Q-Q) plots, indicates that sample deviations from a normal distribution – or deviations from the 45° degree lines in plotted data – occur almost entirely in ranges of data more than one quantile away from fitted regression results and at sparsely sampled distances from those results. The Shapiro-Wilk test results of island #1 (*p*-value = 0.299), which is representative of most sampled islands, and island #5 (*p*-value = 0.057) show that rejecting the overarching assumption of regression residual normality under a quantitative premise can only occur by using a large confidence interval (such as $\alpha = 0.1$). In combination, these Q-Q and Shapiro-Wilk results indicate that pertinent data is normally distributed or approximates being normally distributed to the extent of not impeding Chow test evaluations, given that Chow test *p*-values are sufficiently lower than typically given confidence intervals (such as $\alpha = 0.05$).

As can be shown in Table 3 below, Chow test results for each island (1-7) and both its radius (*r*) and height (*h*) dimensions reveal that the null hypothesis can be strongly rejected for all sampled islands. Therefore, distinct anisotropic and isotropic regimes are statistically justified for the analysis completed in this paper, especially considering the very low magnitude of all *p*-values evaluated and the further statistical evaluation of this data completed below.

Table 3. F-test, degrees of freedom, and p-values serving as output from Chow tests for each island and shrinking dimension over both anisotropic and isotropic regimes.

Island #	Dimension	*F*-value	$N_a + N_i - 2k$	*p*-value
1	r	234.	216	8.96×10^{-55}
2	r	197.	551	2.70×10^{-65}
3	r	181.	97	1.89×10^{-33}
4	r	46.4	61	5.68×10^{-13}
5	r	211.	346	1.47×10^{-60}
6	r	20.6	82	5.71×10^{-8}
7	r	91.6	102	1.67×10^{-23}
1	h	413.	280	3.01×10^{-84}
2	h	210.	527	1.04×10^{-67}
3	h	99.0	90	1.86×10^{-23}
4	h	39.4	60	1.18×10^{-11}
5	h	333.	280	1.02×10^{-74}
6	h	48.0	74	4.27×10^{-14}
7	h	51.4	51	5.98×10^{-13}

In order to evaluate whether isotropic shrinking is characteristic of first or second-order rate kinetics, the Akaike Information Criterion (AIC) of each system is resolved. Relative AIC (ΔAIC) values evaluate the trade-off between the inclusion of additional parameters to different models and the minimization of their errors, determining whether the information loss observed by different kinetic models can justify the subtraction of terms from them. Lower ΔAIC values comparing different kinetic models sharing the same data set indicate better model quality with respect to their ordering and their relative magnitudes. Through the analysis performed below, the AIC of linear (first-order) decay models without two distinct anisotropic and isotropic rates (L), linear decay models with two distinct rates (L+L), and a model with anisotropic linear decay and isotropic parabolic (second-order) decay (L+P) are compared. Therefore, this analysis determines whether the addition of parameters required to distinguish two separate kinetic rates from one another is justified relative to observed error reduction, as well as whether error is best minimized by applying first or second-order rate kinetics to the isotropic regime. Also note that, given AIC orderings and relative AIC magnitudes of L, L+L, and L+P models of the same shrinking data are being compared, relative results will not vary with monotonic logarithmic transformations of data. AIC results are summarized in Table 4 below.

Table 4. Differences in AIC results between L, L+L, and L+P models for each shrinking dimension of each island over both anisotropic and isotropic regimes.

Island #	Dimension	ΔAIC (L)	ΔAIC (L+L)	ΔAIC (L+P)
1	r	662	6.02	0.00
1	h	242	10.9	0.00
2	r	986	39.9	0.00
2	h	1790	373	0.00
3	r	89.0	0.00	4.63
3	h	237	46.5	0.00
4	r	8.44	2.54	0.00
4	h	1.77	8.60	0.00
5	r	317	84.2	0.00
5	h	320	23.7	0.00
6	r	86.5	1.84	0.00
6	h	166	4.37	0.00
7	r	542	113	0.00
7	h	95.8	2.36	0.00

As can be shown in Table 4, L+P models are almost universally favored over L+L and L models, while L+L models are almost universally favored over L models. Given the relative magnitudes of differences between L+P and L+L models, as well as those between L+L and L models, distinguishing between two kinetic rates is very strongly preferred (L+L or L+P) over not doing so (L). In other words, L-P/L-L differences are much smaller than L-L/L differences, frequently by an order of magnitude. Therefore, the two-stage mechanism proposed in this work is both inferentially and informationally justified in a statistical context, given the decay model established in past work shows that L+P models should be used over L+L models in isotropic shrinking over surface areas. Also relative to these differences, exceptions to the general conclusions presented previously occur due to slight differences comparable in size to smaller L-P/L-L differences. Therefore, small quantities of these results can be classified as outliers.

Overall, these results numerically support that first-order rate kinetics describe the anisotropic regime and second-order rate kinetics describe the isotropic regime. Therefore, reactions modeling the rates of anisotropic (r_a) and isotropic (r_i) island shrinking resulting from anisotropic (k_a) and isotropic (k_i) kinetic rate constants can be described via:

$$r_a = k_a [\mathrm{Cu}] \tag{C-11}$$

$$r_i = k_i [\mathrm{Cu}]^2 \tag{C-12}$$

APPENDIX D

COMPUTATIONAL DETAILS FOR CHAPTER 4

Density Functional Theory (DFT) calculation results featured in this work were achieved using the Vienna *Ab Initio* Simulation Package (VASP, version 5.4.4). These calculations applied the Perdew Burke Ernzerhof (PBE) functional,[12] an electronic self-consistent loop break condition of $5x10^{-5}$ eV, and an ionic relaxation loop break condition of 0.02 eV/Å. Projector Augmented Wave (PAW) method resolved pseudopotentials for Cu, O, C, and H elements were used, namely those respectively labelled “Cu”, “O_s”, “C_s”, and “H”. The modeling of MeOH adsorption on Cu_2O interfaces, as well as the subsequent MeOH dissociation to form Methoxy and H adsorbates, was completed using the Climbing-Image Nudged Elastic Band (CI-NEB) method, with each CI-NEB calculation employing five images. DFT energetic comparisons were made between structures modeling flat $Cu_2O(100)$ surfaces and stepped $Cu_2O(100)$ interfaces with {100} oriented facets, which most closely resembled experimental structures. Modeled structures tested Cu and O terminated surfaces to consider a broader set of O surface coverage conditions. Selective dynamics were used to constrain the bottom half of the flat surface constituting both flat and stepped structures, as well as constrain the columns of atoms perpendicularly intersecting the top flat surfaces of stepped $Cu_2O(100)$ structures.

Initial determinations of energetically favorable candidates for MeOH adsorption and dissociation calculations were made using DFT calculations to screen for the most energetically stable dissociated (MeO and H adsorbates) Cu_2O surface structures that resembled the stepped and flat surfaces resolved in experiment. Pursuant to this screening, stepped $Cu_2O(100)\{100\}$ structures were evaluated, in accompaniment with complementary flat $Cu_2O(100)$ structures, while considering both Cu-terminated and O-terminated surfaces. Energetic results achieved during this screening used an energy cutoff (ENCUT) of 300 eV and were sampled only at the Γ-point (1x1x1 *k*-point grid). Calculations of MeO+H adsorption energies (after dissociated of adsorbed MeOH) were achieved using the expression below, with MeOH molecular energies determined using the convergence of similarly parameterized calculations with increasing box size (up to 12 Å x 12 Å x 12 Å):

$$\Delta E_{MeO+H} = E_{MeO+H} - (E_{MeOH} + E_{Cu2O}) \tag{D-1}$$

Using the above notation, MeO+H adsorption energies following dissociation (ΔE_{MeO+H}) are calculated from the DFT energies of simulations featuring separate adsorption of MeO and H adsorbates on a given Cu_2O interface (E_{MeO+H}), an isolated MeOH molecule (E_{MeOH}), and a corresponding Cu_2O interface calculation without any adsorbates (E_{Cu2O}). MeOH adsorption energy screening results for flat $Cu_2O(100)$ surfaces are summarily depicted for both Cu and O-terminated structures in Figure 42 below. Note that, in all structures visualized in future figures, Cu, O, C, and H atoms are respectively represented as blue, red, brown, and white spheres using the VESTA software package.

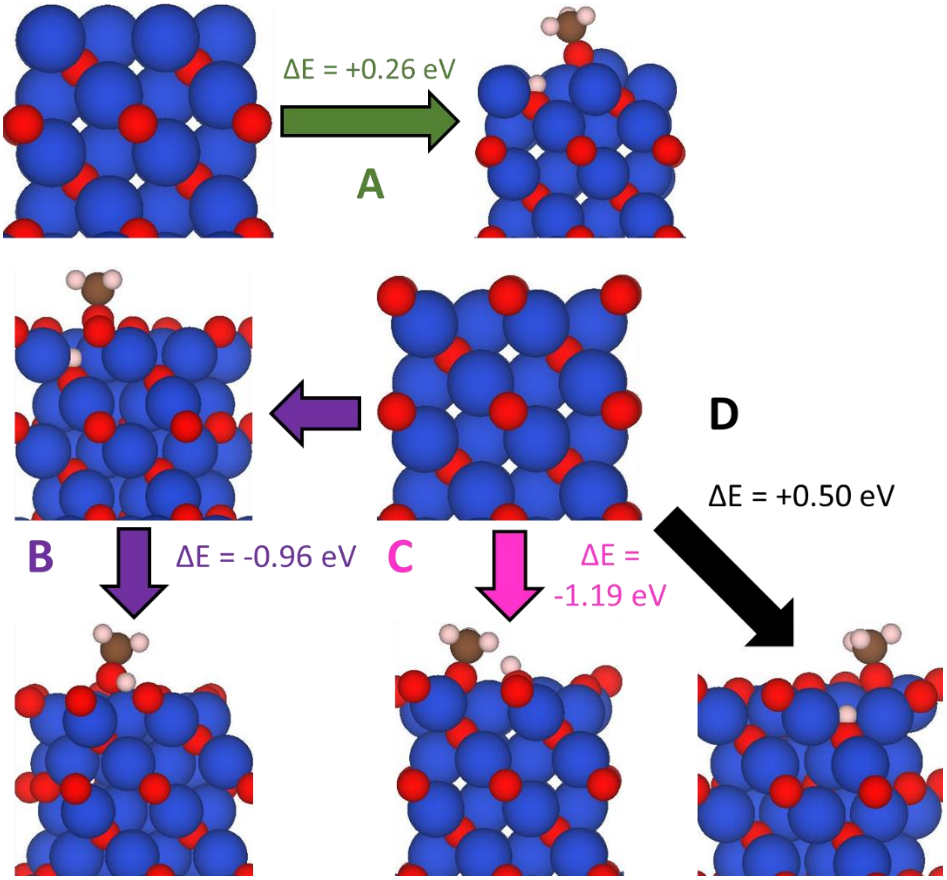

Figure 42. Flat $Cu_2O(100)$ Cu (A) and O-terminated (B, C, D) structures featuring MeOH adsorption energetics after dissociation of H to surface (B, C) and lattice (D) O sites.

Over all structures evaluated, note that the O atoms of MeO adsorbates initially had two-fold coordination, as each of them was most closely attached to single C and Cu atoms. In the case of the Cu-terminated flat $Cu_2O(100)$ surface (Figure 42A), only lattice or subsurface O atoms can bond to H atoms. Given that subsurface O atoms serve as nearly structurally equivalent sites for H adsorption from MeOH dissociation due to being in Cu surrounded environments, only the O atom nearest to the H atoms was tested. Relaxation of the MeO adsorbate upon dissociation yielded an adsorbed O with three-fold coordination and a relatively high adsorption energy (ΔE_{S13A} = +0.23 eV). This relaxation to three-fold coordination leads to a structure in which MeO adsorbates are closest to nearly structurally equivalent matching H adsorbate sites within three nearest-neighbor sites, further justifying past testing of only nearest neighbor sites.

Subsequently tested O-terminated flat $Cu_2O(100)$ surfaces (Figure 42B, 52C, 52D) initially evaluated four structures systematically, featuring H adsorbing to a nearest neighbor surface O (Figure 42C), nearest neighbor subsurface O, next nearest neighbor surface O (Figure 42B), and next nearest neighbor subsurface O (Figure 42D). The initial structure used to initialize the relaxed structure depicted in Figure 42B placed an H adsorbate on the nearest neighbor subsurface O, which then relaxed into a structure (Figure 42B) placing an H atom at an intermediate distance between the MeO adsorbate and the next nearest neighbor surface O adsorption site. Subsequent evaluations revealed that the most energetically favorable structure tested adsorbs H at the nearest neighbor surface O site (Figure 42C) and the least favorable structure adsorbs H at the next nearest neighbor subsurface O site. Consistent with previous calculations, MeOH dissociation to MeO leads to a transition from three-fold to two-fold coordination during relaxation. Also consistent with past work [69, 70], flat O-terminated surfaces are shown to much more (1.45 eV) favorably adsorb and dissociate MeOH.

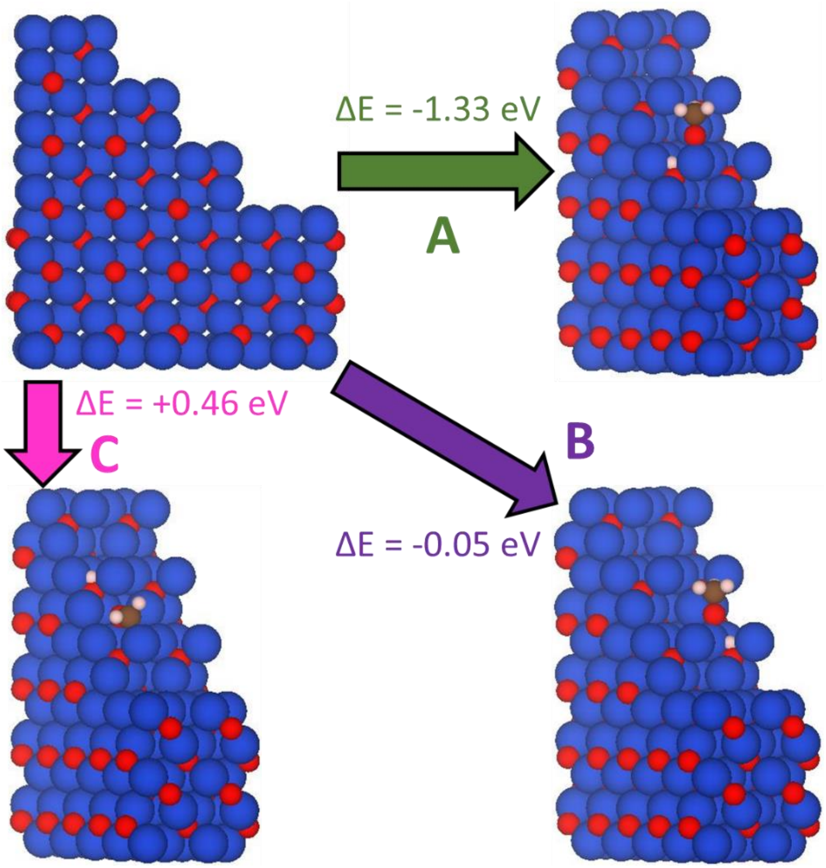

Figure 43. Cu_2O(100){100} Cu-terminated stepped surfaces with MeOH adsorption and dissociation, with MeO adsorption on shared (Figure 43B) or adjacent (Figure 43C) interfaces relative to H adsorbates, as well as MeO adsorption on step edge interfaces shared by H adsorbates (Figure 43A)

Cu-terminated Cu_2O(100){110} interfaces depict several sites for MeO and H dissociative adsorption that can be distinguished from one another based on the locations of MeO and H relative to one another. Given that O within Cu-terminated Cu_2O steps is solely located in the subsurface of the Cu_2O step, MeO adsorbate positions are limited to allow diffusion of H from MeOH to subsurface O in single linear paths. From this limitation, three distinct structures are readily defined and tested as candidates for MeOH dissociation, including MeO adsorbed to a {100} step edge that extends from a flat surface shared by a complementary H adsorbate (Figure 43A). Additionally, MeO can be adsorbed to a flat surface adjacent to an H adsorbate on a shared or adjacent (Figure 43C) flat surface. In each of these cases, initial two-fold coordination was given to MeO adsorbates, though relaxation generally lead to MeO assuming three-fold coordination. Over these cases, MeO adsorbing on the step edge (Figure 43A) is shown to be most energetically favorable.

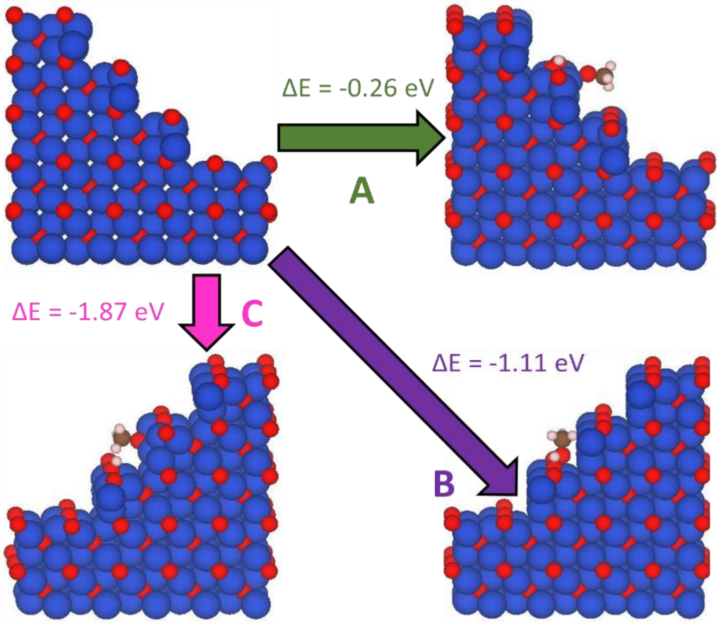

Figure 44. Cu_2O(100){100} O-terminated (O bonded to step edge) stepped surfaces with MeO adsorption on the same (Figure 44A) and adjacent (Figure 44C) step edges as H adsorbates, as well as MeO adsorption on flat surfaces shared by H adsorbates (Figure 44B).

Figure 44 and Figure 45 both depict Cu_2O(100){100} structures with O-terminations. However, the 6 atom P*n*-3*m* Cu_2O unit cell used for constructed all flat and stepped surfaces contains two O atoms that become symmetrically inequivalent when forming stepped $Cu_2O(100)$ surfaces. Figure 44 depicts MeO and H adsorption on O-terminated structures with O bonded to the Cu atoms constituting the edges of the stepped interface, while Figure 45 shows structures with O bonded to the corners formed from the perpendicular intersection of (100) planes constituting the $Cu_2O(100)\{100\}$ step. This perpendicular intersection renders evaluation of both terminations necessary. Upon evaluation, all structures tested in Figure 44 are found to be more favorable than those in Figure 45. In all cases, structures were initialized by applying two-fold coordination to the O of adsorbed MeO.

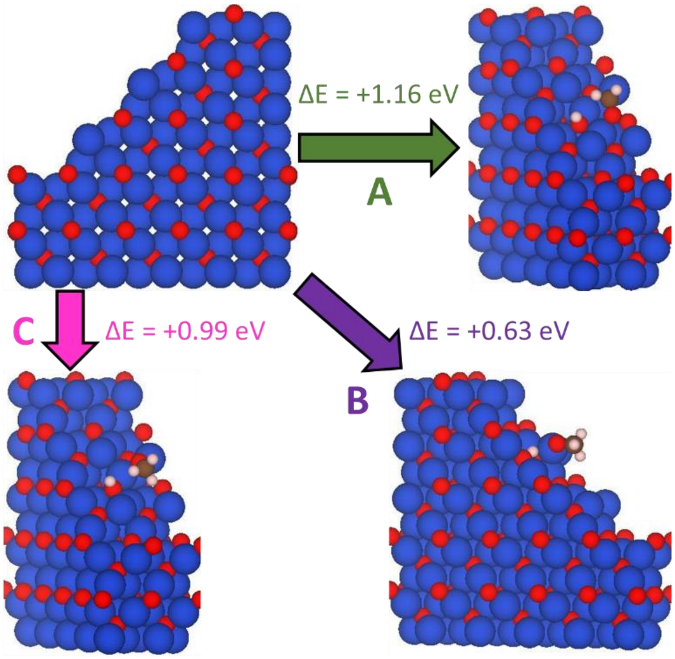

Figure 45. $Cu_2O(100)\{100\}$ O-terminated (O not bonded to step edge) stepped surfaces with MeO adsorption on the same (Figure 45B) and adjacent (Figure 45C) step edges as H adsorbates, as well as MeO adsorption on flat surfaces shared by H adsorbates (Figure 45A).

Applying screening criteria similar to those used to test MeO and H adsorption sites in Figure 43, tested structures include MeO on matching (Figure 44A) and adjacent (Figure 44C) steps as adsorbed H, with MeO adsorbed to two-fold coordinate Cu atoms forming step edges. Another structure tests MeO adsorbed to a three-fold coordinate Cu constituting a flat surface (Figure 44B), which is positioned adjacent to an adsorbed H. The most favorable structure, depicted in Figure 44C, features relaxation of a MeO adsorbate with initial two-fold O coordination to three-fold O coordination, consistent with past test results.

The testing of structures shown above constitutes the screening of Cu and O-terminated $Cu_2O(100)$ and $Cu_2O(100)\{100\}$ surfaces needed to select candidates for evaluating disproportionate adsorption energetics, which can be linked to anisotropic island shrinking. In summary, the screening of Cu and O-terminated $Cu_2O(100)$ and $Cu_2O(100)\{100\}$ interfaces revealed that O-terminated structures are more favorable than Cu-terminated structures overall. Additionally, adsorbate configurations on the most favorable structures were shown to initialize O (in MeOH) with two-fold coordination and subsequently relax to yield O (in MeO) with three-fold coordination primarily affected by additional Cu-O bonding. $Cu_2O(100)\{100\}$ structures proving more favorable than the most favorable $Cu_2O(100)$ flat surface adsorbate configurations (-1.19 eV) always featured MeO adsorption on relatively under-coordinated step edge sites, consistent with experimental expectations for anisotropic island shrinking. Furthermore, the most favorable $Cu_2O(100)\{100\}$ structure resolved observed MeO and H adsorbates on adjacent edge sites. Therefore, the structures selected as candidates for Figure 25, namely from evaluations performed via Figure 42-45, are shown in Figure 44A and Figure 44C, respectively.

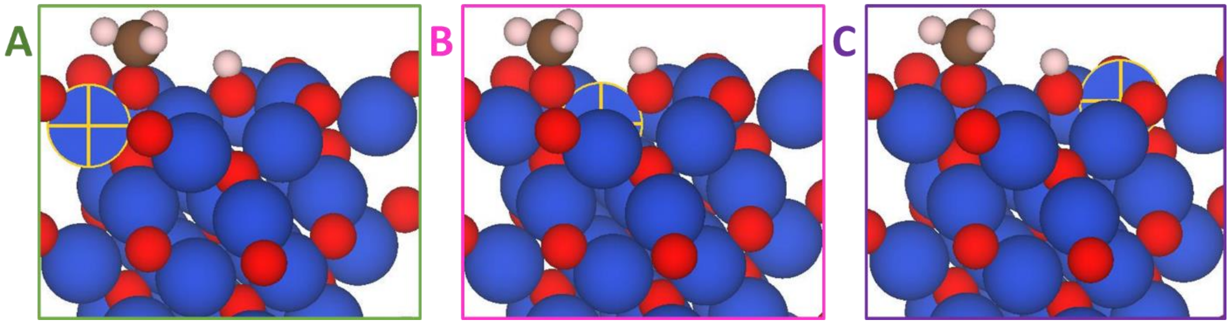

Figure 46. Tested Cu sites – labelled MeO (A), MeO-H (B), and H (C) – for Hubbard U linear response calculations, spanning the H diffusion path of MeOH dissociation.

Evaluation of the effects of electronic correlation starts with the calculation of Hubbard U (U_{3d}) parameters using a linear response approach on pertinent Cu atoms of evaluated structures. Preliminary relaxation and linear response calculations are completed by applying an energy cutoff (ENCUT) of 550 eV and calculation parameters otherwise matching those used in previous test calculations. Linear response techniques employed in past work were first applied to the most favorable flat $Cu_2O(100)$ system (Figure 42C), using a 4x4x1 Γ-point centered grid. Linear response calculations are applied to Cu sites over which H diffuses from MeO to next nearest neighbor O adsorbates, given that these Cu sites are closest to the dissociation processes being modeled. As depicted in Figure 45, Cu sites nearest MeO, between MeO and H, and nearest H adsorbates are calculated to have Hubbard U values of 8.81 ± 0.49 eV, 9.84 ± 0.60 eV, and 8.78 ± 0.54 eV, respectively. Validation for these results is provided by calculation of the Hubbard U values for bulk $CuCO_3$ and CuH_2O_2 systems, which respectively model Cu-O-C and Cu-O-H bonding and were resolved from OQMD. Using respective 2x2x2 (40 atoms) and 1x2x1 (20 atoms) supercells based on 8x8x8 Γ-point centered grid scaled for dimensions, respective Hubbard U values of 10.30 ± 0.50 eV and 10.14 ± 0.50 eV values were calculated for the systems shown in Figure 47.

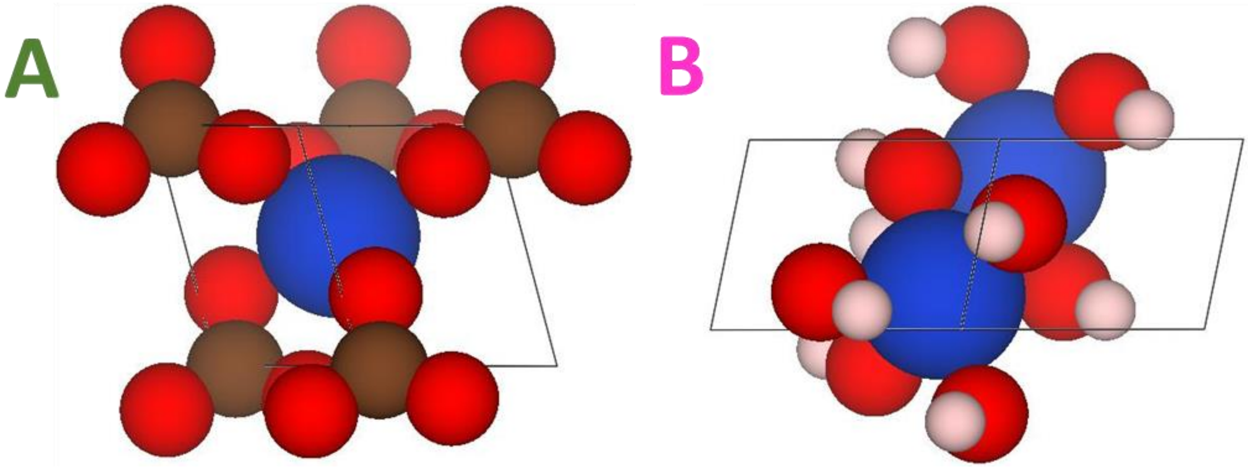

Figure 47. Unit cell representations of bulk $CuCO_3$ (A) and CuH_2O_2 (B) structures.

Given the Hubbard U values and their respective overlapping uncertainties, a single Hubbard U value of 9.3 eV was used to model all MeOH adsorption and dissociation processes involving electronic correlation in this work. Considering that the under-coordination of metal cations has been shown to produce changes in calculated linear response U values of ~0.5 eV, $CuCO_3$ and CuH_2O_2 can be equated to the previously calculated 9.3 eV result within uncertainty and other considerations. Reviewing the effects of surface undercoordination on calculated U values, this result is consistent with a similar Hubbard U value, which was calculated from fitting the band gap of bulk Cu_2O, applied to ethanol adsorption on $Cu_2O(111)$ surfaces[164, 219].

Final results comparing the most favorable flat surface (Figure 42C) to the most favorable stepped surface (Figure 44C) are displayed in Figure 25. Adsorption and diffusion energetics resolved in these sections apply an energy cutoff (ENCUT) of 400 eV, a Monkhorst-Pack *k*-point grid of 2x2x1, the DFT-D3 Grimme method for modeling dispersion effects, the Dudarev implementation of the Hubbard U method, and otherwise matching criteria compared to what was described previously. Including DFT-D3 in Hubbard U linear response calculations had effects (~0.1 eV) on those results that were well within reported uncertainties.

For all interfacial systems calculated in this section, Δ[ΔE] were calculated from a starting structure featuring MeOH adsorbates and two-fold O coordination, while leading to a terminal structure with three-fold O coordination and both MeO and H adsorbates. The Δ[ΔE] result calculated for MeOH dissociation on the most favorable flat $Cu_2O(100)$ surface (0.25 eV) is strongly consistent with the most favorable barriers associated with MeOH diffusion processes on $Cu_2O(111)$ in past work [165]. Beyond validating prior experimental sections, illustration of the link between adsorption site energetics and island shrinking retroactively validates the sole use of ΔE (Figure 42-57) in screening candidate structures for MeOH adsorption and dissociation.

3. Add ammonium hydroxide (28-30%) to this solution dropwise from a glass pipette (~10 drops), until the pH of the solution is approximately 10
4. Mix this solution for 20 min, then centrifuge, wash, dry, and finally calcine Cu/ZnO precipitates at 300 ºC in air

BIBLIOGRAPHY

1. Brown, L.F., *A comparative study of fuels for on-board hydrogen production for fuel-cell powered automobiles.* Int. J. Hydrogen Energy, 2001. **26**: p. 381-397.

2. Matsumura, Y., et al., *Catalytic methanol decomposition to carbon monoxide and hydrogen over nickel supported on silica.* Journal of Molecular Catalysis A: Chemical, 2000. **152**: p. 157-165.

3. Olah, G., *After Oil and Gas: Methanol Economy.* Catal. Lett., 2004. **93**: p. 1-2.

4. Masel, R., *Hydrogen Quick and Clean.* Nature, 2006. **442**: p. 521-522.

5. Wilhite, B.A., et al., *High-Purity Hydrogen Generation in a Microfabricated 23 wt % Ag-Pd Membrane Device Integrated with 8:1 LaNi0.95Co0.05O3/Al2O3 Catalyst.* Adv. Mater., 2006. **18**: p. 1701-1704.

6. Peschka, W., *The future cryofuel in internal combustion engines.* Int. J. Hydrogen Energy, 1998. **23**: p. 27-43.

7. Linder, B., *Operation of an internal combustion engine: Lean conditions with hydrogen produced in an onboard methanol reforming unit.* Fuel, 1984. **63**: p. 1485-1490.

8. Trimm, D.L. and Z.I. Onsan, *Onboard Fuel Conversion for Hydrogen-Fuel-Cell-Driven Vehicles.* Catal. Rev., 2001. **43**(1-2): p. 31-84.

9. Agrell, J., et al., *Production of hydrogen by partial oxidation of methanol over Cu/ZnO catalysts prepared by microemulsion technique.* Appl. Catal. A, 2001. **211**: p. 239-250.

10. Wang, Z., et al., *Selective production of hydrogen by partial oxidation of methanol over Cu/Cr catalysts.* Journal of Molecular Catalysis A: Chemical, 2003. **191**: p. 123-134.

11. Valdes-Solis, T., G. Marban, and A.B. Fuertes, *Nanosized catalysts for the production of hydrogen by methanol steam reforming.* Catal. Today, 2006. **116**: p. 354-360.

12. Brett, D.J.L., et al., *Methanol as a direct fuel in intermediate temperature solid oxide fuel cells with copper based anodes.* Chemical Engineering Science, 2005. **60**: p. 5649-5662.

13. Jiang, Y. and A.V. Virkar, *A high performance, anode-supported solid oxide fuel cell operating on direct alcohol.* Journal of the Electrochemical Society, 2001. **148**: p. A706-A709.

14. Sasaki, K., K. Watanabe, and T. Teraoka, *Directed-alcohol SOFCs: current-voltage characteristics and fuel gas compositions.* Journal of the Electrochemical Society, 2004. **151**: p. A965-A970.

15. Geissler, K., et al., *Autothermal methanol reforming for hydrogen production in fuel cell applicaitons.* Phys. Chem. Chem. Phys., 2001. **3**: p. 289-293.

16. Peppley, B., et al., *Methanol-steam reforming on Cu/ZnO/Al2O3.* Appl. Catal. A, 1999. **179**: p. 31-49.

17. Shobha, T., C.L. Arvainda, and L. Gomathi Devi, *Preparation and characterization of oxides of Ni-Cu:anode material for methanol oxidative fuel cells.* J. Solid State Electrochem., 2003. **7**: p. 451-455.

18. Agrell, J., H. Birgersson, and M. Boutonnet, *Steam reforming of methanol over a Cu/ZnO/Al2O3 catalyst: a kinetic analysis and strategies for suppression of CO formation.* J. Power Sources, 2002. **106**: p. 249-257.

19. Chin, Y.H., et al., *Methanol steam reforming over Pd/ZnO: Catalyst preparation and pretreatment studies.* Fuel Proc. Technol., 2003. **83**: p. 193-201.

20. Ito, S., et al., *Steam reforming of methanol over Pd-Zn alloy catalyst supported on carbon black.* Catalysis Communications, 2003. **4**: p. 499-503.

21. Liu, Y., et al., *Steam Reforming of Methanol Over Cu/CeO2 Catalysts Studied in Comparison with Cu/ZnO and Cu/Zn(Al)O Catalysts.* Topics in Catalysis, 2003. **22**: p. 205-213.

22. Chang, F.W., et al., *Production of hydrogen via partial oxidation of methanol over Au/TiO2 catalysts.* Appl. Catal. A, 2005. **290**: p. 138-147.

23. Cubeiro, M.L. and J.L.G. Fierro, *Selective Production of Hydrogen by Partial Oxidation of Methanol over ZnO-Supported Palladium Catalysts.* Journal of Catalysis, 1998. **179**(1): p. 150-162.

24. Velu, S., et al., *Oxidative Steam Reforming of Methanol over CuZnAl(Zr)-Oxide Catalysts for the Selective Production of Hydrogen for Fuel Cells: Catalyst Characterization and Performance Evaluation.* Journal of Catalysis, 2000. **194**(2): p. 373-384.

25. Wang, Z., W. Wang, and G. Lu, *Studies on the active species and on dispersion of Cu in Cu/SiO2 and Cu/Zn/SiO2 for hydrogen production via methanol partial oxidation.* Int. J. Hydrogen Energy, 2003. **28**: p. 151-158.

26. Alejo, L., et al., *Partial oxidation of methanol to produce hydrogen over Cu---Zn-based catalysts.* Appl. Catal. A, 1997. **162**: p. 281-297.

27. Zhou, L., et al., *Reactivity of oxidized copper surfaces in methanol oxidation.* Journal of Catalysis, 2005. **235**: p. 359-367.

28. Kunkes, E.L., et al., *Hydrogenation of CO2 to methanol and CO on Cu/ZnO/Al2O3: Is there a common intermediate or not?* Journal of Catalysis, 2015. **328**: p. 43-48.

29. Chinchen, G.C., K.C. Waugh, and D.A. Whan, *The activity and state of the copper surface in methanol synthesis catalysts.* Applied Catalysis, 1986. **25**(1): p. 101-107.

30. Alejo, L., et al., *Partial oxidation of methanol to produce hydrogen over Cu-Zn-based catalysts.* Applied Catalysis a-General, 1997. **162**(1-2): p. 281-297.

31. Greiner, M.T., et al., *The oxidation of copper catalysts during ethylene epoxidation.* Phys Chem Chem Phys, 2015. **17**(38): p. 25073-89.

32. Huang, T.-j. and S.-W. Wang, *Hydrogen production via partial oxidation of methanol over copper-zinc catalysts.* Applied Catalysis, 1986. **24**(1–2): p. 287-297.

33. Alejo, L., et al., *Partial oxidation of methanol to produce hydrogen over Cu · Zn-based catalysts.* Applied Catalysis A: General, 1997. **162**(1-2): p. 281-297.

34. Navarro, R.M., et al., *Production of hydrogen by partial oxidation of methanol over carbon-supported copper catalysts.* Topics in Catalysis, 2004. **30-1**(1-4): p. 481-486.

35. Eswaramoorthi, I., V. Sundaramurthy, and A. Dalai, *Partial oxidation of methanol for hydrogen production over carbon nanotubes supported Cu-Zn catalysts.* Applied Catalysis A: General, 2006. **313**(1): p. 22-34.

36. Lin, Y.-C., K.L. Hohn, and S.M. Stagg-Williams, *Hydrogen generation from methanol oxidation on supported Cu and Pt catalysts: Effects of active phases and supports.* Applied Catalysis A: General, 2007. **327**(2): p. 164-172.

37. Lin, Y.-C., et al., *Catalytic Pathways Identification for Partial Oxidation of Methanol on Copper−Zinc Catalysts: CH3OH + 1/2O2↔ CO2+ 2H2.* Industrial & Engineering Chemistry Research, 2008. **47**(8): p. 2523-2527.

38. Burch, R. and R.J. Chappell, *Support and additive effects in the synthesis of methanol over copper catalysts.* Appl. Catal., 1988. **45**: p. 131-150.

39. Klier, K., *Methanol Synthesis.* Adv. Catal., 1982. **30**: p. 243-313.

40. Herman, R.G., et al., *Catalytic synthesis of methanol from CO/H2: I. Phase composition, electronic properties, and activities of the Cu/ZnO/M2O3 catalysts.* J. Catal., 1979. **56**: p. 407-429.

41. Mehta, S., et al., *Catalytic synthesis of methanol from CO/H2: II. Electron microscopy (TEM, STEM, microdiffraction, and energy dispersive analysis) of the Cu/ZnO and Cu/ZnO/Cr2O3 catalysts.* J. Catal., 1979. **57**: p. 339-360.

42. Apai, G., J.R. Monnnier, and M.J. Hanrahan, *Experimental and theoretical approaches to the optical absorption spectra of sulfonyl radicals.* J. Phys. Chem., 1984. **87**: p. 3747-3750.

43. Okamoto, Y., et al., *Surface characterization of copper(II) oxide-zinc oxide methanol-synthesis catalysts by x-ray photoelectron spectroscopy. 2. Reduced catalysts.* J. Phys. Chem., 1983. **87**: p. 3747-3750.

44. Takahama, T., et al., *The preparation of a catalyst for the ester exchange reaction between ethylene glycol and DMT.* Appl. Catal., 1983. **5**: p. 59-64.

45. Bridgewater, A.J., et al., *Methanol synthesis over raney copper-zinc catalysts : III. optimization of alloy composition and catalyst preparation.* Appl. Catal., 1983. **7**: p. 369-382.

46. Fleisch, T.H. and R.L. Mieville, *Studies on the chemical state of Cu during methanol synthesis.* J. Catal., 1984. **80**: p. 165-172.

47. Chinchen, R.H., K.C. Waugh, and D.A. Whan, *The activity and state of the copper surface in methanol synthesis catalysts.* Appl. Catal., 1986. **25**: p. 101.

48. Denise, B., et al., *Supported copper catalysts in the synthesis of methanol: N2O-titrations.* Appl. Catal., 1987. **30**: p. 353-363.

49. Jones, P.M., et al., *Electron Spectroscopic Studies of CH3OH Chemisorption on Cu2O and ZnO Single-Crystal Surfaces: Methoxide Bonding and Reactivity Related to Methanol Synthesis.* J. Am. Chem. Soc., 1998. **120**: p. 1506-1516.

50. Navarro, R.M., M.A. Pena, and J.L.G. Fierro, *Production of Hydrogen by Partial Oixudation of Methanol over a Cu/ZnO/Al2O3 Catalyst: Influence of the Initial State of the Catalysts on the Start-up Behavior of the Reformer.* J. Catal., 2002. **212**: p. 112-118.

51. Severino, F., et al., *Nature of Copper Active Sites in the Carbon Monoxide Oxidation on CuAl2O4and CuCr2O4Spinel Type Catalysts.* J. Catal., 1998. **177**: p. 82-95.

52. Idem, R.O. and N.N. Bakhshi, *"Production of Hydrogen from Methanol over Promoted Coprecipitated Cu-Al Catalysts: The Effects of Various Promoters and Catalyst Activation Methods.* Ind. Eng. Chem. Res., 1995. **34**: p. 1548-1557.

53. Navarro, R.M., et al., *Production of hydrogen by partial oxidation of methanol over carbon-supported copper catalysts.* Topics in Catalysis, 2004. **30/31**: p. 481-486.

54. Ma, J., et al., *Modifications in the Morphological and Chemical Properties of Copper Supported on Different Allotropic Forms of Carbon.* J. Catal., 1999. **183**: p. 32-44.

55. Nakashashi, K., et al., *Diamond-Supported Metal Catalyst: A Novel Medium for Hydrogen Production from Methanol Decomposition.* Catal. Lett., 2002. **80**(3-4): p. 161-164.

56. Reitz, T., et al., *Time-Resolved XANES Investigation of CuO/ZnO in the Oxidative Methanol Reforming Reaction.* J. Catal., 2001. **199**: p. 193-201.

57. Gunter, M.M., et al., *Redox Behavior of Copper Oxide/Zinc Oxide Catalysts in the Steam Reforming of Methanol Studied by in Situ X-Ray Diffraction and Absorption Spectroscopy.* J. Catal., 2001. **203**: p. 133-149.

58. Agrell, J., M. Boutonnet, and J.L.G. Fierro, *Production of hydrogen from methanol over binary Cu/ZnO catalysts - Part II. Catalytic activity and reaction pathways.* Applied Catalysis a-General, 2003. **253**(1): p. 213-223.

59. Navarro, R.M., M.A. Pena, and J.L.G. Fierro, *Production of hydrogen by partial oxidation of methanol over a Cu/ZnO/Al2O3 catalyst: Influence of the initial state of the catalyst on the start-up behaviour of the reformer.* Journal of Catalysis, 2002. **212**(1): p. 112-118.

60. Agrell, J., et al., *Production of hydrogen from methanol over Cu/ZnO catalysts promoted by ZrO2 and Al2O3.* Journal of Catalysis, 2003. **219**(2): p. 389-403.

61. Huang, T.-J. and S.-W. Wang, *Hydrogen production via partial oxidation of methanol over copper-zinc catalysts.* Appl. Catal., 1986. **24**: p. 287-297.

62. González Carrazán, S.R., et al., *Modulation of the selectivity in partial oxidation of methanol over CuZnAl catalysts by adding CO2 and/or H2 into the reaction feed.* Applied Catalysis B: Environmental, 2015. **168-169**: p. 14-24.

63. Gai, P.L. and E.D. Boyers, *Electron Microscopy in Heterogeneous Catalysts*. 2003, London: Institute of Physics.

64. Boudart, M., *Kinetics and Mechanism of Ammonia Synthesis.* Catal. Rev. Sci. Eng., 1981. **23**: p. 1-15.

65. Kishimoto, S., *Influence of annealing on the catalytic activity of cold-worked metals for the decomposition of formic acid.* The Journal of Physical Chemistry, 1973. **77**(13): p. 1719.

66. Sinfelt, J.H., *Catalytic Hydrogenolysis over Supported Metals.* Catal. Rev., 1970. **3**: p. 175-205.

67. Sendner, C., S. Sakong, and A. Gross, *Kinetic Monte Carlo simulations of the partial oxidation of methanol on oxygen-covered Cu(110).* Surface Science, 2006. **600**(16): p. 3258-3265.

68. Besharat, Z., et al., *Dehydrogenation of methanol on Cu2O(100) and (111).* The Journal of Chemical Physics, 2017. **146**(24): p. 244702.

69. Li, J. and G. Zhou, *Density functional theory study of O–H and C–H bond scission of methanol catalyzed by a chemisorbed oxygen layer on Cu(111).* Surface Science, 2016. **646**: p. 288-297.

70. Sakong, S. and A. Gross, *Total Oxidation of Methanol on Cu(110): A Density Functional Theory Study*. The Journal of Physical Chemistry A, 2007. **111**(36): p. 8814-8822.

71. Lawton, T.J., et al., *An Atomic Scale View of Methanol Reactivity at the Cu(1 1 1)/CuOxInterface.* ChemCatChem, 2013. **5**(9): p. 2684-2690.

72. Behrens, M., et al., *The Active Site of Methanol Synthesis over Cu/ZnO/Al2O3 Industrial Catalysts*. Science, 2012. **336**(6083): p. 893-897.

73. Lunkenbein, T., et al., *Formation of a ZnO overlayer in industrial Cu/ZnO/Al2 O3 catalysts induced by strong metal-support interactions.* Angew Chem Int Ed Engl, 2015. **54**(15): p. 4544-8.

74. Tao, F. and M. Salmeron, *In Situ Studies of Chemistry and Structure of Materials in Reactive Environments.* Science, 2011. **331**: p. 171.

75. Ertl, G., *Reactions on Solid Surfaces*. 2 ed. 2009: Wiley.

76. Sharma, R., et al., *Observation of dynamic nanostructural and nanochemical changes in Ceria-based catalysts during in situ reduction.* Phil. Mag., 2004. **84**: p. 2731-2747.

77. Sharma, R., et al., *In Situ Nanoscale Observations of the Mg(OH)2 Dehydroxylation and Rehydroxylation Mechanisms.* Phil. Mag., 2004. **84**: p. 2711-2729.

78. Gai, P.L., *Microstructure and microanalysis of bismuth molybdates.* J. Solid State Chem., 1980. **49**: p. 25-42.

79. Gai, P.L., *Dynamic studies of metal oxide catalysts: MoO3.* Phil. Mag., 1981. **43**(4): p. 841-855.

80. Gai, P.L., J.C. Bart, and E.D. Boyes, *Electron microscopy of industrial oxidation catalysts.* Phil. Mag. A, 1982. **45**: p. 531-547.

81. Gai, P.L., *Structural Evolution of Extended Defects in Nonstoichiometric Solids.* J. Solid State Chem., 1993. **104**: p. 119-130.

82. Gai, P.L. and K. Kourtakis, *Solid-state defect mechanism in vanadyl pyrophosphate catalysts: Implications for selective.* Science, 1995. **267**: p. 661.

83. Gai, P.L., *A new structural transformation mechanism in catalytic oxides.* Acta Cryst. B, 1997. **53**: p. 346-352.

84. Andersson, J.S., et al, *Point Defects and Extended Defects in Niobium Oxides.* Nature, 1973. **243**: p. 81.

85. Wacha, I.E. and R.J. Madix, *The selective oxidation of CH3OH to H2CO on a copper(110) catalyst.* J. Catal., 1978. **53**: p. 208-227.

86. Sexton, B.A., A.E. Hughes, and N.R. Avery, *A spectroscopic study of the adsorption and reactions of methanol, formaldehyde and methyl formate on clean and oxygenated Cu(110) surfaces.* Surface Science, 1985. **155**: p. 366-386.

87. Bowker, M. and R.J. Madix, *XPS, UPS and thermal desorption studies of alcohol adsorption on Cu(110) : I. Methanol.* Surface Science, 1980. **95**: p. 190-206.

88. Ammon, C., et al., *Dissociation and oxidation of methanol on Cu(1 1 0).* Surface Science, 2002. **507**(845-850).

89. Sender, C., S. Sakong, and A. Gross, *Kinetic Monte Carlo simulations of the partial oxidation of methanol on oxygen-covered Cu(110).* Surface Science, 2006. **600**: p. 3258-3265.

90. Sakong, S. and A. Gross, *Density functional theory study of the partial oxidation of methanol on copper surfaces.* J. Catal., 2005. **231**: p. 420-429.

91. Russel Jr, J.N., S.M. Gates, and J.T. Yates, *Reaction of methanol with Cu(111) and Cu(111) + O(ads).* Surface Science, 1985. **163**: p. 516-540.

92. Russell, J.N., S.M. Gates, and J.T. Yates, *Reaction of methanol with Cu(111) and Cu(111) + O(ads).* Surface Science, 1985. **163**(2): p. 516-540.

93. Ryberg, R., *The oxidation of methanol on Cu(100).* The Journal of Chemical Physics, 1985. **82**(1): p. 567-573.

94. Tanaka, K., Fujita, T., and Okawa, Y., Surface Science, 1998. **401**: p. L407-412.

95. Leibsle, F.M., Surface Science, 1998. **337**(1-2): p. 51-66.

96. Lederer, T., Arvanitis, D., Comelli, G., Troger, L., Baberschke, K., Phys. Rev. B., 1993. **48**: p. 15390-15404.

97. Knight, P.J., Driver, S.M., Woodruff, D.P., J Phys-Condens Mat., 1997. **9**(1): p. 21-31.

98. Coulman, D.J., Wintterlin, J., Behm, R.J., Ertl, G., Phys. Rev. Lett., 1990. **64**: p. 1761-1764.

99. Jensen, F., Besenbacher, F., Lagsgaard, E., Stensgaard, I., Surface Science, 1991. **259**: p. l781.

100. Jensen, F., Besenbacher, F., Stensgaard, I., Surface Science, 1992. **269/270**: p. 400-404.

101. Besenbacher, F., and Norskov, J.K., Progress in Surface Science, 1993. **44**: p. 5-66.

102. Matsumoto, T., Bennett, R.A., Stone, P., Yamada, T., Domen, K., Bowker, M., Surface Science, 2001. **471**(1-3): p. 225-245.

103. Jensen, F., Besenbacher, F., Lagsgaard, E., Stensgaard, I., Surface Science Letters, 1991. **259**: p. L774-780.

104. Zhou, G.W., W.S. Slaughter, and J.C. Yang, *Terraced hollow oxide pyramids.* Phys. Rev. Lett., 2005. **94**(24): p. 246101.

105. Zhou, G.W., et al., *Cu_2O island shape transition during Cu-Au oxidation.* Physical Review Letters, 2006. **96**: p. 226108.

106. Zhou, G.W. and J.C. Yang, *Formation of Quasi-one-dimensional Cu_2O structures by in situ oxidation of Cu(100).* Phys. Rev. Lett., 2002. **89**: p. 106101.

107. Zhou, G.W. and J.C. Yang, *Initial Oxidation Kinetics of Copper (110) film investigated by in situ UHV-TEM.* Surface Science, 2003. **531**: p. 359-367.

108. Zhou, G.W. and J.C. Yang, *Temperature effect on the Cu_2O Oxide Morphology Created by Oxidation of Cu(001) as Investigated by in situ UHV TEM.* Applied Surface Science, 2003. **210**: p. 165-170.

109. Zhou, G.W. and J.C. Yang, *Temperature effects on the Growth of Oixde islands on Cu(110).* Applied Surface Science, 2004. **222**: p. 357-364.

110. Zhou, G.W. and J.C. Yang, *Initial oxidation kinetics of Cu(100), (110), and (111) thin films investigated by in situ ultra-high-vacuum transmission electron microscopy.* Journal of Materials Research, 2005. **20**(7): p. 1684-1694.

111. Zhou, G.W., L. Wang, and J.C. Yang, *Effect of surface topology on the formation of oxide islands on Cu surfaces.* J. Appl. Phys., 2005. **97**: p. 063509.

112. Holse, C., et al., *Dynamic Behavior of CuZn Nanoparticles under Oxidizing and Reducing Conditions.* The Journal of Physical Chemistry C, 2015: p. 150122080137001.

113. Kresse, G. and J. Furthmuller, *Efficient iterative schemes for ab initio total-energy calculations using a plane-wave basis set.* Phys Rev B Condens Matter, 1996. **54**(16): p. 11169-11186.

114. Kresse, G. and J. Furthmüller, *Efficiency of ab-initio total energy calculations for metals and semiconductors using a plane-wave basis set.* Computational Materials Science, 1996. **6**(1): p. 15-50.

115. Kresse, G. and J. Hafner, *Ab initio molecular dynamics for liquid metals.* Phys Rev B Condens Matter, 1993. **47**(1): p. 558-561.

116. Kresse, G. and J. Hafner, *Ab initio molecular-dynamics simulation of the liquid-metal-amorphous-semiconductor transition in germanium.* Phys Rev B Condens Matter, 1994. **49**(20): p. 14251-14269.

117. Perdew, J.P., et al., *Atoms, molecules, solids, and surfaces: Applications of the generalized gradient approximation for exchange and correlation.* Phys Rev B Condens Matter, 1992. **46**(11): p. 6671-6687.

118. Blochl, P.E., *Projector augmented-wave method.* Phys Rev B Condens Matter, 1994. **50**(24): p. 17953-17979.

119. Kresse, G. and D. Joubert, *From ultrasoft pseudopotentials to the projector augmented-wave method.* Phys. Rev. B, 1999. **59**(3): p. 1758-1775.

120. Momma, K. and F. Izumi, *VESTA: a three-dimensional visualization system for electronic and structural analysis.* Journal of Applied Crystallography, 2008. **41**(3): p. 653-658.

121. Momma, K. and F. Izumi, *VESTA: a three-dimensional visualization system for electronic and structural analysis.* J. Appl. Cryst., 2011. **44**(6): p. 1272-1276.

122. Henkelman, G., B.P. Uberuaga, and H. Jónsson, *A climbing image nudged elastic band method for finding saddle points and minimum energy paths.* J. Chem. Phys., 2000. **113**(22): p. 9901-9904.

123. Maimaiti, Y., M. Nolan, and S.D. Elliott, *Reduction mechanisms of the CuO(111) surface through surface oxygen vacancy formation and hydrogen adsorption.* Physical Chemistry Chemical Physics, 2014. **16**(7): p. 3036-3046.

124. Wang, L., T. Maxisch, and G. Ceder, *Oxidation energies of transition metal oxides within the `$\mathrm{GGA}+\mathrm{U}$` framework.* Physical Review B, 2006. **73**(19): p. 195107.

125. Dudarev, S.L., et al., *Electron-energy-loss spectra and the structural stability of nickel oxide: An LSDA+U study.* Physical Review B, 1998. **57**(3): p. 1505-1509.

126. Grabow, L.C. and M. Mavrikakis, *Mechanism of Methanol Synthesis on Cu through CO2and CO Hydrogenation.* ACS Catalysis, 2011. **1**(4): p. 365-384.

127. Johansson, A.J. and T. Brinck, *Mechanisms and energetics of surface reactions at the copper-water interface*. 2012, TR-12-07, Swedish Nuclear Fuel Management Co., Stockholm, Sweden, 2012 Search PubMed.

128. Cococcioni, M. and S. de Gironcoli, *Linear response approach to the calculation of the effective interaction parameters in the $\mathrm{LDA}+\mathrm{U}$ method.* Physical Review B, 2005. **71**(3): p. 035105.

129. Curnan, M.T. and J.R. Kitchin, *Investigating the Energetic Ordering of Stable and Metastable TiO2 Polymorphs Using DFT+U and Hybrid Functionals.* The Journal of Physical Chemistry C, 2015. **119**(36): p. 21060-21071.

130. Aschauer, U., J. Chen, and A. Selloni, *Peroxide and superoxide states of adsorbed O2 on anatase TiO2 (101) with subsurface defects.* Physical Chemistry Chemical Physics, 2010. **12**(40): p. 12956-12960.

131. Padama, A.A., et al., *NO dissociation on Cu(111) and Cu2O(111) surfaces: a density functional theory based study.* J Phys Condens Matter, 2012. **24**(17): p. 175005.

132. Agrell, J., H. Birgersson, and M. Boutonnet, *Steam reforming of methanol over a Cu/ZnO/Al2O3 catalyst: a kinetic analysis and strategies for suppression of CO formation.* Journal of Power Sources, 2002. **106**(1-2): p. 249-257.

133. Raimondi, F., et al., *Hydrogen production by methanol reforming: post-reaction characterisation of a Cu/ZnO/Al2O3 catalyst by XPS and TPD.* Applied Surface Science, 2002. **189**(1-2): p. 59-71.

134. Agrell, J., M. Boutonnet, and J.L.G. Fierro, *Production of hydrogen from methanol over binary Cu/ZnO catalysts.* Applied Catalysis A: General, 2003. **253**(1): p. 213-223.

135. Li, C.-L. and Y.-C. Lin, *Catalytic Partial Oxidation of Methanol over Copper–Zinc Based Catalysts: A Comparative Study of Alumina, Zirconia, and Magnesia as Promoters.* Catalysis Letters, 2010. **140**(1-2): p. 69-76.

136. Sakong, S. and A. Gros, *Density functional theory study of the partial oxidation of methanol on copper surfaces.* Journal of Catalysis, 2005. **231**(2): p. 420-429.

137. Sakong, S. and A. Gross, *Total oxidation of methanol on Cu(110): a density functional theory study*. J Phys Chem A, 2007. **111**(36): p. 8814-22.

138. Sun, S., Y. Wang, and Q. Yang, *Density functional theory study of the methanol adsorption and dissociation on CuO(111) surface.* Applied Surface Science, 2014. **313**: p. 777-783.

139. Studt, F., et al., *The Mechanism of CO and CO2Hydrogenation to Methanol over Cu-Based Catalysts.* ChemCatChem, 2015. **7**(7): p. 1105-1111.

140. Oh, S.H. and R.M. Sinkevitch, *Carbon monoxide removal from hydrogen-rich fuel cell feedstreams by selective catalytic oxidation.* Journal of Catalysis, 1993. **142**(1): p. 254-262.

141. Greeley, J. and M. Mavrikakis, *Methanol Decomposition on Cu(111): A DFT Study.* Journal of Catalysis, 2002. **208**(2): p. 291-300.

142. Rabe, S. and F. Vogel, *A thermogravimetric study of the partial oxidation of methanol for hydrogen production over a Cu/ZnO/Al2O3 catalyst.* Applied Catalysis B: Environmental, 2008. **84**(3-4): p. 827-834.

143. Lee, K.-Y., C.-C. Shen, and Y.-J. Huang, *Enhancement of the Partial Oxidation of Methanol Reaction over CuZn Catalyst by Mn Promoter.* Industrial & Engineering Chemistry Research, 2014. **53**(32): p. 12622-12630.

144. Le, D., S. Stolbov, and T.S. Rahman, *Reactivity of the Cu2O(100) surface: Insights from first principles calculations.* Surface Science, 2009. **603**(10): p. 1637-1645.

145. Sun, B.-Z., W.-K. Chen, and Y.-J. Xu, *Reaction mechanism of CO oxidation on Cu2O(111): A density functional study.* The Journal of Chemical Physics, 2010. **133**(15): p. 154502.

146. Chen, S., et al., *Oxidation Resistance of Graphene-Coated Cu and Cu/Ni Alloy.* ACS Nano, 2011. **5**(2): p. 1321-1327.

147. Pint, B.A., J.R. DiStefano, and I.G. Wright, *Oxidation resistance: One barrier to moving beyond Ni-base superalloys.* Materials Science and Engineering: A, 2006. **415**(1): p. 255-263.

148. Prescott, R. and M.J. Graham, *The formation of aluminum oxide scales on high-temperature alloys.* Oxidation of Metals, 1992. **38**(3): p. 233-254.

149. Li, J., J.W. Mayer, and E.G. Colgan, *Oxidation and protection in copper and copper alloy thin films.* Journal of Applied Physics, 1991. **70**(5): p. 2820-2827.

150. Chi, H., et al., *Dependence of H2 and CO2 selectivity on Cu oxidation state during partial oxidation of methanol on Cu/ZnO.* Applied Catalysis A: General, 2018. **556**: p. 64-72.

151. Grabow, L.C. and M. Mavrikakis, *Mechanism of Methanol Synthesis on Cu through CO2 and CO Hydrogenation.* ACS Catalysis, 2011. **1**(4): p. 365-384.

152. Studt, F., et al., *The Mechanism of CO and CO2 Hydrogenation to Methanol over Cu-Based Catalysts.* ChemCatChem, 2015. **7**(7): p. 1105-1111.

153. Kuld, S., et al., *Quantifying the promotion of Cu catalysts by ZnO for methanol synthesis.* Science, 2016. **352**(6288): p. 969-974.

154. Cox, D.F., *Methanol decomposition on single crystal Cu2O.* Journal of Vacuum Science & Technology A: Vacuum, Surfaces, and Films, 1990. **8**(3): p. 2599.

155. Saito, M. and K. Murata, *Development of high performance Cu/ZnO-based catalysts for methanol synthesis and the water-gas shift reaction.* Catalysis Surveys from Asia, 2004. **8**(4): p. 285-294.

156. Spencer, M.S., *The role of zinc oxide in Cu ZnO catalysts for methanol synthesis and the water-gas shift reaction.* Topics in Catalysis, 1999. **8**(3-4): p. 259-266.

157. van den Berg, R., et al., *Structure sensitivity of Cu and CuZn catalysts relevant to industrial methanol synthesis.* Nat Commun, 2016. **7**: p. 13057.

158. Li, S., J. Scaranto, and M. Mavrikakis, *On the Structure Sensitivity of Formic Acid Decomposition on Cu Catalysts.* Topics in Catalysis, 2016. **59**(17): p. 1580-1588.

159. Wachs, I.E. and R.J. Madix, *The selective oxidation of CH3OH to H2CO on a copper (110) catalyst.* Journal of Catalysis, 1978. **53**(2): p. 208-227.

160. Sexton, B.A., *Surface vibrations of adsorbed intermediates in the reaction of alcohols with Cu(100).* Surface Science, 1979. **88**(2): p. 299-318.

161. Sakong, S. and A. Groß, *Density functional theory study of the partial oxidation of methanol on copper surfaces.* Journal of Catalysis, 2005. **231**(2): p. 420-429.

162. Sakong, S., C. Sendner, and A. Gross, *Partial oxidation of methanol on Cu(110): Energetics and kinetics.* Journal of Molecular Structure-Theochem, 2006. **771**(1-3): p. 117-122.

163. Soon, A., et al., *Surface oxides of the oxygen–copper system: Precursors to the bulk oxide phase?* Surface Science, 2007. **601**(24): p. 5809-5813.

164. Xu, H., et al., *Mechanism of C-C and C-H bond cleavage in ethanol oxidation reaction on Cu2O(111): a DFT-D and DFT+U study.* Physical Chemistry Chemical Physics, 2017. **19**(38): p. 26210-26220.

165. Riguang, Z., et al., *A DFT study on the formation of CH3O on Cu2O(111) surface by CH3OH decomposition in the absence or presence of oxygen.* Applied Surface Science, 2011. **257**(9): p. 4232-4238.

166. Senanayake, S.D., et al., *Hydrogenation of CO2 to Methanol on CeOx/Cu(111) and ZnO/Cu(111) Catalysts: Role of the Metal–Oxide Interface and Importance of Ce3+ Sites.* The Journal of Physical Chemistry C, 2016. **120**(3): p. 1778-1784.

167. Rodriguez, J.A., et al., *Hydrogenation of CO2 to Methanol: Importance of Metal–Oxide and Metal–Carbide Interfaces in the Activation of CO2.* ACS Catalysis, 2015. **5**(11): p. 6696-6706.

168. Waluyo, I., et al., *Potassium-Promoted Reduction of Cu2O/Cu(111) by CO.* The Journal of Physical Chemistry C, 2018.

169. Kim, J.Y., et al., *Reduction of CuO and Cu2O with H2: H embedding and kinetic effects in the formation of suboxides.* Journal of the American Chemical Society, 2003. **125**: p. 10684-10692.

170. Pike, J., et al., *Formation of stable Cu2O from reduction of CuO nanoparticles.* Applied Catalysis A: General, 2006. **303**(2): p. 273-277.

171. Sun, S., Y. Wang, and Q. Yang, *Density functional theory study of the methanol adsorption and dissociation on CuO(1 1 1) surface.* Applied Surface Science, 2014. **313**: p. 777-783.

172. Zuo, Z.-J., et al., *Insight into the size effect on methanol decomposition over Cu-based catalysts based on density functional theory.* Computational and Theoretical Chemistry, 2014. **1033**: p. 14-22.

173. Chi, H., et al., *Structural Change of a Cu/ZnO Catalyst under Methanol Observed by ETEM.* Microscopy and Microanalysis, 2017. **23**(S1): p. 2100-2101.

174. Zou, L., et al., *In situ atomic-scale imaging of the metal/oxide interfacial transformation.* Nature Communications, 2017. **8**(1): p. 307.

175. Meng, S., et al., *Atomistic Insight into the Redox Reactions in Fe/Oxide Core–Shell Nanoparticles.* Chemistry of Materials, 2018: p. acs.chemmater.8b03679.

176. Zhu, W., et al., *In Situ Atomic-Scale Probing of the Reduction Dynamics of Two-Dimensional Fe2O3Nanostructures.* ACS Nano, 2017. **11**: p. 656-664.

177. Lagrow, A.P., et al., *Visualizing the Cu/Cu2O interface transition in nanoparticles with environmental scanning transmission electron microscopy.* Journal of the American Chemical Society, 2017. **139**: p. 179-185.

178. Simonsen, S.B., et al., *Coarsening of Pd nanoparticles in an oxidizing atmosphere studied by in situ TEM.* Surface Science, 2016. **648**: p. 278-283.

179. Nielsen, M.H., S. Aloni, and J.J. De Yoreo, *In situ TEM imaging of CaCO<sub>3</sub> nucleation reveals coexistence of direct and indirect pathways.* Science, 2014. **345**(6201): p. 1158.

180. Zhou, G. and J.C. Yang, *Temperature effect on the Cu2O oxide morphology created by oxidation of Cu(0 0 1) as investigated by in situ UHV TEM.* Applied Surface Science, 2003. **210**(3–4): p. 165-170.

181. Zhou, G. and J.C. Yang, *Initial oxidation kinetics of copper (110) film investigated by in situ UHV-TEM.* Surface Science, 2003. **531**(3): p. 359-367.

182. Zhou, G. and J.C. Yang, *Initial Oxidation Kinetics of Cu(100), (110), and (111) Thin Films Investigated by in Situ Ultra-high-vacuum Transmission Electron Microscopy.* Journal of Materials Research, 2005. **20**(07): p. 1684-1694.

183. Zhou, G. and J.C. Yang, *Reduction of Cu2O islands grown on a Cu(100) surface through vacuum annealing.* Phys Rev Lett, 2004. **93**(22): p. 226101.

184. Akaike, H., *A new look at the statistical model identification.* IEEE Transactions on Automatic Control, 1974. **19**(6): p. 716-723.

185. Zhou, G. and J.C. Yang, *Formation of Quasi-One-Dimensional ${\mathrm{C}\mathrm{u}}_{2}\mathrm{O}$ Structures by in situ Oxidation of Cu(100).* Physical Review Letters, 2002. **89**(10): p. 106101.

186. Zhu, Q., et al., *Early and transient stages of Cu oxidation: Atomistic insights from theoretical simulations and in situ experiments.* Surface Science, 2016. **652**: p. 98-113.

187. Tersoff, J. and R.M. Tromp, *Shape transition in growth of strained islands: Spontaneous formation of quantum wires.* Phys Rev Lett, 1993. **70**(18): p. 2782-2785.

188. Bowker, M., *Catalysis resolved using scanning tunnelling microscopy.* Chem Soc Rev, 2007. **36**(10): p. 1656-73.

189. Chi, H., et al., *In situ Observation of Cu2O Island Shrinking on Cu(100) Facet under Methanol Using Environmental Transmission Electron Microscopy.* Microscopy and Microanalysis, 2018. **24**: p. 302-303.

190. Zhu, Q., W.A. Saidi, and J.C. Yang, *Step-Edge Directed Metal Oxidation.* The Journal of Physical Chemistry Letters, 2016. **7**(13): p. 2530-2536.

191. Andolina, C.M., et al., *Constructing a predictive model of copper oxidation from experiment and theory.* Microscopy and Microanalysis, 2017. **23**(S1): p. 920-921.

192. Zhu, Q., W.A. Saidi, and J.C. Yang, *Step-induced oxygen upward diffusion on stepped Cu(100) surface.* The Journal of Physical Chemistry C, 2015. **119**(1): p. 251-261.

193. Zhu, Q., W.A. Saidi, and J.C. Yang, *Enhanced Mass Transfer in the Step Edge Induced Oxidation on Cu(100) Surface.* The Journal of Physical Chemistry C, 2017. **121**(21): p. 11251-11260.

194. Henkelman, G., B.P. Uberuaga, and H. Jónsson, *A climbing image nudged elastic band method for finding saddle points and minimum energy paths.* The Journal of Chemical Physics, 2000. **113**(22): p. 9901-9904.

195. Henkelman, G. and H. Jónsson, *Improved tangent estimate in the nudged elastic band method for finding minimum energy paths and saddle points.* The Journal of Chemical Physics, 2000. **113**(22): p. 9978-9985.

196. Huang, T.J. and S.W. Wang, *HYDROGEN-PRODUCTION VIA PARTIAL OXIDATION OF METHANOL OVER COPPER-ZINC CATALYSTS.* Applied Catalysis, 1986. **24**(1-2): p. 287-297.

197. Zhou, G., et al., *Step-Edge-Induced Oxide Growth During the Oxidation of Cu Surfaces.* Physical Review Letters, 2012. **109**(23): p. 235502.

198. Mei, D.H., L.J. Xu, and G. Henkelman, *Potential Energy Surface of Methanol Decomposition on Cu(110).* Journal of Physical Chemistry C, 2009. **113**(11): p. 4522-4537.

199. Hansen, P.L., et al., *Atom-Resolved Imaging of Dynamic Shape Changes in Supported Copper Nanocrystals.* Science, 2002. **295**(5562): p. 2053-2055.

200. Delmon, B., et al., *Handbook of heterogeneous catalysis.* Ertl, Knözinger, Weitkamp (Eds.), VCH, Weinheim, 1997: p. 1387.

201. Jeangros, Q., et al., *Reduction of nickel oxide particles by hydrogen studied in an environmental TEM.* Journal of Materials Science, 2013. **48**(7): p. 2893-2907.

202. Chenna, S., R. Banerjee, and P.A. Crozier, *Atomic-Scale Observation of the Ni Activation Process for Partial Oxidation of Methane Using In Situ Environmental TEM.* ChemCatChem, 2010. **3**(6): p. 1051-1059.

203. Zhu, W., et al., *Atomic structural evolution during the reduction of α-Fe2O3nanowires.* Journal of Physical Chemistry C, 2016. **120**: p. 14854-14862.

204. Chi, H., et al., *In situ Observation of C112O Island Shrinking on Cu(100) Facet under Methanol Using Environmental Transmission Electron Microscopy.* Microscopy and Microanalysis, 2018. **24**(S1): p. 302-303.

205. Monkhorst, H.J. and J.D. Pack, *Special points for Brillouin-zone integrations.* Phys. Rev. B, 1976. **13**(12): p. 5188-5192.

206. Methfessel, M. and A.T. Paxton, *High-precision sampling for Brillouin-zone integration in metals.* Phys Rev B Condens Matter, 1989. **40**(6): p. 3616-3621.

207. Perdew, J.P., K. Burke, and M. Ernzerhof, *Generalized Gradient Approximation Made Simple.* Physical Review Letters, 1996. **77**(18): p. 3865-3868.

208. Perdew, J.P., K. Burke, and M. Ernzerhof, Phys. Rev. Lett., 1997. **78**.

209. Mishra, A.K., A. Roldan, and N.H. de Leeuw, *CuO Surfaces and CO2 Activation: A Dispersion-Corrected DFT+U Study.* The Journal of Physical Chemistry C, 2016. **120**(4): p. 2198-2214.

210. Nolan, M. and S.D. Elliott, *The p-type conduction mechanism in Cu2O: a first principles study.* Physical Chemistry Chemical Physics, 2006. **8**(45): p. 5350-5358.

211. Ekuna, C.E., et al., Eur. Phys. B. , 2014. **87**.

212. Yu, K. and E.A. Carter, *Communication: Comparing ab initio methods of obtaining effective U parameters for closed-shell materials.* The Journal of Chemical Physics, 2014. **140**(12): p. 121105.

213. Isseroff, L.Y. and E.A. Carter, Phys Rev B Condens Matter, 2012. **85**.

214. Jiang, P., et al., *Experimental and theoretical investigation of the electronic structure of Cu2O and CuO thin films on Cu(110) using x-ray photoelectron and absorption spectroscopy.* The Journal of Chemical Physics, 2013. **138**(2): p. 024704.

215. Kulik, H.J. and N. Marzari, *A self-consistent Hubbard U density-functional theory approach to the addition-elimination reactions of hydrocarbons on bare FeO+.* The Journal of Chemical Physics, 2008. **129**(13): p. 134314.

216. Capdevila-Cortada, M., Z. Łodziana, and N. López, *Performance of DFT+U Approaches in the Study of Catalytic Materials.* ACS Catalysis, 2016. **6**(12): p. 8370-8379.

217. Bhola, K., et al., *Influence of Hubbard U Parameter in Simulating Adsorption and Reactivity on CuO: Combined Theoretical and Experimental Study*. The Journal of Physical Chemistry C, 2017.

218. Wang, W., et al., *Synthesis of CuO and Cu2O crystalline nanowires using Cu(OH)2 nanowire templates.* Journal of Materials Research, 2011. **18**(12): p. 2756-2759.

219. Aschauer, U., et al., *Influence of Subsurface Defects on the Surface Reactivity of TiO2: Water on Anatase (101).* The Journal of Physical Chemistry C, 2010. **114**(2): p. 1278-1284.

220. Lee, K.Y., H. Hwang, and W. Choi, *Advanced Thermopower Wave in Novel ZnO Nanostructures/Fuel Composite*. ACS Applied Materials & Interfaces, 2014. **6**(17): p. 15575-15582.